Understanding the Development and Growth

of the Zebrafish (*Danio rerio*) Infraorbital Bones.

By

Carolyn Chang

A Thesis Submitted to
Saint Mary's University, Halifax, Nova Scotia
in Partial Fulfillment of the Requirements for
the Degree of Master's of Science in Applied Science.

August, 2013, Halifax, Nova Scotia

© Carolyn Chang, 2013

Dedication

This thesis is dedicated to the different teachers and mentors that have helped to guide me throughout my education. The most important lessons of all were from my parents and family who shared their joy of learning and always encouraged me to aim high and follow my dreams.

Table of Contents

List of Figures

List of Tables

Abstract

Understanding the Development and Growth of the Zebrafish (*Danio rerio*) Infraorbital Bones

By Carolyn Chang

Abstract: This study investigates the development of the neural crest derived infraorbital bones of the zebrafish (*Danio rerio*). Located around the underside of the orbit, the infraorbital bones ossify intramembranously in a set sequence and are closely associated with the lateral line sensory system. I conducted detailed analyses of the condensation to ossification phases of development of these bones, analysed infraorbital bone development via a series of skeletogenic condensation laser ablation experiments, and the neuromasts associated with the infraorbital bones were ablated at multiple time-points in order to investigate their highly debated inductive potential for infraorbital ossification. The results of this study highlight the developmental robustness of the infraorbital bones. The recovery of ablated structures demonstrates rescue mechanisms that allowed for the series to develop normally following perturbation. The mechanisms of developmental robustness should be investigated further as the infraorbital bones can be used to increase understanding of intramembranous bone patterning.

August 22, 2013.

List of Abbreviations

AP – alkaline phosphatase

BMP – bone morphogenic protein

CFP – cherry fluorescent protein

Dpf – days post fertilization

EtOH - ethanol

IO – infraorbital

SL – standard length

NBF – neutral buffered formalin

PBS – phosphate buffered saline

PC – principal component

PFA – paraformaldehyde

SD – standard deviation

TUNEL - Terminal deoxynucleotidyl transferase dUTP nick end labeling

ZIRC – zebrafish international resource center

Acknowledgments

First, I would like to thank my supervisor Tamara Franz-Odendaal. You have given me the opportunity to complete this project and have provided support, guidance, knowledge, and constructive criticisms throughout this entire degree. You have consistently expected the best quality of work from me, which has strengthened my critical thinking, independent research and writing skills immensely. You have been a mentor and role model for me, for which I will be forever grateful.

To my supervisory committee, Timothy Frasier and Tanya Peckmann, I thank you for providing a critical sounding board and insight as experts in your fields. Your perspectives have strengthened this project and have encouraged me to think outside of the box. Thank you. I would like to thank Andrew Gillis for your insight, advice, and assistance (including some reagents) which helped to guide my experimental design, analysis and interpretations. Dominique Adriaens, thank you for providing feedback and advice in the latter stages of my project, especially your suggestions regarding analysis methods. Shannon Fisher, thank you for providing me with transgenic zebrafish to use for my project.

To the members of the Franz-Odendaal Bone Development Lab, I thank you for providing a supportive and enjoyable atmosphere. In particular I would like to thank Megan Dufton and Sewvandini Atukorala for being my fish room partners and always being there the talk about experiments and fish problems. I would like to thank Bev Hymes for fish care and staining as well as James for sharing his TUNEL protocol.

1.0   Introduction

1.1 The Teleost Skull

Fish inhabit an impressive variety of environments and exhibit diversity in behaviour, morphology, diet, reproduction, and in their skeletons (Nelson, 1976). There are approximately 25,000 fish species in the phylum Chordata, subphylum Vertebrata within five distinct existing classes (Ostrander, 2000). Teleosts fishes, or bony fishes, are the most numerous and represent 96% of all fish (Ostrander, 2000). Teleosts are extremely diverse, with 38 orders, 426 families and 4064 genera (Figure 1) (Ostrander, 2000).

The teleost skeleton serves many important functions such as providing structural support, protection, locomotion, buoyancy, and it is also involved in feeding and respiration (Ostrander, 2000). In addition to these functions, the teleost skeleton is also involved in the physiological processes of growth and mineral homeostasis (Ostrander, 2000). The variety of fish skeletons reflects a variety of life history strategies, and in particular, the diversity of the skull is pronounced (e.g. Hildebrand and Goslow, 2001; Farrell et al., 2011). The skull of teleosts is complex, as it is an assemblage of a number of bony and cartilaginous elements joined by many joints and connections into a single structural unit that allows for a high degree of movement (Ostrander, 2000; Hildebrand and Goslow, 2001). Teleost skulls vary in terms of the number of bones, types of bones and in the types of bone articulations (Hildebrand and Goslow, 2001). However, despite this diversity, the teleost (and all vertebrate) skulls have an embryonic origin from the neural crest and paraxial mesoderm similar to other vertebrates (chick: Couly et al., 1998; mouse: Jiang et al., 2002; zebrafish: Kague et al., 2012).
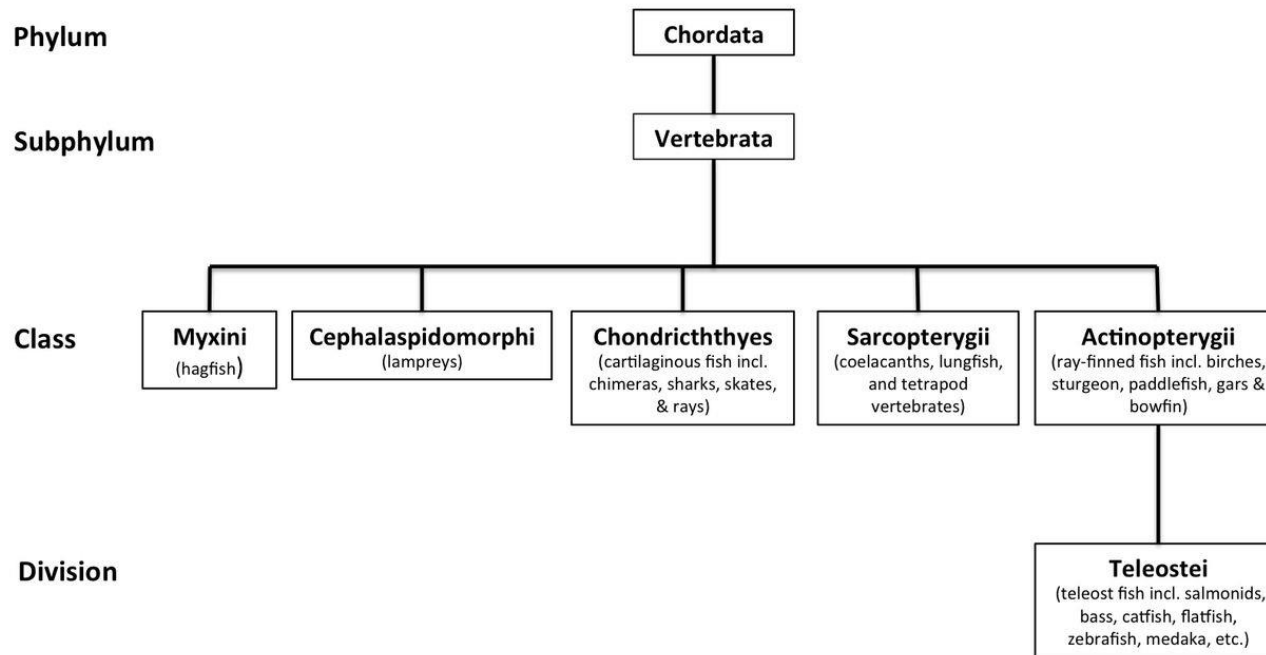
Figure 1. Ancestral and derived categories of fishes (modified from Nelson, 1994).

1.2 The Neural Crest Contribution to the Teleost Skull

The neural crest is located in the neurulating embryo as a ridge between the epidermal and neural ectoderms (Hall and Horstadius, 1988). Following neurulation the ridge resembles a cell mass that separates the two halves of the spinal cord dorsally (Hall and Horstadius, 1988). Within this cell mass are neural crest cells, which migrate away from the neural ectoderm to many areas of the body and differentiate into a number of types of tissues and organs such as sensory, pigment, endocrine and connective tissues (Hall and Horstadius, 1988).

Emerging from the diencephalon, midbrain and hindbrain in distinct populations or streams of cells, cranial neural crest cells are uniquely capable of differentiating into the cartilages, bones and connective tissues that comprise the skull (Hall and Horstadius, 1988). Specific to the teleost skull (i.e. zebrafish), the neural crest contributes to the olfactory, orbital, otic and opercular bones (with the exceptions of the kinethmoid, posterior portion of the frontal bone, parasphenoid, epioccipital, parietal, posttemporal), as well as the mandibular, palatoquadrate, hyoid anterior and branchial arches (with the exception of the ceretobranchial which is of mixed origin) (Kague et al., 2012).

The regulation of neural crest cell morphogenesis after migration comes from internal and external factors including genes, morphogens, growth factors and environmental signals (Henderson and Carter, 2002).

1.3 Teleost Skull Development

1.3.1 Two Developmental Processes of Ossification

In general, bone matrix is deposited by bone forming cells. Mono- or multi-nucleated osteoclasts are responsible for bone removal (i.e. during bone remodeling). Teleost bone is vascularized and is usually cellular (containing osteocytes); however in more derived teleosts, the bone can be acellular, lacking osteocytes (Witten, 1997). During bone formation, osteoblasts either secrete bone matrix becoming entrapped within the matrix forming cellular bone or osteoblasts remain on the periphery of the bone matrix and form acellular bone (Witten, 1997). Zebrafish have cellular bone (Cubbage and Mabee, 1996).

The bones of the skull ossify through two distinct developmental processes (Hall, 2005). Bone can develop through a direct ossification type, intramembranous ossification, where bone replaces a fibrocellular model directly in the membrane. Alternatively, bone can also develop indirectly through cartilage replacement, in which bone replaces a cartilage model. Although not the most common ossification type in the zebrafish skull, thirty of the seventy-four bones of the zebrafish skull ossify intramembranously (Cubbage and Mabee 1996). Most bones that develop intramembranously are neural crest derived, and it is this form of ossification that is the focus of this thesis.

1.3.2 Skeletogenesis and Induction

The development of the skeleton, skeletogenesis, involves a step-wise process where each step is dependent on the previous step and involves different cellular processes (such as migration, adhesion, proliferation, and growth) that are

each under different genetic controls (Hall, 2005). Three major developmental processes occur during skeletogenesis: epithelial-mesenchymal tissue interaction, condensation of mesenchymal cells, and differentiation; each are introduced below as described by Hall (2005).

The induction of mesenchyme first begins through an epithelial-mesenchymal interaction. This interaction can take place either before, during or after migration of mesenchymal cells and serves several functions during skeletogenic development: localization of skeletogenic mesenchyme provides an inductive signal for differentiation, allows for differentiation to begin, and sets the basic number of progenitor cells for the skeletal element.

The condensation phase follows induction of skeletogenesis and in this phase the building blocks, the mesenchymal cell condensations, of the bones form. The condensation phase enables selective regulation of genes to occur in order to specify chondro- or osteogenesis. As such the process of condensation formation is complex and involves the expression and regulation of many genes, transcription factors and proteins. The condensation phase consists of multiple steps: initiation, boundary establishment, cell adhesion, proliferation, growth, and cessation of growth. The latter two steps occur with the down-regulation of cell adhesion molecules and genes that control proliferation. Following condensation formation, overt differentiation of skeletogenic cells occurs. This is the result of the up-regulation of genes and transcription factors associated with skeletogenic differentiation: bone morphogenic proteins (*BMPs*), *Wnt* signaling, *Msx1* and

Msx2, Runx-2, and *Hoxa-11, 12, 13* all promote osteoblast differentiation (Hall 2005; Franz-Odendaal 2011). .

In addition to these fundamental steps in skeletogenesis, mechanical forces also play an important role. At the cellular level mechanical forces can influence cell shape, cell pressure, cilium bending, temperature changes, energy potentials and production and assembly of extracellular matrix components (reviewed in Carter et al., 1998). These cellular changes due to mechanical forces can subsequently have an effect at the molecular level through cytoskeletal damage or disruption, integrin binding, growth factors, and stretch activated ion channels all of which can affect cell activities (reviewed in Carter et al., 1998). The timing of ossification of elements in teleosts coincides with the mechanical forces being exerted on the elements by inserted or adjacent muscles, tendons or ligaments (e.g. in; catfish: Adriaens and Verraes, 1998; zebrafish: Danos and Staab, 2010). The effect of mechanical stimulation on ossification has been experimentally tested in the avian skull in an experiment done by Hall (1986) where, *in vitro*, the quadratojugal bone was mechanically stimulated by movement against the quadrate resulting in a switch from osteogenesis to chondrogenesis.

The condensation to differentiation phase of bone development includes a complex series of developmental steps each relying on localized temporal signaling. The formation of the teleost skull therefore requires an elaborate regulation and synchronization in the timing of condensation initiation, growth and differentiation between all the condensation centers of all the bones, many of these require further elucidation.

1.4 The Zebrafish (*Danio* rerio) Model

The zebrafish, *Danio rerio*, is a small freshwater teleost fish of the cyprinid family in the class Actinopterygii (ray-finned fishes): the lineages leading to cyprinids and mammals split approximately 450 million years ago (Meyer et al., 1993; Nüsslein-Volhard et al., 2002). The zebrafish is a frequently used model vertebrate organism in a wide variety of biological studies (e.g. Nüsslein-Volhard et al., 2002; Schilling and Webb, 2007). *Danio rerio* shares many features with other vertebrates such as cell and tissue types (for e.g. skeletal, muscle, nervous, immune, cardiovascular, digestive and skin) and embryological stages, but zebrafish also display many unique characteristics that help with understanding evolutionary patterns and processes (Lieschke and Currie, 2007; Schilling and Webb, 2007). There is also a generally conserved position and timing of neural crest cell migration among vertebrates including the zebrafish (Schilling and Webb, 2007). There are 74 bones in the zebrafish skull with the majority forming through cartilage replacement (Cubbage and Mabee 1996). For this investigation the zebrafish model will be used since it possesses many of the same skeletal cell and tissue types as other vertebrates as well as similar bone formation processes (Hall, 2005). Here, I will focus on one set of intramembranous bones, the infraorbital bones.

1.5 The Infraorbital Bones

The infraorbital (IO) bones are a series of intramembranous, neural crest derived bones located around the underside of the eye in teleosts (Figure 2). This series of bones is a component of the circumorbital series of bones that surround the eye. The circumorbital series also includes the supraorbital bones above the eye (Cubbage and Mabee, 1996). The IO bones are named, infraorbital one through five, according to their
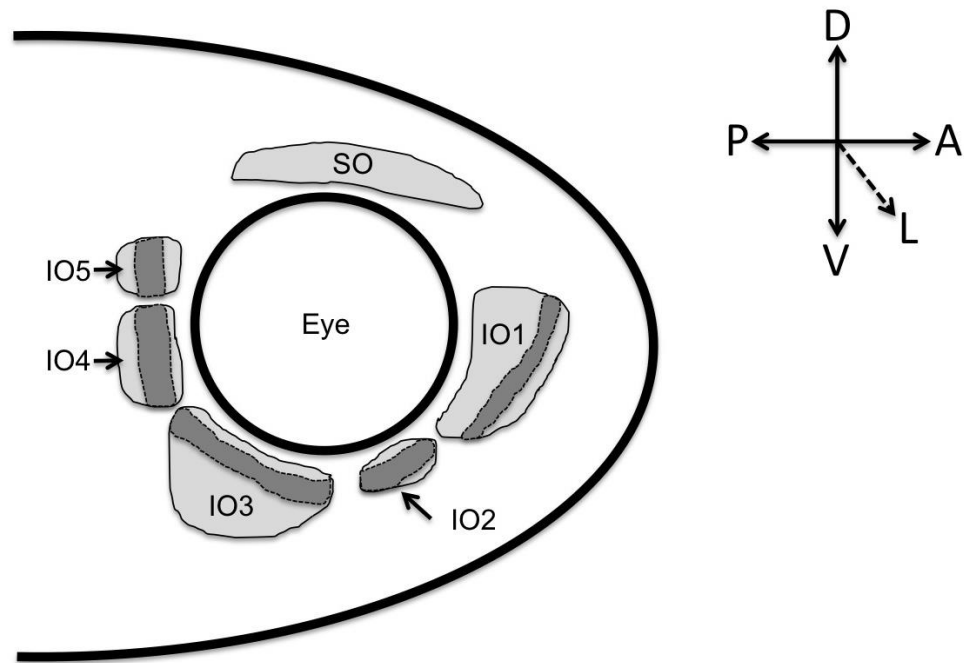
Figure 2. A schematic showing the infraorbital (IO) bones and the supraorbital bone (SO), a component of the circumorbital bone series in the zebrafish (*Danio rerio*) skull. Flat components of each bone are shaded in light grey. Lateral line canals are demarcated by darker shading as well as dashed lines. Anterior (A), posterior (P), dorsal (D), ventral (V) and lateral (L) direction are indicated in the top right. Schematic is modified from Nelson (1969) as well as Cubbage and Mabee (1996).

position in the skull from anterior to posterior. The function of the eye-surrounding bones has not yet been directly investigated; however with such a close association to the eye these bones likely serve a protective or supportive role for the eye. These bones also house the cranial lateral line system. The lateral line is a sensory system that allows fish to sense water movement and pressure gradients and is composed of neuromast mechanosensory receptors distributed along the head and trunk of fish. The lateral line canals that house the neuromast sensory receptors are found in many intramembranous skull bones, including the infraorbital bones (Cubbage and Mabee, 1996). The organization of lateral line canals has been described by Webb in Ostrander (2000) and ranges from a simple reduced pattern to a complex pattern with extensive branching: the zebrafish exhibits a narrow-simple pattern of lateral line canals (Ostrander, 2000).

The infraorbital series of bones are found in generally the same position and arrangement in teleosts and range in number from five to seven bones (Nelson, 1969). The number of neuromasts that are found in lateral line canals associated with these bones is also similar in teleosts (Nelson, 1969). It has been suggested that the primitive teleost condition was seven infraorbital bones with more than seven neuromasts distributed among the canals and that a reduction in the number of IO bones and number of neuromasts occurred during the evolution of teleostean fishes (Nelson, 1969). The reduced number of infraorbital bones seen in cyprinids (namely five) is thought to be due to the fusion of IO bones in the middle of the series (i.e. IO3-IO5) (Nelson, 1969).

The development of the zebrafish infraorbital bones has only once been described by Cubbage and Mabee's (1996) highly cited description of the entire zebrafish skull. While this report provided a thorough description of adult IO morphology, it only

provided a brief explanation of infraorbital one development and did not include any detail regarding the development of the remaining IO bones. The infraorbital bones ossify in a set sequence starting at around 6.0 mm standard length (SL) through to 20.0 mm SL (Cubbage and Mabee, 1996). First, infraorbital one (also known as the lachrymal) ossifies, followed by the concurrent ossification of infraorbitals three and five (Cubbage and Mabee, 1996). Then infraorbital four ossifies, and finally infraorbital two, ossifies. IO2 is also the final bone to undergo ossification in the zebrafish skull (Cubbage and Mabee, 1996). The morphology of each infraorbital bone varies in both shape and size and these have been generally described by Cubbage and Mabee (1996) and are summarized below.

Infraorbital one bone (IO1) is located at the anterodorsal edge of the orbit (Figure 2) and first appears as two slivers of bone. As the bone grows these two slivers fuse together and the IO1 bone takes on an irregular disc shape, becoming more elongate as more bone is laid down. Two foramina are found on the anterodorsal edge of IO1 and the infraorbital lateral line starts to ossify anterior to these foramina. The IO1 bone meets with infraorbital two at its ventral edge. When IO1 has finished ossification it has three pores: the first pore opens dorsally below the nasal sac and posterodorsal to the anterior maxillary barbel, the second pore opens laterally off the canal immediately posterior to the anterior maxillary barbel, and the third pore opens where IO1 meets infraorbital two.

Infraorbital two (IO2) is found at the posteroventral edge of IO1 and is situated ventral to the orbit and anterior to infraorbital three (IO3). IO2 shares pores with IO1 and IO3 and contains one neuromast foramen.

Infraorbital three (IO3) is the largest infraorbital bone and spans the ventral edge of the orbit; it is positioned between IO2 and infraorbital four. The infraorbital lateral line lies across the length of IO3 and a lateral line pore is found at each end of the bone, with an additional pore at the center of IO3. Two neuromast foramen are found in IO3.

Infraorbital four (IO4) is located at the posterior edge of the orbit, situated ventrally to infraorbital five. IO4 has one neuromast foramen and shares lateral line pores with IO3 and infraorbital five. IO4 of zebrafish is thought to be homologous to the fifth infraorbital of basal teleosts.

Infraorbital five (IO5) is found at the posterodorsal edge of the orbit and is anterolateral to the sphenotic. One lateral line pore is found at the dorsal edge of IO5 and a second pore is found where IO5 meets IO4. One neuromast foramen is found in IO5.

Other than the above description which included one schematic of the series and two figures showing only IO1, there have been no other descriptions of these bones in zebrafish. The development and growth of the zebrafish infraorbital bones remains to be elucidated.

1.6 Cranial Lateral Line

The functional unit of the lateral line system is the neuromast. The neuromast is a mechanosensory receptor organ that is similar to that of the stereocilia of the inner ear of humans. At the core of the neuromast are mechanosensory hair cells that are surrounded by support cells and mantle cells which secrete the cupula that surrounds the hair cells (Figure 3) (Ghysen et al., 2004). The mechanosensory hair cells are innervated by sensory neurons (Ghysen et al., 2004).

Two kinds of neuromasts have been described in teleosts (Webb and Shirey, 2003). Presumptive (primary) canal neuromasts are found enclosed within the lateral line canals and superficial (secondary) neuromasts are found in the skin (Webb and Noden, 1993; Baker and Bronner-Fraser, 2001). Presumptive canal neuromasts and superficial neuromasts can be differentiated based on size and shape (Webb and Shirey, 2003). The superficial neuromasts have a small and round shape with hair cells spread evenly across the neuromasts. Presumptive primary canal neuromasts and superficial neuromasts become distinct during the latter part of the larval period, which ends at approximately 10.5 mm SL (Parichy et al., 2009). These two types of neuromasts also have different biochemical and functional properties. Canal neuromasts are able to interact with the surface through pores in the bony canals (Baker and Bronner-Fraser, 2001). The differences in the two types of neuromasts become apparent over the course of their development, which involves migration of neuromast primordia, maturation and canal enclosure (in the case of primary neuromasts (Raible and Kruse, 2000). Zebrafish possess both types of neuromasts (Raible and Kruse, 2000; Webb and Shirey, 2003).
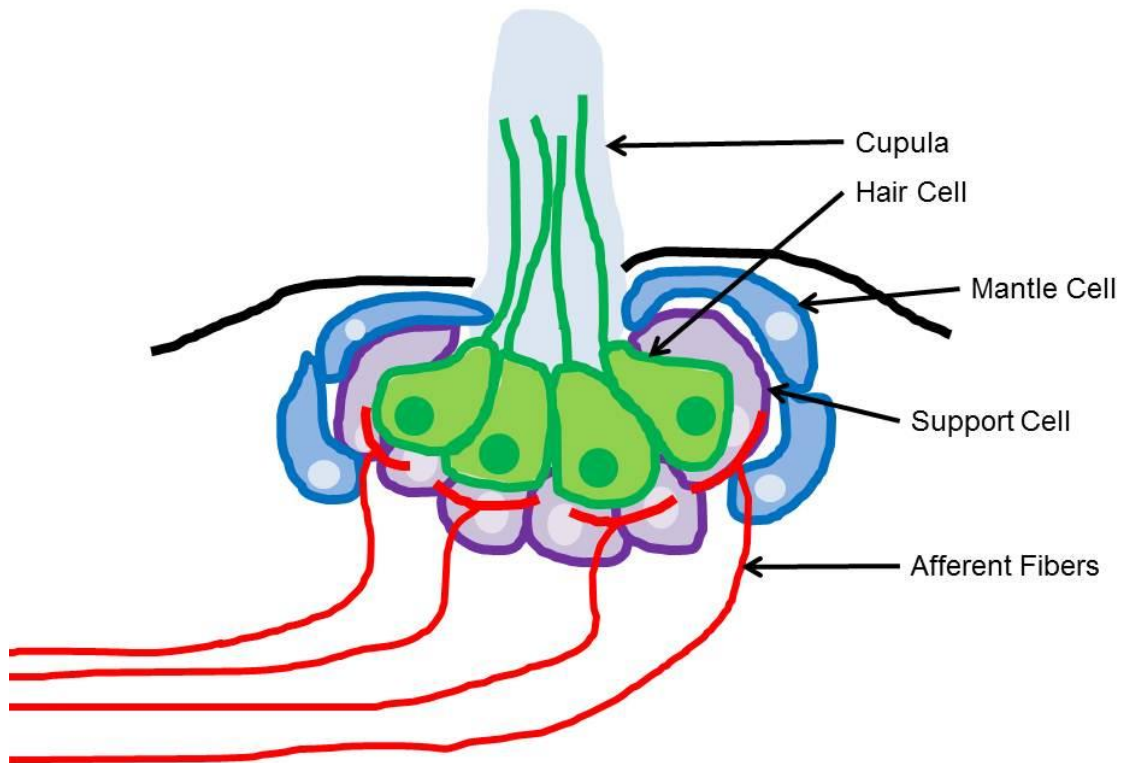
Figure 3. **Schematic of a neuromast showing the different cell types comprising the neuromast organ. Hair cells (green) are innervated by afferent nerve fibers (red). Mantle cells (blue) secrete the cupula (grey) that surround the hair cells and also separate the neuromast from the epidermis (black). Support cells are shown in purple. Schematic modified from Ghysen and Dambly-Chaudière (2004).**

1.6.1 Cranial Lateral Line Development

The cranial lateral line system develops from ectodermal placodes (Baker and Bronner-Fraser, 2001). Vertebrates have five types of placodes on their heads: lens placode, nasal placode, trigeminal placode, otic placode and epibranchial (4) placodes (Webb and Noden, 1993). There are also many lateral line (dorsolateral) placodes found only in anamniotes (Webb and Noden, 1993). Cranial placodes are transitory, thickened patches of ectoderm usually distributed bilaterally (Baker and Bronner-Fraser, 2001). Found in distinct positions on the head, placodes form as a result of inductive interactions with different regions of the neural tube (Jacobson, 1966; Jacobson and Sater, 1988). Placodes form through invagination and/or delamination and are precursors to other unique cell types like sensory receptors; they contribute to the peripheral nervous system as well as to the majority of all the primitive cranial sensory system of vertebrates (e.g. Webb and Noden, 1993; Baker and Bronner-Fraser, 2001). The lateral line system is derived from multiple placodes (more than six); specifically the cranial lateral line system is derived from the dorsolateral placodes (Baker and Bronner-Fraser, 2001).

Lateral line placodes migrate and deposit lateral line organs, which consist of both the neuromast and the innervating nerves, along the head (Stone, 1922; Baker and Bronner-Fraser, 2001; Sepède et al., 2002; Webb and Shirey, 2003). The migrating placode is polarized with one side containing the migrating neuromast primordium and the other housing the contribution to the ganglia (Baker and Bronner-Fraser, 2001). The migrating primordium was thought to deposit primary neuromasts that give rise to secondary neuromasts (Stone, 1922; Baker and Bronner-Fraser, 2001), however, more recent work has shown secondary neuromasts arising from a second migrating

primordium (Sepède et al., 2002). Neuromast maturation and enclosure within the walls of the bony lateral line canals occurs during the juvenile (10.5 mm SL) to adult period of development (Webb and Shirey, 2003).

1.6.2 Lateral Line Canal Wall Formation

Using SEM analysis, Webb and Shirey (2003) provide the only early description of the pattern and growth of the cranial lateral line neuromasts in post-embryonic zebrafish. The analyses however, were specific to the canals of the supraorbital and mandibular bones, and canals in other bones were only briefly investigated. These authors conclude that the morphology and pattern of development of the cranial lateral line canals in zebrafish is similar to that of other teleost species, however importantly, the timing of canal formation with respect to neuromast maturity is different in zebrafish.

Webb and Shirey (2003) also describe four developmental stages of canal neuromast development in the zebrafish, which are briefly summarized here. Stage one involves the presumptive canal neuromast sitting on the epithelium above an underlying intramembranous bone (for example an infraorbital bone). The second stage of neuromast development consists of two sub-stages where the neuromast first sits in a shallow depression of epithelium, an epithelial groove; this is followed by ossification of bony canal walls that extend upwards from the underlying intramembranous bone. The third stage of neuromast development occurs as the canal is enclosed by an epithelium, which fuses over the neuromast. In the last stage of canal neuromast development, canal walls are reported to fuse over the neuromast to form a canal segment with a completely ossified canal roof. The lateral line canals are generally formed between the juvenile stage of development (10.5 mm SL) and adulthood (reproductive maturity/ 4 months of age).

1.6.3 Neuromast induction of lateral line canals

Since skeletogenesis involves epithelial induction (Hall, 1981; Hall and Van Exan, 1982; Tyler and McCobb, 1980; Takahashi et al., 1991; Webb and Shirey, 2003) and since placodes (including neuromasts) arise from epithelia (e.g. Webb and Noden, 1993; Baker and Bronner-Fraser, 2001), it has been debated that placode-derived neuromasts have inductive potential with regards to inducing bony canal wall formation (Devillers, 1947; Lekander, 1949; Kapoor, 1970; Webb and Shirey, 2003). Previous discussion (reviewed in Kapoor, 1970) has made reference to the inductive capabilities of the neuromast receptor organs of the lateral line system in teleosts. The neuromasts were discussed to be likely to induce the formation of the canal since they form prior to the formation of the canals in many teleosts (reviewed in Kapoor, 1970). However, in some species (e.g. *ophicephalus punctatus* Bloch), the bony canals were present prior to neuromast formation (reviewed in Kapoor, 1970). Additionally, researchers argued that the neuromasts do not directly induce canal wall ossification, but change the mechanical (Moodie, 1922) and biochemical (Westoll, 1937) environment which triggers ossification. A large portion of this literature was based on inferences made from observations, but only one experiment has been documented to directly test these inferences. Devillers (1947) ablated the neuromasts of the supraorbital canal in salmonids and observed abnormal morphogenesis of the frontal bone (cited in Webb and Shirrey, 2003).

In the zebrafish, the neuromasts have been suggested to induce the formation of the bony lateral line canal walls during the second stage of canal development when the neuromast sitsa in an epithelial groove for an extended period of time (Webb and Shirey, 2003).

There is a zebrafish mutant, *dog-eared*, in which the anterior lateral line neuromasts are reduced in size or missing (Kozlowski et al., 2005). This mutant has a mutation in the *eya1* gene (Whitfield et al., 1996; Kozlowski et al., 2005). Although abnormal jaw development was also observed, the extent to which the craniofacial skeleton is affected is unknown since the *dog-eared* mutant does not survive to adult stages (Whitfield et al., 1996; Kozlowski et al., 2005).

The relationship between the neuromast and the lateral line canal has not been tested in zebrafish or in any bony fish since DeVillers (1947). In fact, studies investigating the inductive potential of the neuromast on canal wall ossification are from more than 40 years ago (Devillers, 1947; Lekander, 1949; Kapoor, 1970) with the exception of one study from ten years ago (Webb and Shirey, 2003) which did not directly test inductive abilities. Presently, there is a need to increase understanding of the development of lateral line canal walls and any potential involvement of neuromasts in their formation.

1.7 Objectives

This study aims to investigate the development and growth of the zebrafish (*Danio rerio*) infraorbital bones and the relationship between these bones and the lateral line canal neuromasts. These relationships will be elucidated through the completion of three main research objectives:

Specific Objectives

1.   Describe the growth of the infraorbital bone series.

2.   Determine whether individual developing infraorbital bones affect the development and/or growth of neighbouring IO bones.

        Hypothesis: I hypothesize that individual developing IO bones do affect the development and/or growth of neighbouring IO bones. If this is true then disruption of one IO bone's development will result in changes to the development and/or growth of adjacent bones in the series.

3.   Determine whether developing canal neuromasts influence the development of the bony canal walls surrounding them.

        Hypothesis: I hypothesize that developing canal neuromasts do affect the mineralization of the bony canal walls surrounding them. If this is true then the removal of a canal neuromast results in a loss of induction of canal wall mineralization.

Significance:

      The infraorbital (IO) bone series consists of neural crest derived intramembranous bones. The development of this IO series must involve a high degree of regulation and synchronization in order for the sequence of IO bone development, shape and location to be consistent amongst teleosts. There is still much to be understood regarding regulation and synchronization involved in skeletogenesis, particularly of intramembranous bones. The results of this study will provide a fundamental framework for further investigations into this regulation. Additionally, investigating the role neuromasts have in IO bone development will contribute to the long-standing, unresolved debate of neuromast induction of ossification. This will be the first study since Webb and Shirey's (2003) publication ten years ago. Understanding the relationship between neuromasts and infraorbital bones will also contribute to understanding the relationship between soft tissues (i.e. neuromasts) and hard tissues (i.e. bone).

2.0   Materials and Methods

2.1 Biological Material, Zebrafish, *Danio rerio*

Wild-type zebrafish (*Danio rerio*) embryos were bred in our laboratory from AB stocks sourced from the Zebrafish International Research Center (ZIRC) and reared following standard conditions to time-points required for the experiments in this study.

Transgenic zebrafish (*Danio rerio*) embryos with cherry fluorescent protein (CFP) expressed in bone cells were generously provided by Dr. Shannon Fisher at the University of Pennsylvania. This transgenic construct permanently labels cells that express *osterix*. During osteoblast differentiation, the zinc-finger transcription factor *osterix* is involved in the differentiation of pre-osteoblasts into mature osteoblasts. Thus, all bone cells will have *osterix* expression which is permanently marked with CFP. These *osterix* embryos were received in our laboratory at five days post-fertilization.

All fish used in this study were raised in the Mount Saint Vincent University fish facility. All protocols follow Canadian Council on Animal Care guidelines, which were annually reviewed by the SMU-MSVU Animal Care Committee.

2.2   Staging Zebrafish

All zebrafish used in this study were staged according to days post fertilization for time-points up to five days post fertilization (dpf) following Parichy et al., (2009). Fish were reared at 28.5°C as in Parichy et al., (2009). After five dpf, zebrafish were staged according to their standard length (SL), which is defined as the distance from the snout to the caudal peduncle (Parichy et al., 2009). SL was measured using the Nikon NIS Imaging Software (for specimens less than 10 mm SL) or with a standard ruler (for

specimens larger than 10 mm SL). Prior to measurement, all zebrafish were anaesthetized by immersion in a 0.01% solution of MS222 (Ethyl-3-aminobenzoate methane sulfonic acid salt, Sigma E10521) made in fresh zebrafish system water. Fish were monitored for the signs of anaesthesia: cessation of opercular movements and loss of caudal fin reflex.

2.3 Specimens for Bone Stained Growth Series

A growth series of bone stained specimens was prepared to describe the growth and development of the infraorbital bones. Zebrafish specimens were collected at 20 developmental time-points (Table 1) from 8.0 mm SL to adulthood (250 mm SL). Growing zebrafish were staged regularly and when fish had reached the desired developmental stage they were euthanized through immersion in a 0.1% solution of MS222 made in fresh zebrafish system water. Following euthanasia, specimens were fixed in 10% neutral buffered formalin (NBF) (Fischer Scientific 23-245-685) overnight at room temperature. Following fixation specimens were either prepared for storage or immediately bone stained. For storage, specimens were rinsed in distilled water and put through a graded ethanol (EtOH) dehydration series to 70% EtOH. Some specimens were also acquired from the lab's stock of previously fixed fish for general use (stored in 70% EtOH). These fish were staged post-fixation and their dates of birth and death were noted.

Table 1. Summary of zebrafish fixed for bone stain growth series (extended table in Appendix 1, Table 1).

Time-Point (mm SL)	Number of Specimens	Specimen Age (days)
8.0	3	43
9.5	2	41
9.0	3	40-104
9.5	3	35-60
10.0	5	34-43
10.5	4	43-104
11.0	5	40-432
11.5	6	40-104
12.0	5	40-104
12.5	5	48-65
13.0	4	48-104
13.5	4	54-104
14.0	5	60-104
14.5	6	40-104
15.0	3	96-434
15.5	2	48-74
16.0	2	104-195
16.5	5	74-118
17.0	5	96-428
18.0	5	137-428
20.0	1	195
22.0	1	195
25.0	3	141
Total	87	

2.4   Specimens for Alkaline Phosphatase (AP) Stained Growth Series

In order to describe osteoblast activity prior to mineralization, an alkaline phosphatase (AP) stained growth series was prepared following the protocol of Edsall and Franz-Odendaal (2010). Zebrafish specimens were collected at ten developmental time-points (Table 2) from 6.0 mm SL to 20.0 mm SL. Zebrafish were staged and when fish had reached the desired developmental stage they were euthanized through immersion in a 0.1% solution of MS222 made in fresh zebrafish system water. Following euthanasia, specimens were fixed in 4% paraformaldehyde (Sigma P6148) made in 0.01M phosphate buffered saline (PBS) (Appendix 2), pH 7.4, at 4°C overnight. Following fixation specimens were either stored in 0.01 M PBS, pH 7.4, at 4°C until staining or rinsed in 0.01M PBS and immediately stained.

Table 2. Summary of zebrafish stained for alkaline phosphatase (AP) (extended table in Appendix 1, Table 2).

Time-Point (mm SL)	Number of Specimens	Specimen Age (days)
6.0	5	25
7.0	7	25-32
8.0	6	32-55
9.0	7	32-55
10.0	6	55
11.0	7	55
12.0	5	55
13.0	5	40-55
14.0	5	40-90
15.0	5	40-90
16.0	5	40-90
17.0	5	90
18.0	5	90
19.0	5	90
Total	78	

2.5 Alkaline Phosphatase (AP) Staining

Prior to alkaline phosphatase (AP) staining all specimens were descaled and degutted. The following modifications to the Edsall and Franz-Odendaal (2010) protocol were made: a more concentrated AP substrate solution was used which yielded more effective staining. Specimens were washed in distilled water (three washes at 15 minutes each) and then incubated in a tris-maleate buffer solution, pH 8.3 {0.605g (0.2 M) trizma base (Sigma 93362), 0.55g maleic acid (0.19 M) (Fischer Scientific 064402), 25ml distilled water} for one hour at room temperature. The following steps all took place in the dark in a glass container. Specimens were incubated in an AP substrate solution {1 ml 20µM (10mg/ml) napthol-AS-TR-phophate (Sigma N6125) in N, N-dimethylformamide (Sigma D4551), 8mg Fast Blue B (Sigma D9805), and 10ml tris-maleate buffer, pH 8.3} in a glass container for one hour. Following the AP substrate step, the specimens were washed (three washes at 15 minutes each) in a saturated sodium borax {sodium tetraborate decahydrate (Sigma B9876)} solution. The specimens were then transferred to a bleaching solution of 10% hydrogen peroxide (drug store) in 1% potassium hydroxide (Sigma 1767) overnight. The following day, all specimens were cleared with a trypsin digestion {1% trypsin (Fischer Scientific 9002-07-7), 2% sodium tetraborate decahydrate (Sigma B9876) in distilled water}. Once digested specimens were stored in 80% glycerol in 100% ethanol at 4°C in the dark.

2.6   Laser Ablation System

Laser ablation was carried out using a MicroPoint® Ablation Laser System, which uses a nitrogen laser attached to a Nikon Eclipse 50i compound microscope. Targeted cells are aligned using the microscope cross-hairs and ablated with the laser.

Prior to all laser ablation experiments, the laser was calibrated and the dye cell was checked for freshness using a mirrored microscope slide. The width of the beam was also calibrated. This regular calibration allowed for accurate ablations.

2.7   Mounting Equipment

For all ablation experiments, zebrafish were individually mounted on a large glass depression slide in fresh, 3% methyl cellulose (Fischer Scientific S80080). Zebrafish were positioned laterally so that their right lateral side was facing upwards using a flame-sterilized tungsten needle.

2.8   Condensation Ablation Experiment

The *osterix* transgenic zebrafish were raised following standard rearing conditions in the fish facility. Since only a small (N=8) number of the embryos survived to reach the juvenile stage of development, it was decided that only one infraorbital bone would be targeted for condensation ablation. Of these transgenic zebrafish some were chosen for ablation (N=4) and the remaining specimens were controls (N=4). Infraorbital five was selected since it develops second in the IO series (with IO3) and it forms a small condensation as it is one of the smallest IO bones. Once *osterix* fish reached approximately 8.0 mm SL they were regularly examined for the presence of the infraorbital five (IO5) condensations. This starting time-point for monitoring was

determined based on the results from the AP and Alizarin Red S growth results (Section 3.0). For example, IO5 osteoblast activity is first seen around 11.0 mm SL, so monitoring for IO5 bone cells forming a condensation began at 8.0 mm SL. Monitoring was conducted by anaesthetizing the fish, mounting them as described above and viewed them on a Nikon Eclipse 50i compound microscope and the CY3 filter (excitation: 530-560, emission: 573-648; Nikon Intensilight C-HGFI system). In the case that an IO5 condensation of bone cells was observed, the fish underwent laser ablation. If no condensations were visible, the fish was removed from the methyl cellulose, rinsed in fresh zebrafish system water, and left to recover from anaesthetization in a container of zebrafish system water. Following recovery the fish was be returned to the fish facility. Fish would undergo this monitoring procedure every 2-3 days until the IO5 condensation was observed.

When a condensation was observed, the IO5 condensation was aligned in the center of the objective lens cross hairs and the fine adjustment knobs were used to focus on the condensation cells (adjusting depth). Once alignment was finished a photograph of the condensation was taken using a Nikon S-Vi1 camera. Following photography, the laser was pulsed at the condensation using the laser ablation system`s pedal attachment. The condensation was considered ablated when fluorescence could no longer be observed in the IO5 condensation. At this time, another photograph was taken. The fish was then removed from methyl cellulose, rinsed in fresh zebrafish system water, and left to recover in a container of fresh system water. Following recovery the fish was returned to the fish facility.

Follow-up observations were carried out at multiple time-points: 24 hours, 5 days, two week, one month and two months post-ablation. This follow-up procedure involved the anesthetization of specimens and mounting of specimens on a glass depression slide, viewing and photography of the ablated IO5 region. Notes were made on the appearance of fluorescent bone cells in the IO5 region at each time point.

Once condensation ablation and control specimens reached adulthood they were anesthetized and then fixed in NBF overnight at room temperature. Following fixation specimens were dehydrated through a graded ethanol series to 70% EtOH for storage.

2.9 Neuromast Vital Dye Preparation

FM1-43FX (Invitrogen F35355) is a lipophilic vital dye that stains the plasma membrane of the hair cells of neuromast mechanosensory receptor cells (REF). Aliquots of FM1-43FX were prepared by suspending 100 µg of FM1-43FX in 200 µL of dimethyl sulfoxide (Fischer Scientific BP231-1) for a concentrated 0.5 µg/ µL (817 µM) solution of FM1-43FX. This concentrated solution was then diluted in fresh zebrafish system water for a working concentration of 3 µM (Moon et al., 2011).

For a working solution of 3µM, the 200 µL (817 µM) aliquot was added to 54.267 mL of zebrafish system water. Once made, stocks at working concentration (3 µM) were stored in the dark at -20°C. When zebrafish were ready for staining, frozen aliquots were then thawed to 28.5°C and then prepared as described above.

2.10   Neuromast Ablation

In order to determine whether IO canal neuromasts influence the ossification of canal walls, IO neuromasts were ablated at both larval and juvenile time-points (Figure 4). Wild-type zebrafish for the neuromast ablation experiment were bred and reared in our fish facility following standard rearing conditions until they had reached the desired developmental stage for ablation. The larval ablation was done once the first migration of IO canal neuromasts was complete at 5 dpf. The juvenile ablation was done during at the time-point immediately before neuromasts have been suggested to induce canal wall ossification (Webb and Shirey, 2003). For both IO3 and IO5 ablations, this time-point was at 10.0 mm SL (usually around 1-1.5 months post-fertilization).

Once zebrafish reached the desired time-point they were vitally stained through immersion in 3μM FM1-43X for 20 minutes in the dark at room temperature. Following staining, zebrafish were transferred to fresh zebrafish system water for rinsing. Zebrafish were individually anaesthetized using 0.01% MS222 and mounted on a glass depression slide.

Specimens were viewed using a Nikon Eclipse 50i compound microscope using FITC (Excitation: 460-500, Emission: 510-560) fluorescence emitted using a Nikon Intensilight C-HGFI system. The targeted neuromasts (Table 3) were then aligned with the ocular cross hairs and the fine adjustment knob. Once alignment was finished a photograph of the neuromast was taken using a Nikon DS-Vi1 camera and NIS Imaging Software. The laser was then pulsed using the system`s pedal attachment. The fluorescence diminished from the field of view as neuromast cells were ablated with the laser. This ablation was repeated until there were no fluorescing neuromast cells visible in the targeted region. Another photograph was taken after the ablation. Specimens were then removed from the

methyl cellulose solution, rinsed in fresh zebrafish system water and returned to a container of system water to recover from the procedure. Following recovery, specimens were returned to their tanks in the fish facility. Controls for the FM1-43 staining and mounting procedure were carried out. Control fish were vitally stained with FM1-43 following the same procedure used for ablation specimens, following this controls were anaesthetized in 0.01% MS222 and mounted in 3% methyl cellulose and imaged using FITC fluorescence. These specimens were then released from the methyl cellulose, rinsed and left to recover as in ablation specimens.

Table 3. Neuromast ablation treatment and control groups.

Treatment Group	Ablation Time-Point (age at ablation)	Neuromasts Targeted	Number of specimens
1	Larval (5 dpf)	Larval IO3 & IO4	N=20
2	Larval (5 dpf)	Control (No ablation)	N=20
3	Juvenile (10.0 mm SL)	IO3 Neuromasts	N=10
4	Juvenile (10.0 mm SL)	IO5 Neuromasts	N=20
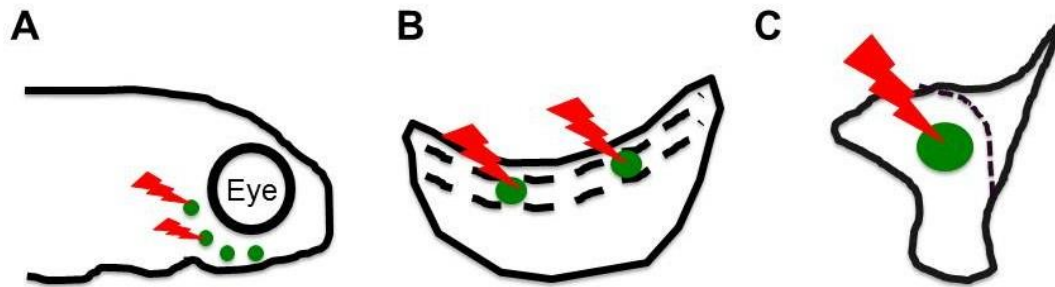
Figure 4. Schematic indicating the ablation in larvae of IO3 and IO4 neuromasts (A), the ablation of the two IO3 canal neuromasts in juveniles (B), and the juvenile ablation of the IO5 canal neuromast (C). All neuromasts are shown as solid green circles and ablations are indicated by red lightning bolts. Dashed lines represent the lateral line bony canals.

2.11 Follow-up on Neuromast Ablations

Specimens that underwent neuromast ablation and controls were observed at 24 hours and at 3-5 days post-ablation. For these follow-ups, specimens were vitally stained and mounted following the same procedure as for the neuromast ablation. Re-staining of the specimens was required as the vital FM1-43FX styryl dye leaves the specimen through naturally occurring cell division. Specimens were viewed under fluorescein isothiocyanate (FITC) fluorescence and photographed. Following this observation procedure, specimens were removed from the methyl cellulose, rinsed in fresh zebrafish system water and returned to a container of system water to recover from the procedure. Following recovery, specimens were returned to their tanks in the fish facility. After the final follow-up (3-5 days post-ablation), specimens were reared to adulthood following standard rearing conditions. Once at adulthood, they were fixed in NBF overnight at room temperature. Following fixation, specimens were dehydrated through a graded ethanol series to 70% EtOH at which point they were stored for future bone staining in order to assess the effects of neuromast ablation on the adult skeleton.

2.12 Histological Analyses of Neuromast Ablation

In order to evaluate the specificity of laser ablation technique for neuromast ablation and also to evaluate the extent of damage caused by the laser ablation, histological analyses were done comparing the neuromast before and after ablation. For these analyses, juvenile zebrafish that underwent neuromast ablation were euthanized and fixed in 4% PFA (Sigma P6148) in PBS overnight at 4°C at two time points; immediately following ablation and 3 days after ablation.. Following fixation specimens were rinsed in PBS, and were then decalcified in 10% ethylenediaminetetraacetic acid disodium salt

dihydrate (Sigma E5134), pH 7.4, for 4-5 days at room temperature. Following decalcification, specimens were embedded as follows. First specimens were processed through a graded EtOH dehydration series (25%, 50%, 70%, 80%, 90% to 100%), then specimens were rinsed in Citrosolve twice for 30 minutes at room temperature, and finally placed melted paraffin wax in warmed wax molds at 54°C overnight. The next day, the wax was changed and specimens remained in fresh wax at 54°C for two hours. Specimens were then embedded in fresh wax on an ice block and were oriented for coronal sectioning. Once embedded in hardened wax blocks sections were left to store (minimum for one overnight) at -20°C.

Embedded specimens were then sectioned on a microtome and were cut at 5μm in thickness. Sections were placed (alternating each serial section) on Aptes (Appendix 2, Sigma A3648) coated slides for TUNEL staining and Haupt's coated slides (Appendix 2) for Masson's Trichrome staining. Sections were incubated overnight at 38°C and were then stored at 4°C (Aptes sections) or room temperature (Haupt's sections).

Sections on Aptes coated slides were stained following a TUNEL staining protocol {Franz and Kidson, 1997; with modifications by Jabalee (personal communication)} for the detection of cell death. This protocol used the Roche *in situ* cell death detection kit (Cat. No. 11 684 817 910) which contained the following reagents: Alkaline phosphatase (AP) enzyme solution (TdT), label solution (fluorescein-dUPT), converter AP (anti-fluotescien antibody, AP). First slides were de-waxed twice in CitroSolve for ten minute washes. Next, slides were rehydrated in a graded ethanol rehydration to distilled water: 100% EtOH for 2 minutes, 90% EtOH for 2 minutes, 70% EtOH for 2 minutes, and 50% EtOH for 1 minute, and distilled water for 2 minutes. Following rehydration slides were predigested in 2X saline sodium citrate diluted from a

20X concentrate (Sigma S6639) warmed to 75°C for 20 minutes in a Coplin jar wrapped in aluminum foil. Following pre-digestion, slides were rinsed in distilled water for three five minute washes. Following washes, slides were dried and sections were circled using a hydrophobic pen to limit the spread of solutions away from sections. TdT buffer {30 mM Tris hydroxymethyl aminomethane (Roche 77-86-1), pH 7.2; 140 mM sodium cacodylate trihydrate (Sigma C0250); 1 mM cobalt (II) chloride hexahydrate (Sigma 255599)}, pH 7.4, was then applied to slides for 5 minutes. Next, the TdT buffer was removed from the slides and sections were encircled once again using the hydrophobic pen. The TUNEL reaction mixture (5 μL enzyme solution and 45 μL label solution) was then applied to the slides as well and label solution was applied to a negative control slide (to ensure staining was specific to cells undergoing apoptosis). Slides were incubated in a humidity chamber at 38°C for 1.5 hours. Following incubation slides were rinsed in distilled water for three ten minutes washes. Slides were then dried and sections were circled using the hydrophobic pen. A 5% goat serum (Sigma 9023) in 0.01M Tris-buffered saline {(75 mL distilled water; 1.2 g Tris; pH to 7.5); 0.9 g sodium chloride (EMD SX-0420-3)}, pH 7.4, was then applied to the slides for 15 minutes. Following this, the AP converter solution was applied to sections which were then incubated in a humidity chamber for 1 hour. Slides were then washed twice in 1 mM levamisole for five minutes. The colour reaction [1 mL predetection buffer, 14 μL of NBT Stock {0.015g nitroblue tetrazolium (Sigma N6876); 140 μL N, N-dimethyl formamide (Sigma 319937); 60 μL distilled water}, 2 μL BCIP Stock {0.01g bromochloroindoyl phosphate (Sigma B6777); 200 μL N, N-dimethyl formamide}, and 1 μL 1M levamisole] mixture was then applied to slides which were incubated in the dark inside a humidity chamber for 1.5 hours. Following the colour reaction slides were rinsed in running tap water for five

minutes, dried and coverslipped using Gel Mount. After drying overnight, slides were sealed using clear nail varnish and stored in the dark at 4°C.

2.13 Whole-Mount Bone Staining Procedure

Bone staining was carried out in order to visualize the mineralized bones of control and experimental specimens. Prior to staining all specimens stored in 70% EtOH were re-hydrated to distilled water. Specimens were also descaled and degutted. Next, specimens were placed in a 3% hydrogen peroxide (drugstore brand) made in 1% potassium hydroxide (Sigma 1767) bleaching solution overnight to remove all pigmentation. Following bleaching, specimens were transferred to a saturated sodium tetraborate decahydrate (Sigma B9876) solution for eight hours at room temperature. Specimens were then stained in a 1 mg/ml Alizarin Red S (Sigma A5533) staining solution made in 1% potassium hydroxide solution overnight. After staining, specimens were rinsed in 1% potassium hydroxide (Sigma 1767) and transferred to a 1% trypsin (Fischer Scientific 9002-07-7)/2% sodium tetraborate decahydrate (Sigma B9876) tissue digestion solution for three days at room temperature or until all tissues had digested and the specimens had cleared. Once all tissues were digested specimens were placed through a graded glycerol series (20%, 60%) made in 1% potassium hydroxide (Sigma 1767) to storage in 100% glycerol.

Additionally, mature (3 year old) adult specimens were double stained for bone and cartilage using an acid-free Alizarin Red S and Alcian Blue double staining procedure (Appendix 2).

2.14 Analyzing Bone Stained and AP Stained Growth Series Specimens

Once all growth series specimens were stained, infraorbital bones were analyzed both *in situ* and following dissection using a Nikon SMZ1500 stereomicroscope and Nikon 50i eclipse compound microscope. Infraorbitals were photographed using a Nikon DXM 1200C camera.

2.15 Analyzing Bone Stained Condensation Ablation Specimens

Once all condensation ablation specimens were bone stained, infraorbital bones (including ablation, control-side and control IOs) were analyzed both in situ and following dissection using a Nikon SMZ1500 stereomicroscope. Infraorbitals were photographed using a Nikon DXM 1200C camera. Dissected infraorbital bones were photographed individually at high magnification for future shape analysis.

Once dissected infraorbital bones were photographed, they were prepared for shape analysis using the suite of SHAPE software (Iwata and Ukai, 2002; http://lbm.ab.a.u-tokyo.ac.jp/~iwata/shape/). Photographs of dissected infraorbitals were inserted into Microsoft PowerPoint 2010 and outlined using the trace function. Outlines were saved in full colour to a BitMap file. The digital outlines were then uploaded to the program ChainCoder where the contours of the outlines were extracted and stored as chain code (Freeman 1975). The chain codes were then normalized into elliptical Fourier descriptors (EFDs) in the program Chc2Nef. Next, the program PrinComp performed principal component analysis on the EFDs. Finally, shape change accounted for by each resulting principal component was visualized using the program PrinPrint, this procedure was based on that of Iwata et al., (2004).

2.16 Analyzing Bone Stained Neuromast Ablation Specimens

Following bone staining, the right lateral side of all neuromast ablation and control specimens were photographed using a Nikon SMZ1500 stereomicroscope and a Nikon DXM 1200C camera. Care was taken to ensure all specimens were oriented the same way for photographs as they would be used for future geometric landmark morphometric analyses (which require consistency in specimen orientation).

2.17 Canal Wall Analysis of Neuromast Ablation Specimens

In order to evaluate the amount of infraorbital canal wall mineralization, the length of raised canal walls on bone stained neuromast ablation specimens was measured on high magnification photographs using NIS Imaging software. Four measurements were taken during this procedure. The total length of the IO bone where the canal wall will form and the length of the portion of the canal wall that had begun extending outwards (approx. perpendicular to the IO bone) (Figure 5) were measured for both canal walls on individual IO bones. These two measurements were taken for both canal walls for IO3 through IO5. From these measurements a ratio was calculated using the following formula:

$$\frac{\text{Length of Anterior Canal Wall Raised} + \text{Length of Posterior Canal Wall Raised}}{\text{Length of Anterior Presumptive Canal} + \text{Length of Posterior Presumptive Canal}}$$

This ratio was calculated for each treatment and control group. The amount of canal wall mineralization for each IO3-IO5 bone was compared individually between ablation and control groups using an independent samples t-test in SPSS (IBM SPSS Statistics Version 19).
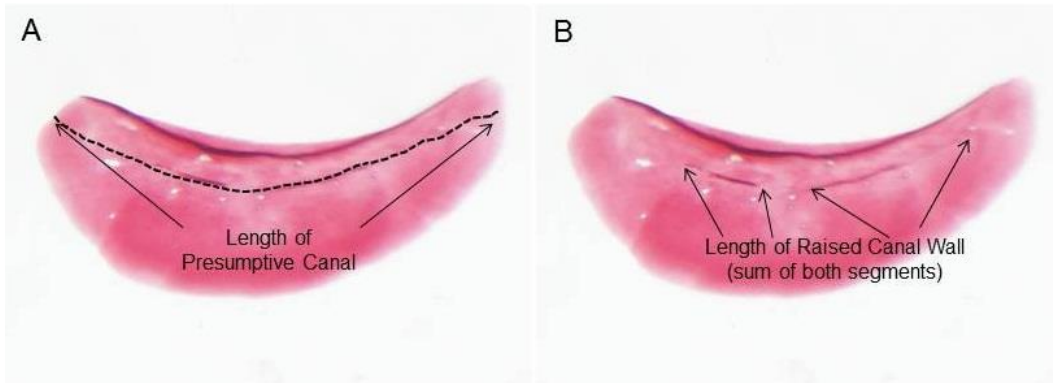
Figure 5. Schematic showing the measurements for one canal side used in calculating the ratio used to compare canal wall mineralization in bone stained neuromast ablation specimens. (A) The presumptive canal wall length (dashed line) of IO3 and (B) the raised canal length (sum of both segments shown with arrows)

2.18   Morphometric Analysis of Neuromast Ablation Specimens

Two different analysis methods were used to determine the affect of neuromast ablation on IO bone shape. First a geometric landmark morphometric analysis was done. This analysis involved the plotting of landmarks on the lateral view of the IO series. The landmarks of ablation specimens and control specimens were compared to determine if there were differences between the IO series of each of these groups. An analysis of biological shape was also performed where the contour of each IO bone was outlined and contour shape was compared between ablation and control specimens to determine if there were IO shape differences between groups.

Geometric landmark morphometric analysis

In order to compare the shape of the IO series in neuromast ablation specimens to controls, individual analyses were conducted for each neuromast ablation treatment group compared to control specimens using geometric morphometric analysis. These analyses involved the application of 20 landmarks (Figure 6) on scaled photographs of the lateral view of right side of ablation and control specimens' skulls. Landmarks (Table 4) were chosen based on their easily identifiable anatomical positions. Photographs were first digitized in tpsUtil and the 20 landmarks (Figure 6) were applied in tpsDig2 software (F. James Rohlf, http://life.bio.sunysb.edu/morph/) and analyses were conducted using the IMP series of software (H. David Sheets, http://www3.canisius.edu/~sheets /morphsoft.html, version 6). Procrustes superimposition in CoordGen7a was used to align corresponding landmarks in order to analyze the changes in shape, and the procrustes distance was calculated. TwoGroup was used to calculate the average Procrustes distance for each treatment and control group. The average distances were then compared individually to that of the control group using Goodall's F-Test and Resampled F-Test.

Following, vector analyses were then conducted in tpsSuper software (F. James Rohlf, http://life.bio.sunysb.edu/morph/), which created a consensus of the landmark for each of the treatment groups and control group. Next each treatment group was individually compared to the control group using tpsSplin (F. James Rohlf) where output vectors show the magnitude and direction of each treatment landmark compared to control landmarks.
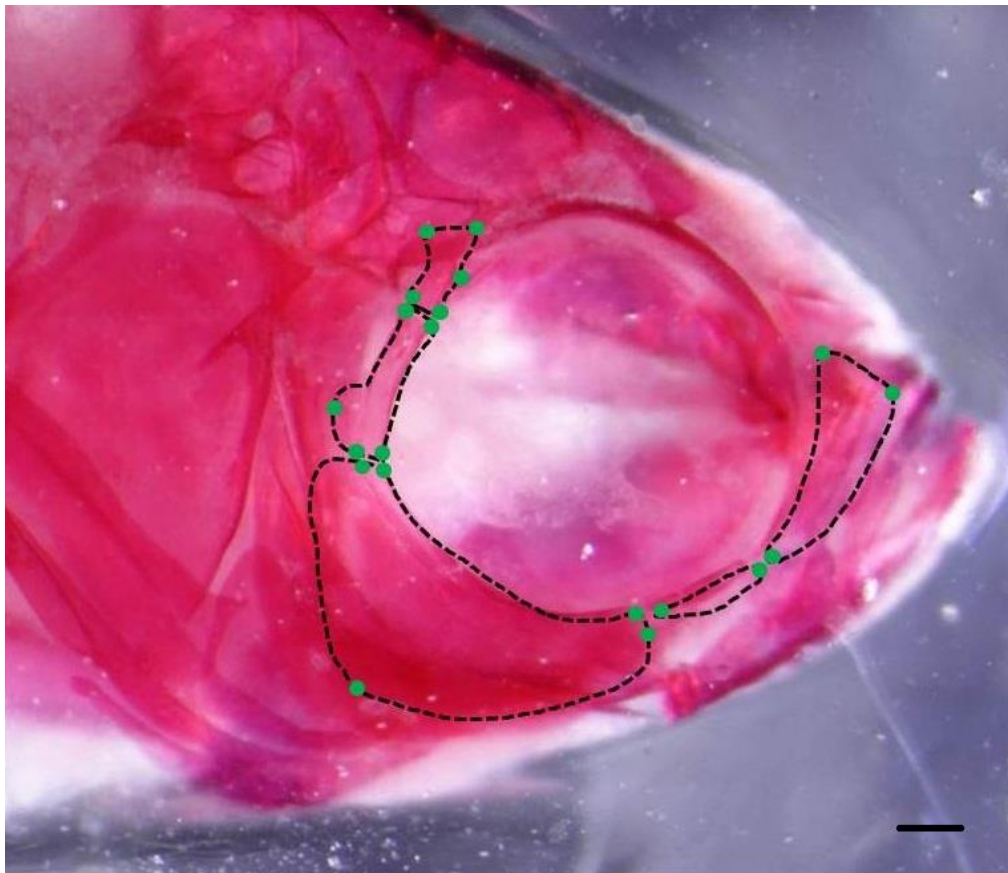
Figure 6. Landmarks applied to the right lateral view of the IO series for morphometric analyses. Scale is 100 μm.

Table 4. List of 20 landmarks used for geometric morphometric analyses.

Landmark Number	IO Bone	Description of Location
1	IO1	Most dorso-posterior edge of IO1
2	IO1	Most dorso-anterior edge of IO1
3	IO1	Most ventral point of IO1
4	IO2	Most anterior point of IO2
5	IO2	Most posterior point of IO2
6	IO3	Most dorso-anterior point of IO3
7	IO3	Most ventral-anterior point of IO3
8	IO3	Most ventral point of IO3
9	IO3	Most ventral-posterior point of IO3
10	IO3	Most dorso-posterior point of IO3
11	IO4	Most ventral-anterior point of IO4
12	IO4	Most ventral-posterior point of IO4
13	IO4	Most posterior point of IO4
14	IO4	Most dorsal-posterior point of IO4
15	IO4	Most dorsal-anterior point of IO4
16	IO5	Most ventral-posterior point of IO5
17	IO5	Most ventral-anterior point of IO5
18	IO5	Most anterior point of IO5
19	IO5	Most dorsal-anterior point of IO5
20	IO5	Most dorsal-posterior point of IO5

Shape contour morphometric analysis

For an alternative analysis of IO shape following neuromast ablation, outline analyses of IO shape were performed to compare neuromast ablation IO bones to control IO bones. High magnification photographs of infraorbital bones were prepared and analysed using the suite of SHAPE software (Iwata and Ukai, 2002; http://lbm.ab.a.u-tokyo.ac.jp/~iwata/shape/) as described earlier (section 2.15)

For analyses of larval neuromast ablation specimens, IO3-IO5 were individually compared to that of control specimens. Analyses of juvenile ablation specimens involved the comparison of IO3 and IO5 outlines for neuromast ablation specimens, to that of controls. Shape analyses were completed as previously described in section 2.15.

3.0 Results

3.1 Description of Infraorbital Bone Mineralization and Osteoblast Activity

3.1.1 Results of whole-mount bone stained growth series

A whole-mount bone stained growth series was prepared in order to describe the mineralization process involved in infraorbital growth. A description of each infraorbital bone's growth is provided from the first signs of mineralization until adulthood.

Infraorbital One

Mineralization of infraorbital one (IO1) first appears in specimens 10.0-11.0 mm SL. Initially, IO1 was shaped as a small sliver of bone along the posterior side of the lateral line canal and extended around a central foramen (Figure 7C-E). The amount of mineralization expanded with further growth and extended towards the borders of the IO1 bone. The dorsal half of IO1 mineralizes before the ventral half (Figure 7F-G). The walls of the lateral line canal begin to mineralize starting at 15.0 mm SL, as the posterior wall of the canal extends outwards (laterally). As the posterior canal wall extends outwards it closes over the roof of the canal extending towards the anterior side of the canal (Figure 7H indicated by asterisk). The closure of the lateral line canal continues throughout further IO1 mineralization; the canal roof closes in the central region of the canal first.

Infraorbital Two

Infraorbital two (IO2) begins mineralization at 16.5-18.0 mm SL starting at either one or two ossification centers in the ventral part of the element(s) (Figure 8A-C). When two ossification centers develop (N=2/5), they fuse later.

The position of the single ossification center is always present midway between the two centers (when present). By 20.0 mm SL, the lateral line canal walls of IO2 begin to mineralize outwards (laterally). The ventral canal wall mineralizes more that the dorsal wall (Figure 8F-I). Also, at 20.0 mm SL both the flat wing-like extension of IO2 as well as the canal portion are present (Figure 8I).

Infraorbital Three

Mineralization of infraorbital three (IO3) first begins in the canal portion of the element, later expanding into the flat wing-like extension. First appearing at 10.0 mm SL mineralization begins in the central portion of the lateral line canal of IO3 (Figure 9A and B). This mineralization expands along the length of the canal before extending into the flat, wing-like portion of the element at 11.0 mm SL. During this increase in mineralization the size of the element increases dramatically. Canal wall mineralization begins at 12.5 mm SL as wall segments extend outwards prior to fusing with adjacent segments (Figure 9F-L). Around 16.0 mm SL, the dorsal canal wall starts to close over the roof of the canal towards the ventral canal wall (Figure 9M).

Infraorbital Four

Infraorbital four (IO4) begins to mineralize at 14.5 − 16.0 mm SL. Starting at the base of a canal-shaped element, this mineralization expands along the length of the element (Figure 10A-C). Canal wall mineralization begins as wall segments mineralize outwards (laterally) at 16.5 mm SL (Figure 10J and K). These segments eventually expand and fuse together to form a wall structure. The flat, wing-like extension of IO4 begins to mineralize as early as 16.0 mm SL. At 18.0 mm SL, the canal walls begin to approach each other over the roof of the canal.

Infraorbital Five

Beginning at a single ossification center, the mineralization of infraorbital five (IO5) starts around a central canal foramen at 13.0 mm SL (Figure 11A-E). This mineralization expands along the entire presumptive canal length at 14.0 mm SL. Appearing at 17.0 mm SL; the flat, wing-like extension of IO5 begins to mineralize (Figure 11J and K). Canal walls become apparent as they mineralize outwards (laterally) at 22.0 mm SL in adjacent segments (Figure 11O). The mineralization of the anterior canal wall precedes that of the posterior wall.

Infraorbital Bones in Three Year Old Fish

In order to determine when canal roof closure occurs, I investigated older, three year old specimens (N=5). Zebrafish are considered to be adults at sexual maturity around 3 months post-fertilization (approximately 20.0 mm SL) and live to 3-5 years old (Parichy et al., 2009). Since complete canal mineralization was not observed in young adult specimens (3-12 months), three year old fish were also fixed, bone stained and analysed. Bone staining reveals that the IO1 canal roof is not completely closed even at 3 years of age; canal walls have not met one another at the ends of the canal (closure is observed in the center of the canal roof only) (Figure 12A and B). No canal closure is seen with bone staining for IO2-IO5, as the canal walls in all of these elements are raised but have not begun closing over to form a complete roof (Figure 12C-J).

To further investigate the canal roof development in aged specimens, whole-mount double stained (Appendix 2 for procedure) specimens (3 year old specimens, N=5) from an ongoing aging project in the lab were inspected for canal roof development. Alizarin Red staining (for mineralization) in these

specimens is consistent with previous observations. Additionally, Alcian Blue staining, which is generally used to detect cartilage, stains structures rich in mucopolysaccharides and is observed lining the canal roofs (Figure 9K).
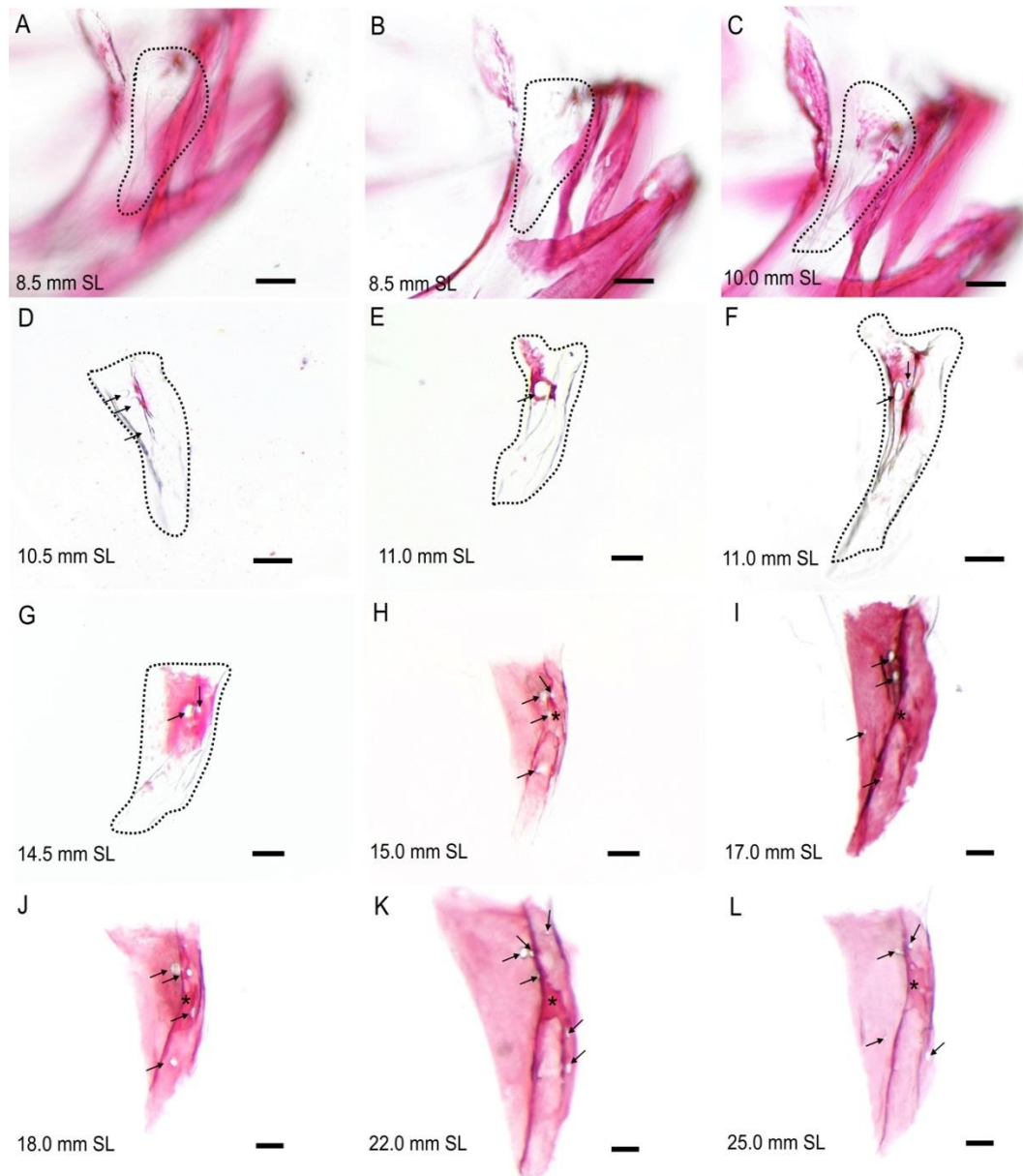
Figure 7. The development of infraorbital one (IO1). (A-C) undissected, (D-L) dissected. The presumptive IO1 bone is present prior to mineralization beginning at 8.5 mm SL but does not stain at this age (A). Mineralization begins at 10.0 mm SL (C) and continues in specimens up to 25.0 mm SL (L). Mineralization occurs around the foramen (arrows) and around canal walls (D-F). The bony lateral line canal roof (*) begins closing at 15.0 mm SL. Anterior direction is to the right and posterior is to the left in all images. Scale bars are 100 μm.
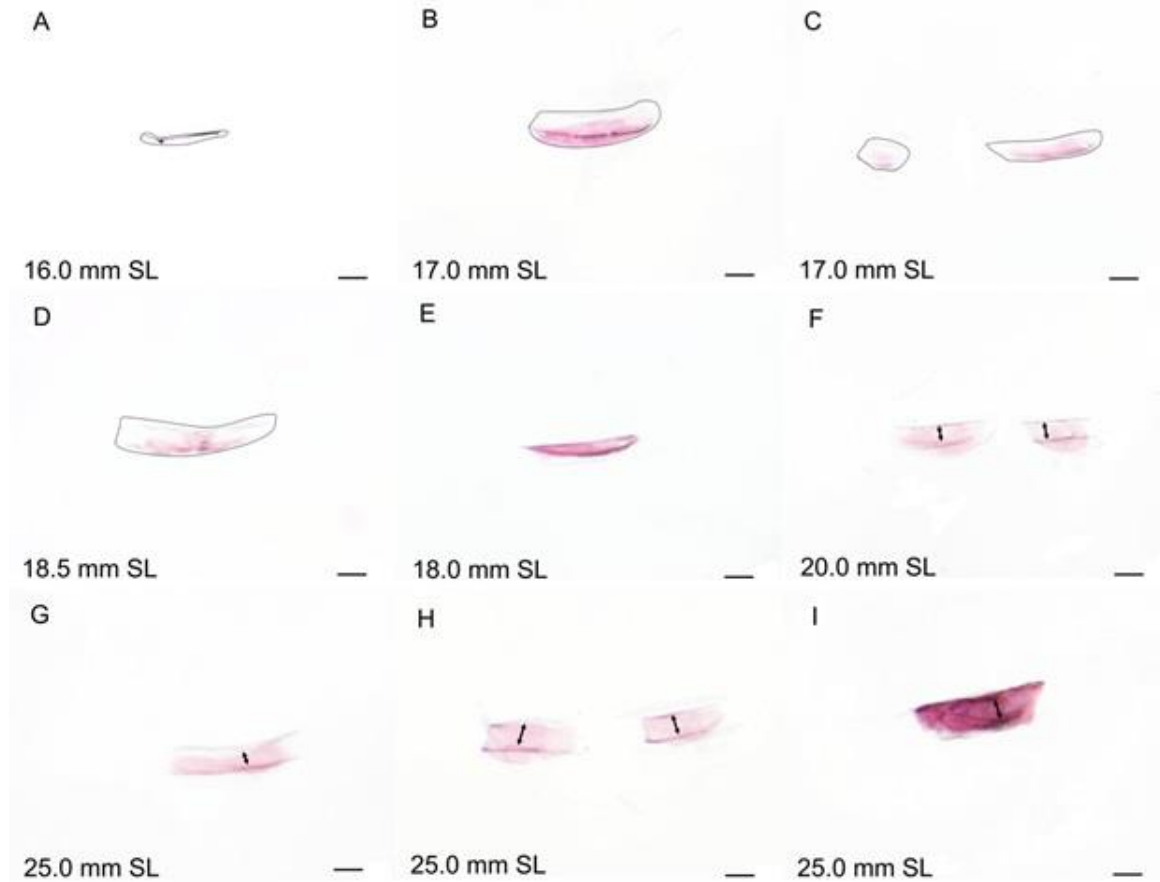
Figure 8. The development of infraorbital two (IO2). IO2 mineralizes late in zebrafish development. IO2 is first noticeable at 16.0 mm SL (A) as a line of tissue that extends from IO1 to IO3. By 17.0 mm SL IO2 appears as one or more slivers of bone (B and C). These slivers of bone eventually ossify into short roof-less canals that expand and, in the case of multiple slivers, join together to form one canal. The point in time when fusion occurs varies. Canal walls begin to mineralize at 20.0 mm SL (F). IO2 is outlined in A-D for clarity. (I) is from a 3 year old specimen. Anterior direction is to the right and posterior is to the left in all images. Arrows indicate canal walls. Scale bars are 100 μm.
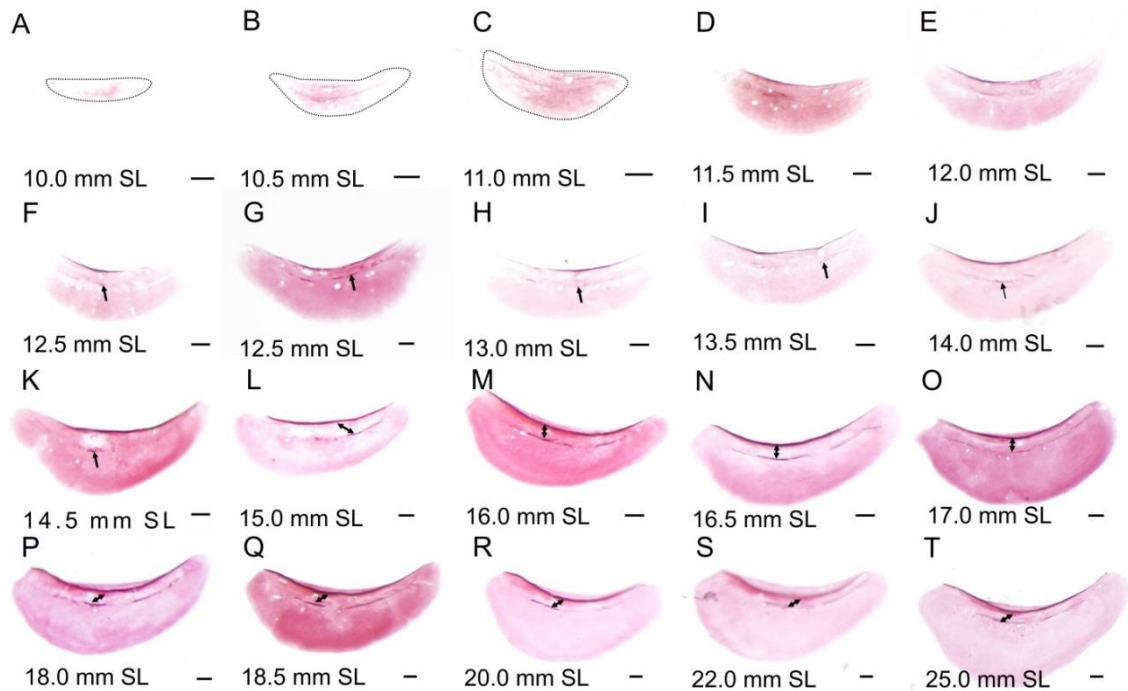
Figure 9. The development of infraorbital three (IO3). IO3 is shown dissected out of the skull (A-T). Mineralization begins at 10.0 mm SL (A) near the center of the presumptive bone (A and B), and continues throughout IO3 development (C-T). The size of the developing IO3 bone increases dramatically during this process. At the same time the lateral line canal walls (double arrows) begin to ossify, appearing at first as segments (arrows) (F-K). Later in development, parallel canal wall segments begin to join and fuse as they continue to ossify outwards (laterally) to form tall canal walls (L-T). By 16.0 mm SL (M), the dorsal canal wall begins to ossify bending over the roof. Mineralization of IO3 continues to adulthood (N-T). Anterior direction is to the right and posterior is to the left in all images. Arrows indicate canal walls. Scale bars are 100 μm.
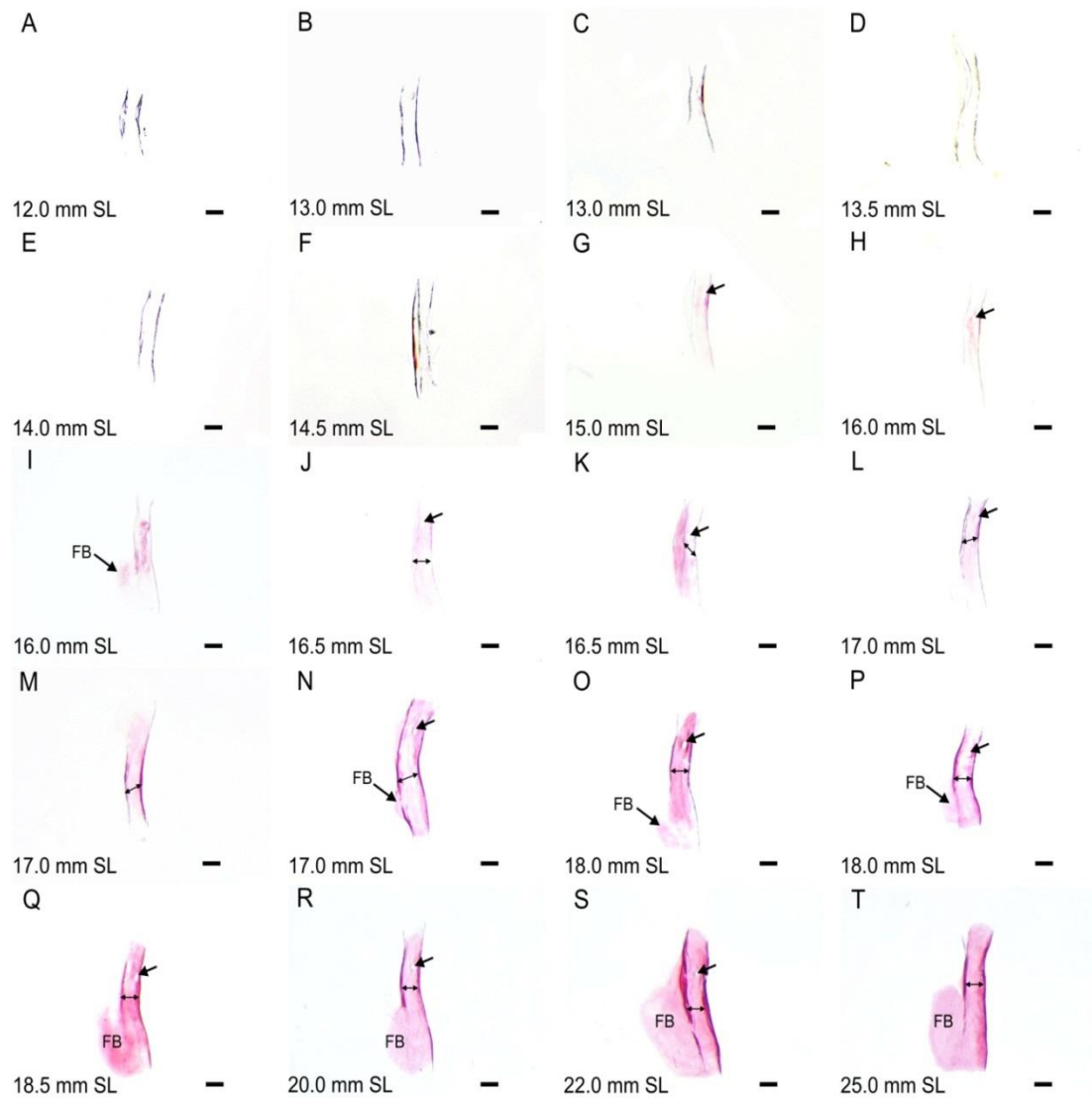
Figure 10. The development of infraorbital four (IO4). IO4 dissected (A-T). Appearing at 12.0 mm SL (A), the presumptive IO4 is canal shaped with no roof enclosure (A-E). At 14.5 mm SL (F) mineralization begins along the base of the canal (G-L). At 16.0 mm SL (I) the canal walls (double arrows) begin to form, mineralizing laterally (outwards). An extension of the flat (FB) portion of IO4 extends out from the posteroventral end of bone (I-T). At 20.0 mm SL (S) the canal roof begins to mineralize. The canal roof closure is not complete by 25.0 mm SL (T). Anterior direction is to the right and posterior is to the left in all images. Single arrows indicate canal foramen. Scale bars are 100 μm.
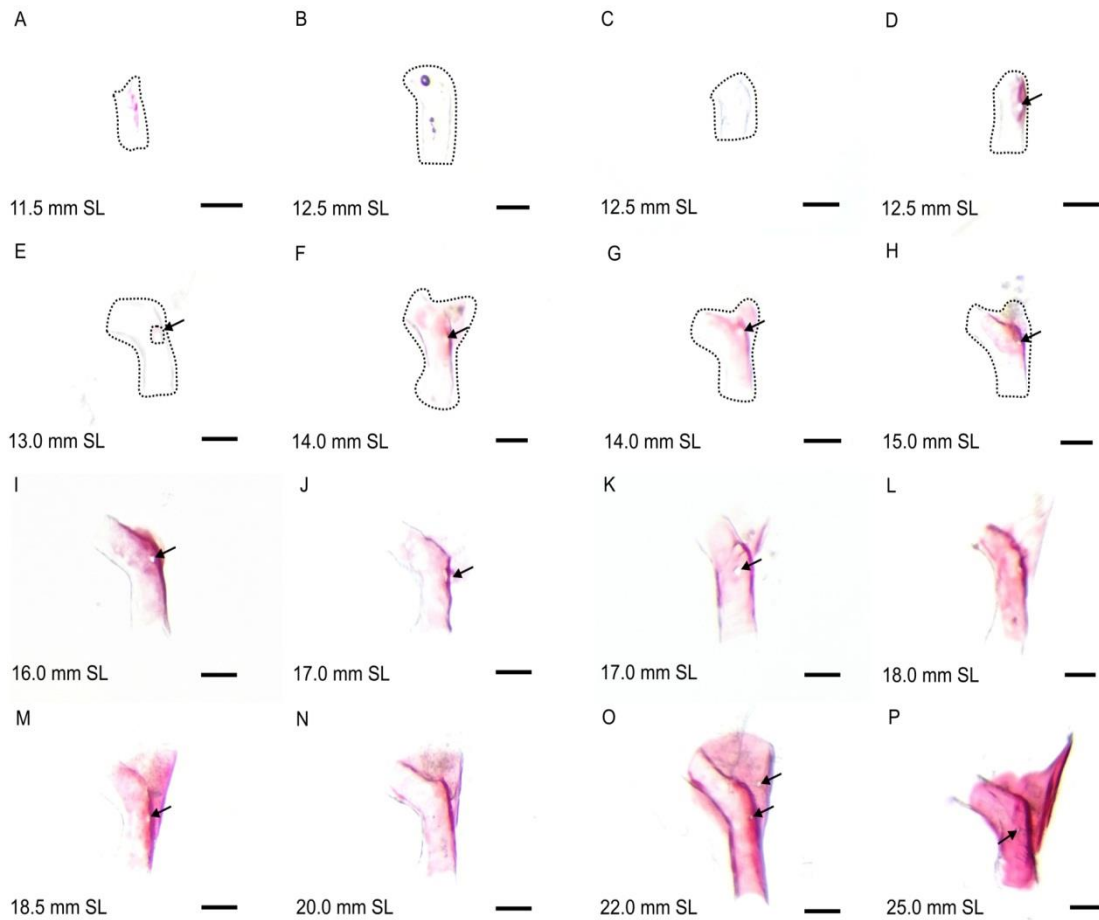
Figure 11. The development of infraorbital five (IO5). IO5 dissected (A-P). Forming as an open, roof-less canal with a bent shape, the presumptive IO5 appears between 11.0 and 12.5 mm SL (A-C). A single foramen (arrows) is present, and mineralization begins around the circumference of this foramen (D-F). Mineralization expands from the initial foramen area (D-E), and also continues as a flat extension from the anterodorsal corner of IO5 at 14.0 mm SL (F-I). By 17.0 mm SL (J) the canal walls begin mineralization. Mineralization continues in the canal walls and flat extension (K-P). At 25.0 mm SL (P) the canal roof of IO5 is not yet closed. Anterior direction is to the right and posterior is to the left in all images. Scale bars are 100 μm.
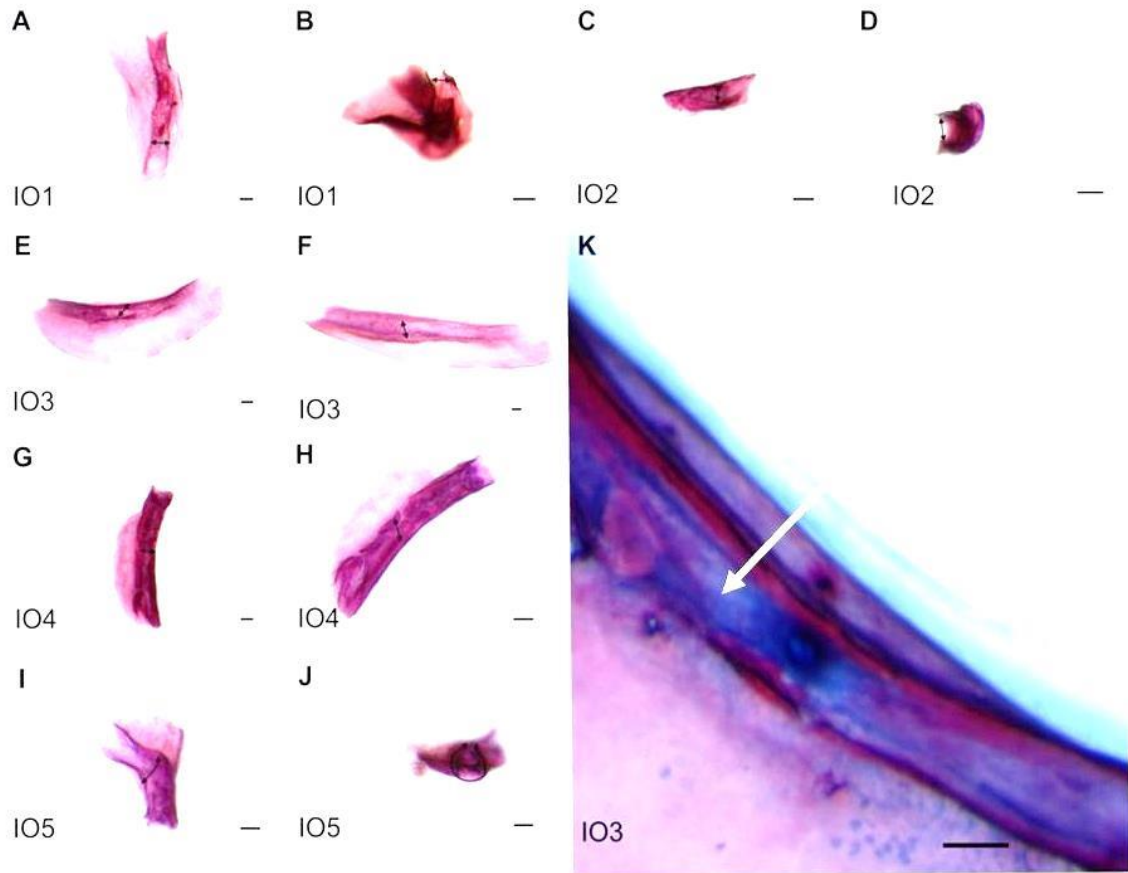
Figure 12. The infraorbital bones in a mature, three year-old zebrafish. (A-B), IO1, (C, D) IO2; (E-F, K) IO3, (G-H), IO4, (I-J) IO5. The infraorbital bones from a mature zebrafish were bone stained (A-J) or double stained for cartilage and bone (K) and dissected. All bones show raised lateral line canal walls and lack complete canal roof mineralization (double arrows). The composition of the unmineralized canal roof can be visualized via Alcian Blue staining (arrow) (K). Anterior direction is to the right and posterior is to the left in all images. Scale bars are 100 μm.

3.1.2 Whole-mount alkaline phosphatase growth series

Osteoblast activity in IO1 is first detected with alkaline phosphatase (AP) staining in specimens 9.0 mm SL (Figure 13A). This osteoblast activity is first apparent in the flat portion of the element and later (at >15 mm SL) is present in the lateral line canal portion (Figure 13B and C). Osteoblast activity persists in the element throughout IO1 growth and AP staining is strong in specimens 17.0 mm SL. From 15.0 – 17.0 mm SL specimen there is osteoblast activity in the canal walls and around canal foramen.

IO2 first shows the presence of active osteoblasts in the canal portion of the element at 15.0 mm SL (Figure 13D). AP staining remains strong in this region and starts to expand into the dorsal flat, wing-like extension in specimens of 16.0 – 17.0 mm SL (Figure 13E and F). There is also osteoblast activity in the canal roof and foramen (Figure 13E and F) at these ages; however intensity is lower than in IO1.

IO3 AP activity is first present in specimens at 11.0 mm SL where osteoblast activity is present in the canal portion of the element (Figure 13G). As the fish grows, AP activity increases in the canal portion and is quite prominent at 15.0 mm SL (Figure 13H). By 17.0 mm SL, active osteoblasts are also in the flat, wing-like extension of the element (Figure 13F). Similar to IO1 and IO2, AP activity is present in the canal roof and foramen.

Osteoblast activity is first visible in the canal of IO4 in specimens of 12.0 mm SL (Figure 13I). By 15.0 mm SL, AP expression has expanded along the length of the canal (Figure 13J), and by around 18.0 mm SL, the osteoblast activity extends into the flat, wing-like extension of IO4 as well as into the canal

roof (Figure 13K). Staining intensity is strong as in IO1 and unlike in IO2 and IO3.

IO5 shows the first signs of AP activity in the base and walls of its lateral line canal by 12.0 mm SL (Figure 13I). At 15.0 mm SL, osteoblast activity is prominent in canal roof as well as in the flat, wing-like extension of the element (Figure 13L). AP activity is still prominent in canal pores as well as in the flat extension at 17.0 mm SL (Figure 13M).
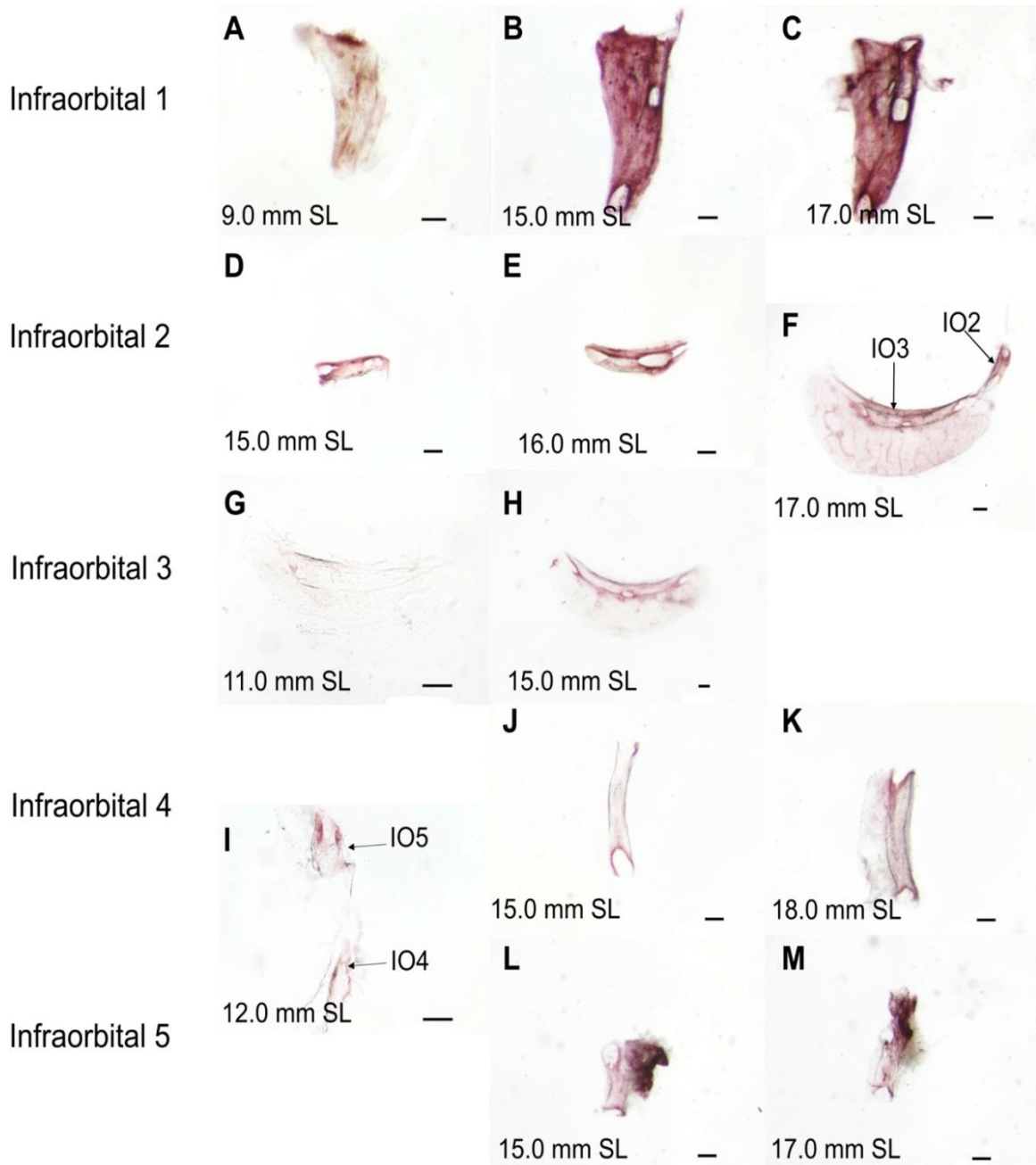
Figure 13. Alkaline phosphatase (AP) staining shows active osteoblasts in the developing zebrafish infraorbital (IO) bones. (A-C) IO1, (D-F) IO2, (F-H) IO3, (I-K) IO4, and (I, L-M) IO5. Anterior direction is to the right and posterior is to the left in all images. Scale bars are 100 μm.

3.2.1 Short-term results of infraorbital five condensation ablation

To investigate the role that an individual infraorbital bone plays in the development of the infraorbital series, a single infraorbital condensation namely IO5, was ablated using the laser ablation method. Immediately following laser ablation, there is no visible sign of the IO5 condensation (n=4) (Figure 14A and B). Similarly, at 24h post-ablation there is still no visible IO5 condensation (Figure 14C); however, by 4 days post-ablation a reformed IO5 condensation is visible (n=4)(Figure 14D). This reformed IO5 condensation is slightly smaller and is closer to the adjacent IO4 condensation when compared to the IO5 condensation on the control side (Figure 14E). The reformed IO5 condensation touches the IO4 condensation. By two weeks post-ablation an obvious size and developmental difference is seen when comparing the recovered IO5 to the control side (compare Figure 14F and 14G). The recovered IO5 (n=3/4) appears smaller in size compared to the control, appearing shorter in length. A developmental difference is also evident with respect to canal wall development; as the recovered IO5 does not have visible canal walls whereas the control side has walls that approach one other (Figure 14F and G). These results indicate that an infraorbital bone can recover from ablation, however the recovered IO5 condensations appear smaller and less developed when compared to the control IO5 condensations.
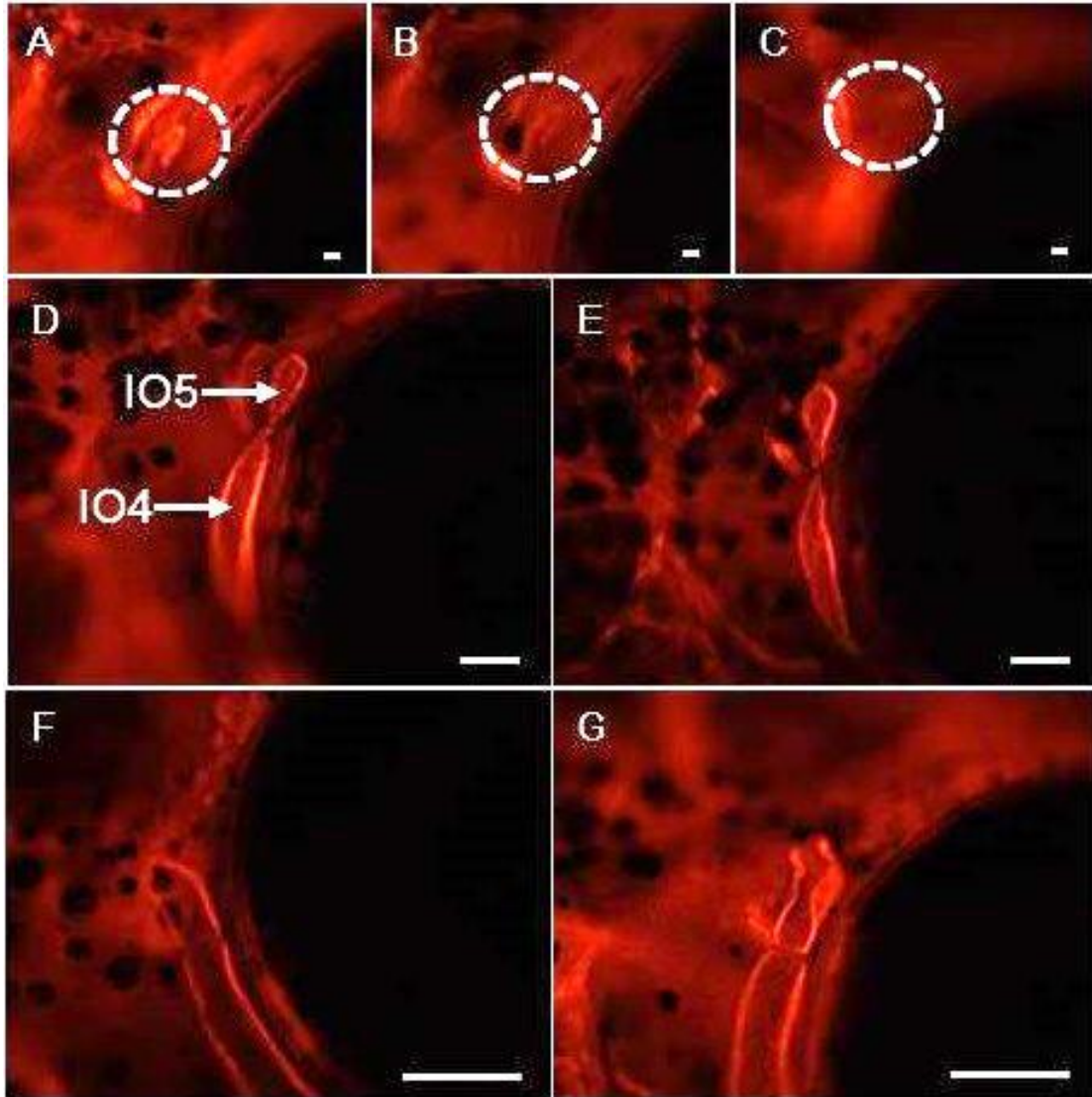
Figure 14. Laser ablation of the right infraorbital five (IO5) condensation in an *osterix*$^{+/+}$ zebrafish. (A) before ablation; (B) immediately after ablation; (C) 24 hours post-ablation, no condensation is visible; (D) by 4 days post-ablation a reformed condensation is observed touching IO4 compared to (E) control-side; (F) the IO5 continues to grow at 2 weeks post-ablation and is still closely associated with IO4; it appears less developed (lacking canal walls) compared to the (G) control side. Anterior is to the right and posterior is to the left such that the eye is located in the bottom right of each image. Scale bars are 50 μm.

3.2.2 Long-term results of infraorbital five condensation ablation

Overall, two months after ablation of the IO5 condensation, the reformed IO5 bone is morphologically different from the control-side of the head (in n=3/4) and is also different to other non-ablation fish (n=4, not shown) (Figure 15). The remaining ablation specimen appeared similar to the control-side specimens. The recovered IO5 differs from the control and control-side IO5 bone in terms of shape, size and developmental stage (Figure 15). In terms of shape, the recovered IO5 bone does not possess the prominent bend in the canal aspect or a flat, wing-like portion of the bone that is characteristic of IO5 morphology (compare Figure 15A,C to 15B, D). Additionally, the recovered IO5 appears truncated as the dorsal-half of the bone has not formed making the recovered element smaller compared to controls. With respect to developmental stage, the lateral line canal walls in ablation specimens are not as developed as they have not approached one another compared to those of control-side elements. Untreated control specimens are not shown.
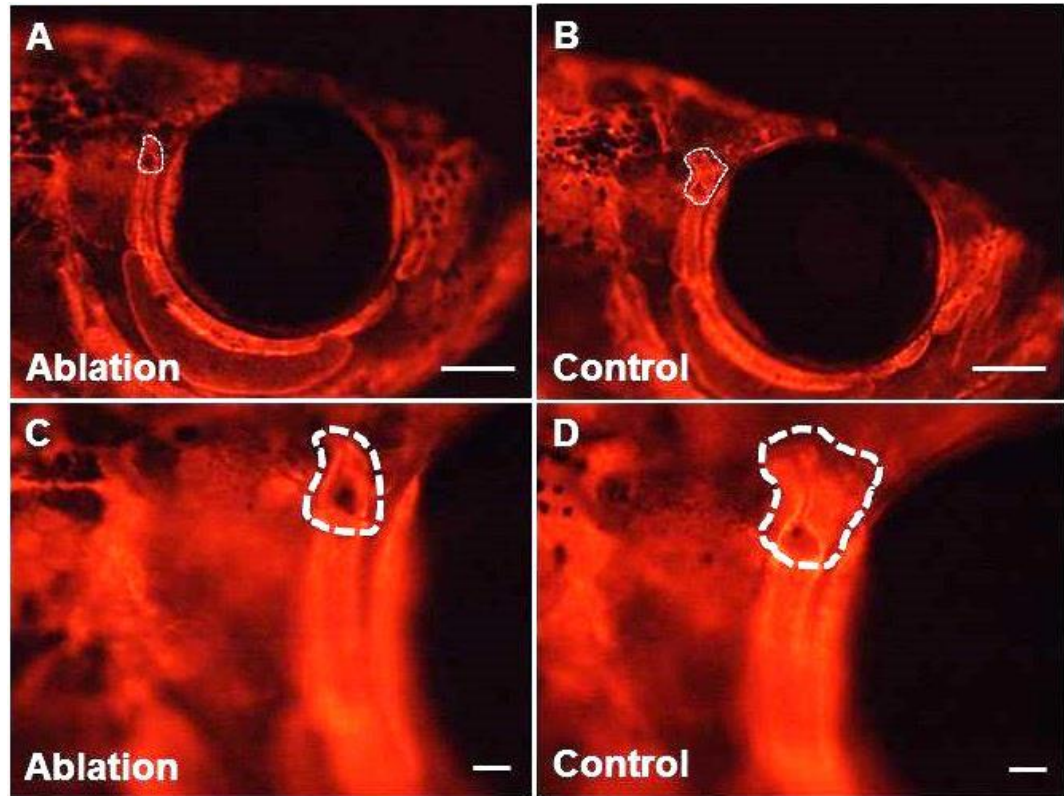
Figure 15. Two months following IO5 condensation ablation developmental and shape differences are seen when comparing ablated (A and C) and control-side (B and D). Recovered IO5 bones appear smaller in size as the dorsal length and wing-extension are not seen and also less developed as canal walls are not as raised. Anterior is to the right and posterior is to the left. Scale bars are 50 μm.

By adulthood (19.0-22.0 mm SL), the recovered IO5 is still visibly different to that of the controls (control-side and control group) in three of the four ablation specimens (Figure 16A-B, D). In the fourth specimen, the IO5 bone is similar in shape and size to the control IO5 elements (Figure 16C). The affected IO5 elements differ from control IO5 elements similarly to previous observations at two months post-ablation; that is, the recovered IO5 element is smaller, dorsally truncated and appears less developed (Figure 16A, B and D). The extent which this recovered IO5 differs from control elements varies between specimens, as there was a range of morphologies observed from an extreme (Figure 16D) to a milder case (Figure 16B).

Since IO5 recovery appears to be close to the adjacent IO4, the adult IO4 structure was also examined in ablation, control-side and control specimens (Figure 17). The IO4 from the right side (ablation-side) of treated specimens appears identical morphologically to the IO4 element from the left side (control-side) of the head (Figure 17 A, B and 16 D, E). When comparing ablation IO4 bones to control specimens (Figure 17C and F), variations in IO4 morphology (element length and the presence or absence of a flat, wing-like extension) are seen in both groups. There is no distinct visible difference in ablation elements compared to control IO4 elements.
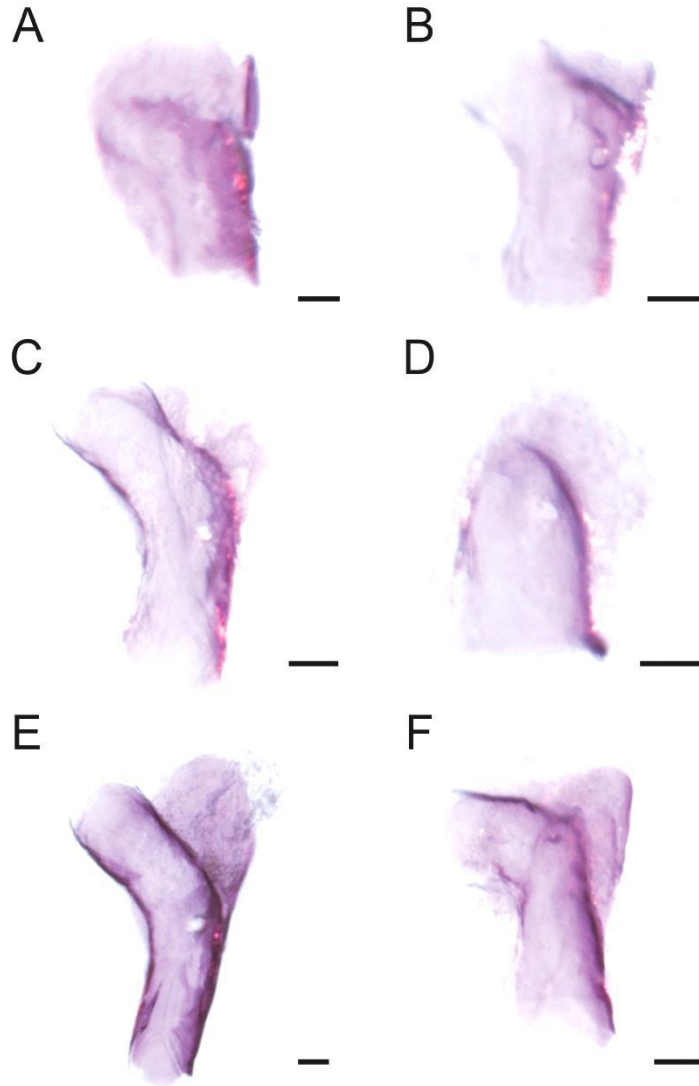
Figure 16. Infraorbital five (IO5) elements from adult ablation and control zebrafish. The IO5 element from condensation ablation specimens (A- D). All (A-B, D) but one (C) IO5 element appears smaller and less developed compared to controls (E and F). (A-D) have reduced or absent flat, wing-like extensions compared to controls (E and F). The forth ablation IO5 element (C) is similar in size and shape to control (E and F). Anterior is to the right and posterior is to the right in all images. Scale bars are 50 μm.
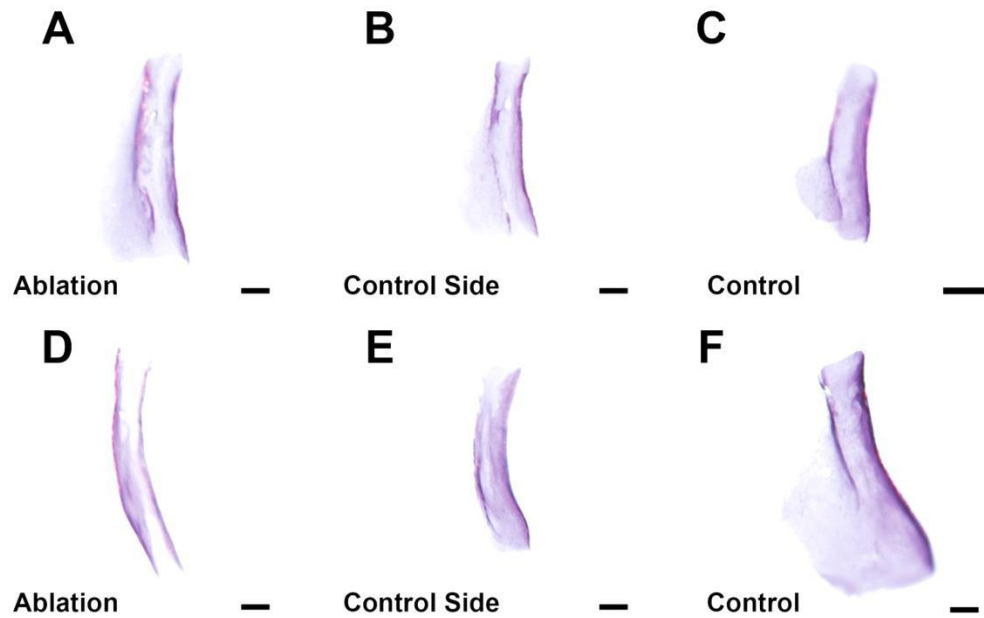
Figure 17. Infraorbital four (IO4) elements from adult (A, D) ablation, (B, E) control-side and (C, F) control zebrafish. The IO4 element from the ablation-side of adult condensation ablation specimens appears similar in shape and size to the IO4 element on the control-side of the specimen (A compared to B, D compared to E). The IO4 elements from control specimens (C and F) appears similar in shape and size to all the ablation specimen IO4 elements. Between all specimens (within groups and between groups) natural variation is seen in IO4 shape with respect to the size of the flat, wing-like extension of the element. Anterior is to the right and posterior is to the left in all images. Scale bars are 100 μm.

3.2.3 Statistical shape analysis

To statistically analyze whether shape differences between ablation and control specimens are present, a morphometric shape analysis was performed in the SHAPE software program (Iwata and Ukai, 2002). This analysis examines contour shape from images, delineates the contour shape with elliptic Fourier descriptors (EFDs) and performs a principal component analysis to summarize shape information (Iwata and Ukai, 2002). The contour of IO5 elements of ablation, control-side and control specimens were compared using this program. Table 5 gives the data for IO5 shape analysis. The cumulative contribution of the first three principal components is for over 70% of the total variance. Following visualization of the principal components in PrinPrint, the morphological meaning associated to each principal component was delineated (Figure 18). The first principal component corresponds to the thickness or width: length proportion of the element and accounts for 37.42% of the total variance. The second principal component corresponds to the size of the flat, wing-like extension of the element and accounts for 21.75% of the variance. Finally, accounting for 14.32% of the variance is the third principal component which describes the bend in the canal portion of the element.

After plotting scatter graphs of the first three principal component scores some grouping of ablation and control specimens were seen with relation to IO5 morphology (Figures 19-21). It is important to note that one of the four ablation elements tended to group with control elements instead of with the remaining ablation elements (red triangle in Figure 19-20). The strongest grouping was observed when PC1 (element width) was plotted against PC2 (wing size) as three

of the four ablation elements grouped close together in a cluster (Figure 19, circled); recall that PC1 and PC2 accounts for 37.42% and 21.75% of the variation, respectively. This cluster was seen in the area that represented wide, wing-less or reduced wing size suggesting that ablated condensations share this morphology and control-side/control elements do not..

No specific grouping was observed along the PC3 (bend) axis as the ablation elements were evenly distributed; half of the ablation elements have a bend in the canal aspect while the other half did not (Figure 20 and 21). The control-side and control IO5 elements were also equally distributed along PC3 (Figure 20). The control-side and control elements did not show distinct groupings and were evenly distributed among one another suggesting that this variation represents the normal variation of this dimension in IO5 elements and is not caused by the ablation experiment.

Table 5. Eigenvalues and proportions of principal components of the infraorbital five (IO5) elliptic Fourier descriptors. A cumulative total of 96% of the variance is accounted for by the first seven principal components.

	PC1	PC2	PC3	PC4	PC5	PC6	PC7
Eigenvalue*	8.56	4.98	3.28	2.83	0.96	0.74	0.51
Proportion (%)	37.42	21.75	14.32	12.37	4.19	3.23	2.23
Cumulative (%)	37.42	59.18	73.50	85.87	90.06	93.30	95.52

*Read eigenvalue as $\chi \times 10^{-3}$

PC1
(Width)

PC2
(Wing Size)

PC3
(Bend)
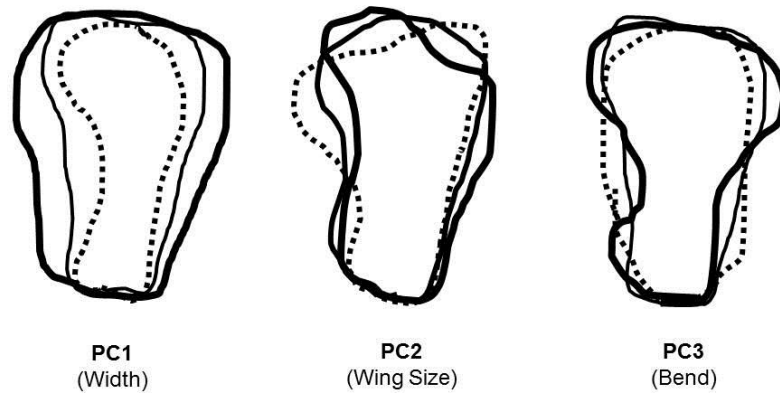
Figure 18. Variations in IO5 shape in adult ablation, control-side and control specimens accounted for by the 1st, 2nd, and 3rd principal components. The contour variance of each principal component is shown: broken line, thin solid line and thick solid line show average -2SD, mean and +2SD respectively. SD, standard deviations from the mean.
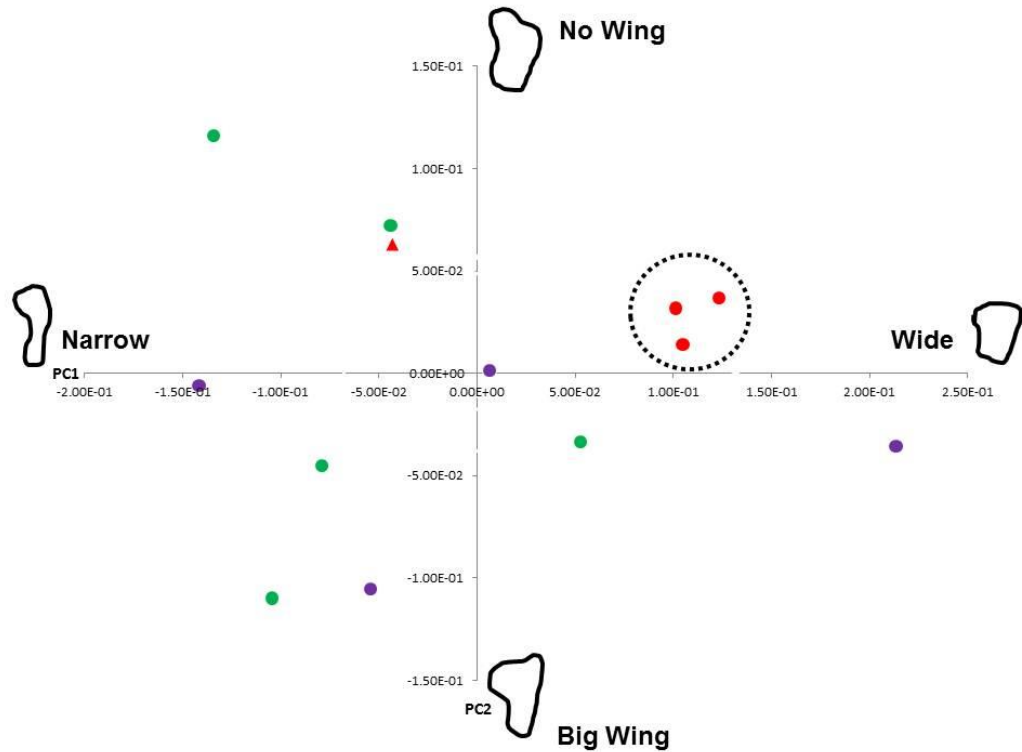
Figure 19. Scatter graphs of scores for ablation experiment IO5 elements on principal components 1 and 2. Ablation, control-side and control infraorbital five (IO5) elements are colour coded red, purple, and green respectively. Reconstructed shapes representing the variance in each principal component are shown at the axes end-points. A distinct grouping of all but one (triangle) of the ablation IO5 elements is shown in the circle.
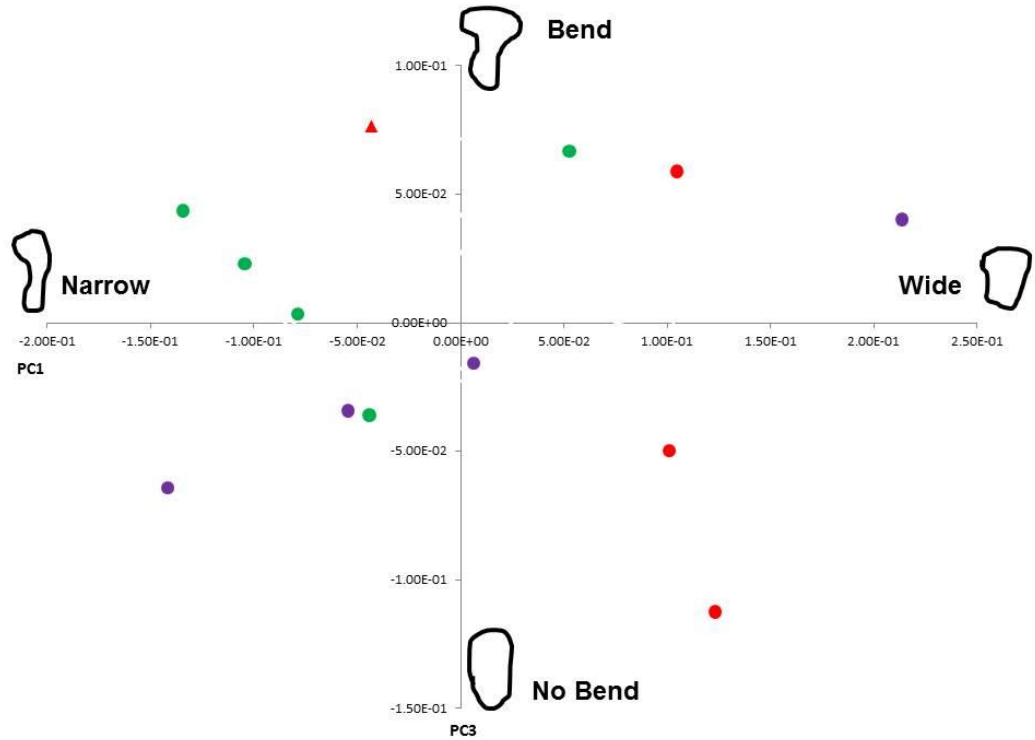
Figure 20. Scatter graphs of scores for ablation experiment IO5 elements on principal components 1 and 3. Ablation, control-side and control infraorbital elements are colour coded red, purple, and green respectively. Reconstructed shapes representing the variance in each principal component are shown at the axes end-points. All but one (triangle) ablation IO5 elements are seen on the positive side of the PC1 axis (wide). No distinct grouping is seen between groups, and the ablation elements are equally distributed on the positive and negative ends of the PC3 axis (bent and un-bent ends).
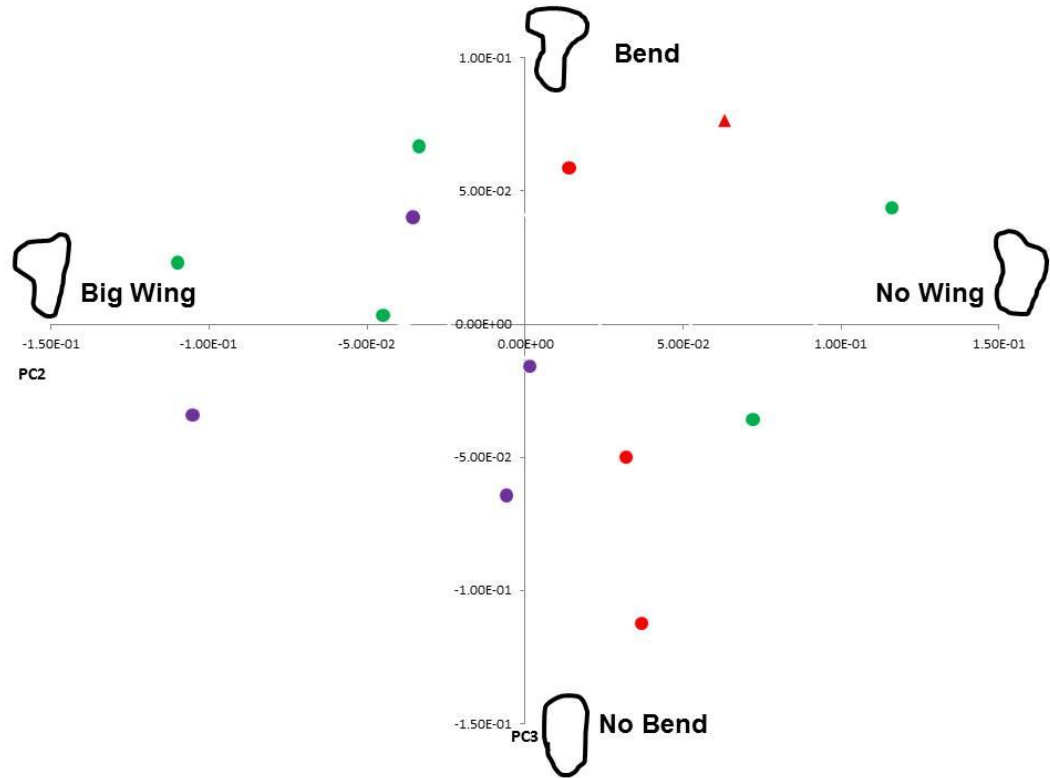
Figure 21. Scatter graphs of scores for ablation experiment IO5 elements on principal components 2 and 3. Ablation, control-side and control infraorbital elements are colour coded red, purple, and green respectively. Reconstructed shapes representing the variance in each principal component are shown at the axes end-points. No distinct grouping is seen between groups, although all ablation specimens are located on the positive side of the x-axis (small wing size). The ablation elements are equally distributed on the positive and negative ends of the y-axis (bent and un-bent ends).

3.3 Neuromast Ablation

In order to determine whether IO canal neuromasts influence the ossification of canal walls, IO neuromasts were ablated at both larval and juvenile time-points. Neuromasts were ablation as described in section 2.10. For all ablations, the FM1-43FX dye allowed for neuromasts to be visualized under FITC fluorescence (Figure 22A) and subsequently ablated (Figure 22B). Follow-up observations were performed by live observations (3.3.1). Long-term analyses were also conducted through a statistical shape analysis (3.3.2).

3.3.1 Short-term results of infraorbital canal neuromast ablation

Each time a neuromast was ablated, the ablation event was visualized as a bubble in the targeted tissue followed by immediate loss of fluorescence. No other visible damage was observed during the ablation.

Following, the IO3 and IO4 neuromast ablation in larval fish, there was no visible sign of the ablated neuromast immediately following ablation (Figure 22B) or signs of regrowth 24 hours post-ablation (Figure 22C) (n=20). At 5 days post-ablation neuromast regrowth was visualized (Figure 22D) as smaller (few cells) compared to before ablation (n=20) (Figure 22). Following, the ablation of IO3 (n=10) or IO5 (n=20) neuromasts in juvenile specimens, there was no recovered neuromast present at 24 hours post-ablation (compare Figure 23A and Figure 23B). At 4 days post-ablation, the recovered neuromast (Figure 23C) was similar in morphology to that of control (untreated) neuromasts (Figure 23D).
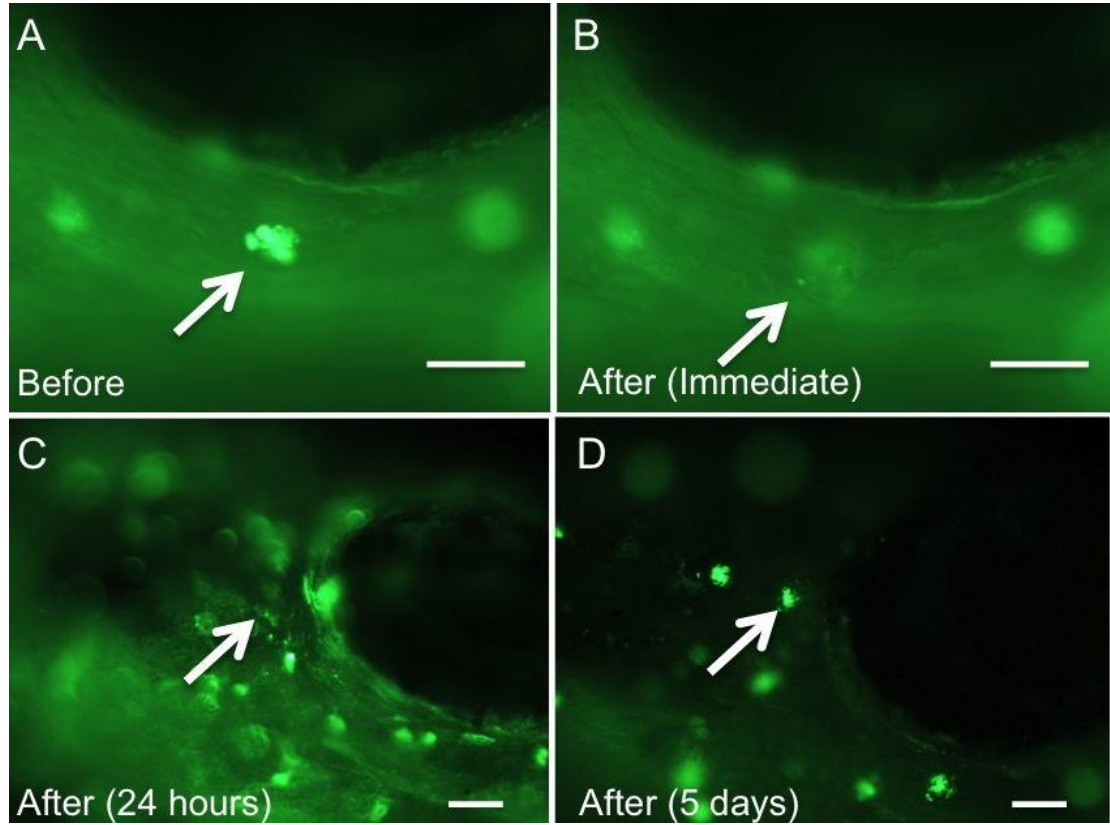
Figure 22. Ablation of IO3 and IO4 neuromasts in larval (5 dpf) zebrafish results in neuromast recovery. (A) Before and (B) immediately after neuromast ablation in larval (5 dpf) zebrafish. (C) At 24 hours post-ablation there is no visible sign of the neuromast. (D) At 5 days post-ablation the recovered neuromast can be observed. Arrows indicate the ablation region. Anterior is to the left and posterior is to the right in all images. Scale bars are 50 μm.
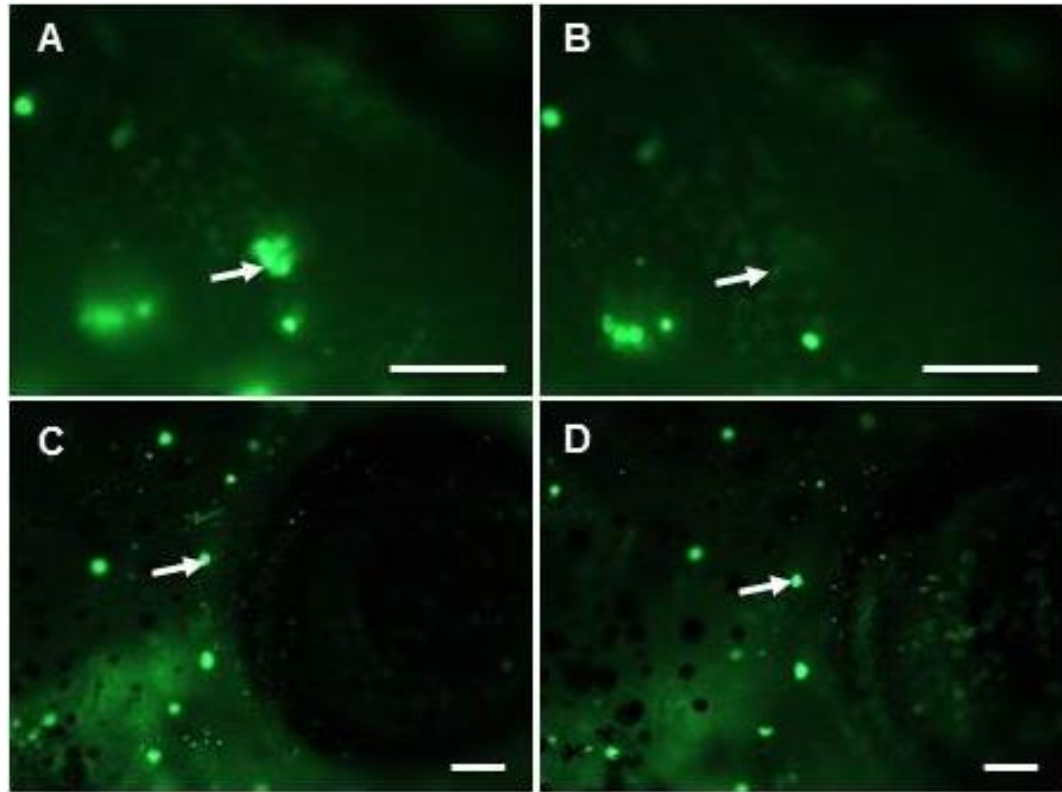
Figure 23. Ablation of neuromast in juvenile (10.0 mm SL) zebrafish results in neuromast recovery. (A) Before and (B) after neuromast ablation. (C) At 4 days post-ablation there is visible sign of a recovered neuromast that appears similar to control specimen IO neuromasts (D). Anterior is to the left and posterior is to the right in all images. Scale bars are 50 μm.

Histological staining was done one hour following ablation to investigate the extent of tissue damage following ablation. TUNEL staining at 3 days post-ablation was done to investigate cell death due to ablation: three days was chosen for this as the process of cell death may not be seen immediately following ablation. Histological sections show that the neuromast is damaged by the ablation but that surrounding tissues are not (compare Figure 24C and D). TUNEL staining, which labels apoptotic cells, was conducted three days post-ablation and show that cell death is observed in cells within the neuromast itself but not in surrounding tissues (Figure 24E); control side were not positive for apoptosis (Figure 24F).
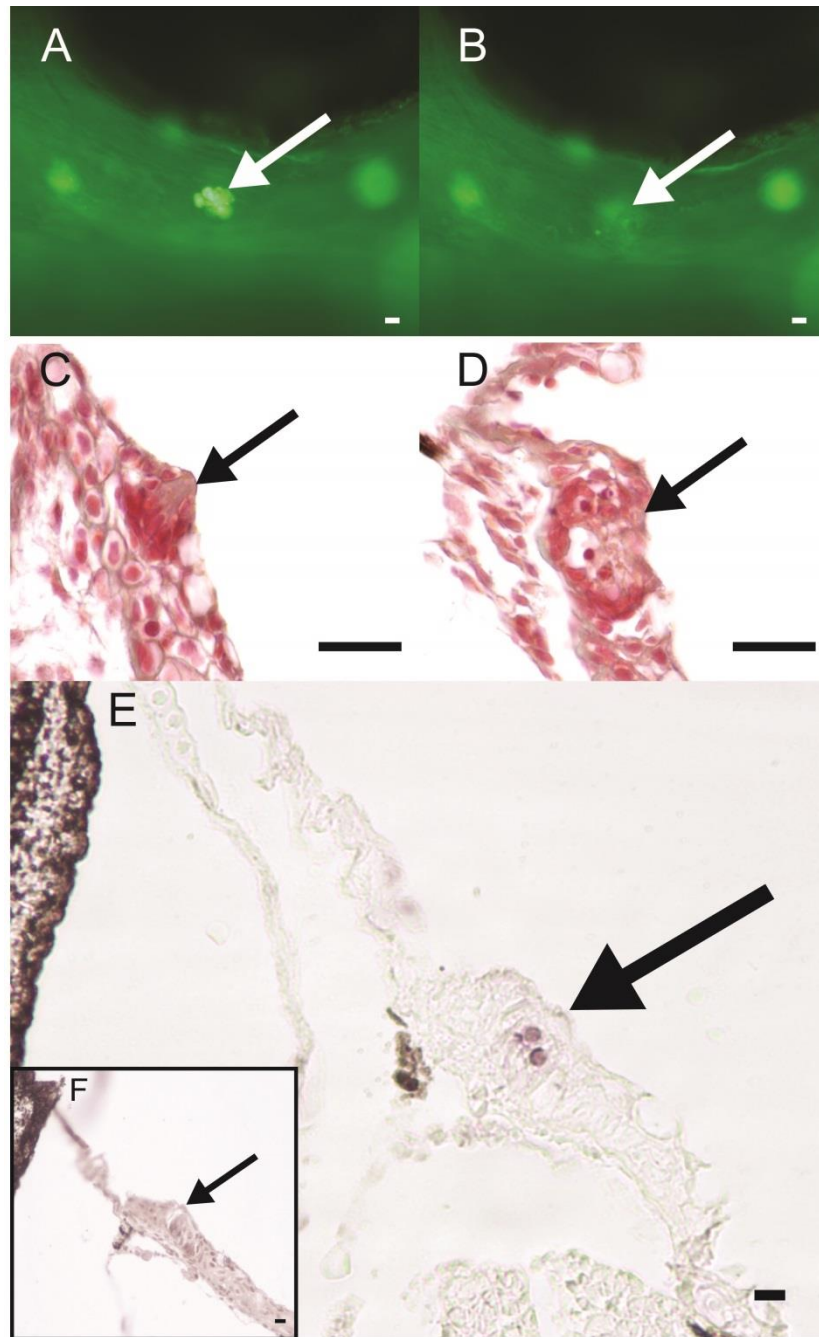
Figure 24. (A) Before and (B) after neuromast laser ablation in live zebrafish specimens stained with FM1-43. One hour post-ablation, Masson's trichrome stained cross-section of (C) control-side and (D) ablated neuromasts. Three days post-ablation, TUNEL stained cross-section of (E)) ablated neuromasts and control side (inset F). Arrow indicated neuromasts. Scale bars are 10 μm.

73

3.3.2 Long-term results of infraorbital canal neuromast ablation

In order to evaluate the effects of earlier neuromast ablations on adult IO bones, the adult (grown-out) neuromast ablation specimens were fixed and bone stained. All of these specimens were measured prior to fixing and their standard lengths were recorded (Appendix 1, Table 3). Since all treatment and control groups contained a minimum of ten specimens that covered a variety of standard lengths, the standard lengths for each group were compared to ensure that groups were not statistically different from one another in terms of size (developmental stage). Control specimens from both larval control and juvenile control groups were pooled. Groups were compared using a one-way ANOVA for standard length in SPSS (IBM SPSS Version 19). Standard lengths of treatment and control groups did not differ significantly [$F(3,54)=0.065$, $p=0.98$].

3.3.2.1 Neuromast ablation and lateral line canal wall closure

In order to determine whether canal neuromasts are involved in the induction of the outgrowth of the bony lateral line canals in infraorbital bones, the proportion of canal wall outgrowth (which is an indicator of canal closure) was measured in ablation and control specimens (Appendix 1, Table 4). An independent t-test was performed to compare the proportion of canal wall present between each treatment group (larval ablation, juvenile IO3 ablation, and juvenile IO5 ablation) and the control group. The proportion of canal wall outgrowth was significantly less in adult specimens that received larval neuromast ablation in the IO3-IO5 bones compared to controls (IO3 bones: $t(23)=0.329$, $p <0.05$; IO4 bones $t(22)=4.19$, $p<0.05$; and IO5 bones $t(21)=4.69$, $p<0.05$). The proportion of canal

wall outgrowth was also significantly less in adult specimens that received the juvenile neuromast ablation of the IO3 bones compared to controls [t(18)=4.215, p<0.05]. However, no significant difference was seen in the amount of canal wall outgrowth in adult specimens that received the juvenile neuromast ablation of the IO5 bones compared to controls. These results suggest there may be some relationship between neuromasts and lateral line canal wall ossification.

3.3.2.2 Morphometric analysis of adult infraorbital bone morphology using geometric landmarks

Initially, 20 geometric landmarks were applied to scaled images of the right lateral side of neuromast ablation and untreated control specimens and morphometric analyses were conducted using TPS and IMP software programs. The results of these analyses did not provide a clear description of what was happening to the shape of elements as a result of ablation. Specifically, the results indicated variation in the infraorbital bone locations due to differences in head shape. For these methods, fixed landmarks are required to be placed in anatomical locations that can repeatedly be found. Since infraorbital bones are curved elements, there was some subjectivity in positioning these fixed locations. For these reasons, this analysis was abandoned after preliminary results (Appendix 3) were obtained. In order to evaluate the shape of the IO bones in adult specimens following neuromast ablation, a different morphometric analyses was conducted. This involved using a SHAPE analysis software program (Iwate and Ukai, 2002) that describes the entire contour of the IO bones and does not require fixed anatomical landmarks.

3.3.2.3 Shape analysis of adult IO bones after larval neuromast ablations

To statistically analyze shape differences of larval IO bones between neuromast ablation and untreated control specimens, a shape analysis was performed in the software program SHAPE. These analyses were performed on IO3, IO4 and IO5 separately.

For IO3 elements, the cumulative contribution of the first three principal components is for over 85% of the total variance (Table 6). Specifically, PC1 accounts for 51% of the variance, PC2 accounts for 27% of the variance and PC3 accounts for 9% of the variance (Table 6). Following visualization of the principal components in PrinPrint, the morphological meaning associated to each principal component was delineated (Figure 25). The first principal component corresponds to the dorsoventral depth of the element. The second principal component corresponds to the taper direction of the element. Finally, the third principal component describes the bend or curvature along the dorsal edge of the element. After plotting scatter graphs of the first three principal component scores, some groupings of ablation and control specimens were seen in relation to morphology (Figures 26-28). The strongest grouping was observed when PC1 was plotted against PC2 as most of the ablation elements grouped close together in a cluster for deep, anteriorly-tapered shape (Figure 26). The ablation elements separated along the PC3 (bend) axis in the remaining plots as half of the ablation elements showed a bend in the canal aspect (Figure 27 and 28).

For IO4, the cumulative contribution of the first three principal components is for 86% of the total variance (Table 7). The morphological meaning associated to each principal component was delineated (Figure 29).

Again, the first principal component corresponds to 51% of the variance; in this element it describes the size of the flat, wing-like extension. The second principal component accounts for 22% of the variance and corresponds to the curvature of the lateral line canal. Finally, the third principal component accounts for 14% of the variance and describes the thickest part of the element; specifically, whether the dorsal half of the element is wider than the ventral aspect (i.e. top heavy vs. bottom heavy). After plotting scatter graphs of the first three principal component scores no distinct grouping was seen in any of the component axes, however, ablation elements displayed a wider distribution along all PC axes compared to control elements (Figures 30-32).

For IO5 elements, the cumulative contribution of the first three principal components is 88% of the total variance (Table 8). The morphological meaning associated to each principal component was delineated as before (Figure 33). The first principal component corresponds to the size of the flat, wing-like extension and describes 63% of the variance. The second principal component corresponds to the thickness or width of the element and describes 18% of the variance. Finally, the third principal component describes the size of the canal bend of the element but only describes 6% of the observed variance. After plotting scatter graphs of the first three principal component scores no distinct groupings were seen along any of the component axes (Figures 34-36).

Altogether, the results of the shape analysis of adult IO3-IO5 elements after larval neuromast ablation, show that the first three principal components account for over 85% of the variance in all three elements and that the first principal component accounts for at least 50% of the variance in each bone. Since

IO3-IO5 each have their own unique morphology PC1 does not represent the same variation in each bone, however PC1 always describes outgrowth of the flat, wing-like aspect of each bone. Specific grouping of ablation and control specimens was only observed in IO3 elements where the elements group along first and second principal component axes: ablation elements tended to be anteriorly tapered and deep along the dorsoventral length, whereas control elements were shallow along the dorsal ventral length and also posteriorly tapered. For IO4 and IO5 elements, no specific grouping was observed, however the ablation specimens displayed a greater variety of shapes compared to control elements.

PC1
(Dorsoventral Depth)

PC2
(Taper Direction)

PC3
(Dorsal Edge Curvature)
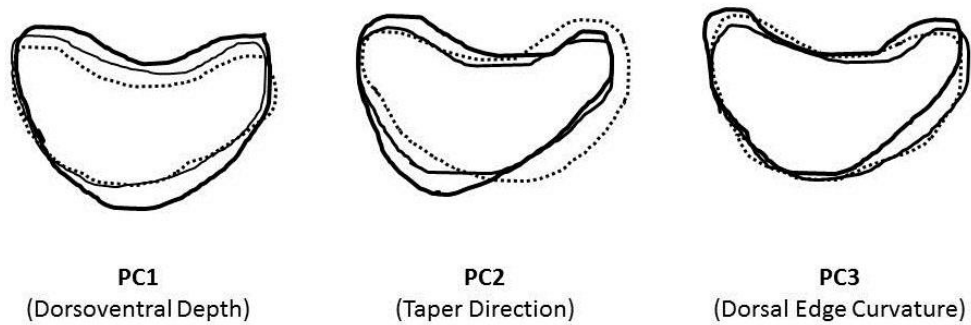
Figure 25. Variations in infraorbital three shape accounted for by the 1st, 2nd, and 3rd principal components following larval neuromast ablation. The contour variance of each principal component is shown: broken line, thin solid line and thick solid line show average -2SD, mean and +2SD respectively. SD, standard deviation.

Table 6. Eigenvalues and proportions of principal components of the larval IO3 neuromast ablation elliptic Fourier descriptors.

	PC1	PC2	PC3	PC4	PC5
Eigenvalue*	2.07	1.09	0.37	0.16	0.13
Proportion (%)	50.60	26.56	9.15	3.90	3.16
Cumulative (%)	50.60	77.15	86.30	90.20	93.36

*Read eigenvalue as χ x 10^{-3}

Table 7. Eigenvalues and proportions of principal components of the larval IO4 neuromast ablation elliptic Fourier descriptors.

	PC1	PC2	PC3	PC4	PC5
Eigenvalue*	12.11	5.14	3.24	1.03	0.72
Proportion (%)	50.53	21.50	13.56	4.32	3.01
Cumulative (%)	50.63	72.13	85.69	90.01	93.02

*Read eigenvalue as χ x 10^{-3}

Table 8. Eigenvalues and proportions of principal components of the larval IO5 neuromast ablation elliptic Fourier descriptors.

	PC1	PC2	PC3	PC4	PC5
Eigenvalue*	8.89	2.50	0.91	0.73	0.26
Proportion (%)	63.31	17.84	6.47	5.20	1.85
Cumulative (%)	63.31	81.15	87.63	92.83	94.68

*Read eigenvalue as χ x 10^{-3}
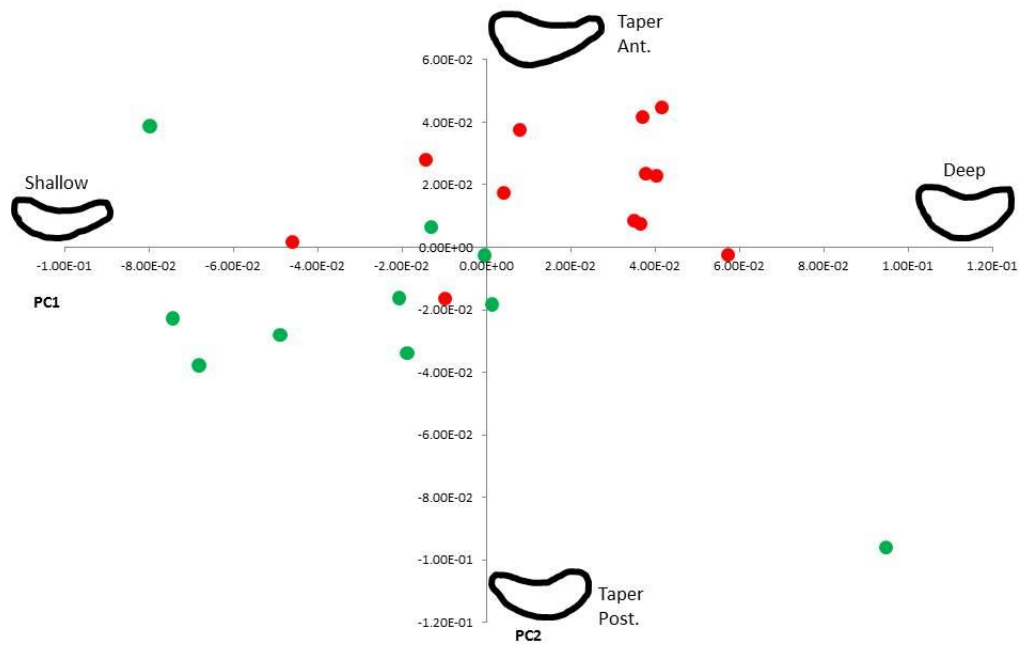
Figure 26. Scatter graphs of scores on principal components 1 and 2 for IO3 elements from larval neuromast ablation (red) and control (green) specimens. Also reconstructed shapes representing the variance are shown at the axes end-points. Some grouping is seen in ablation elements in the quadrant representing deeper, anterior-tapered elements (top right quadrant).
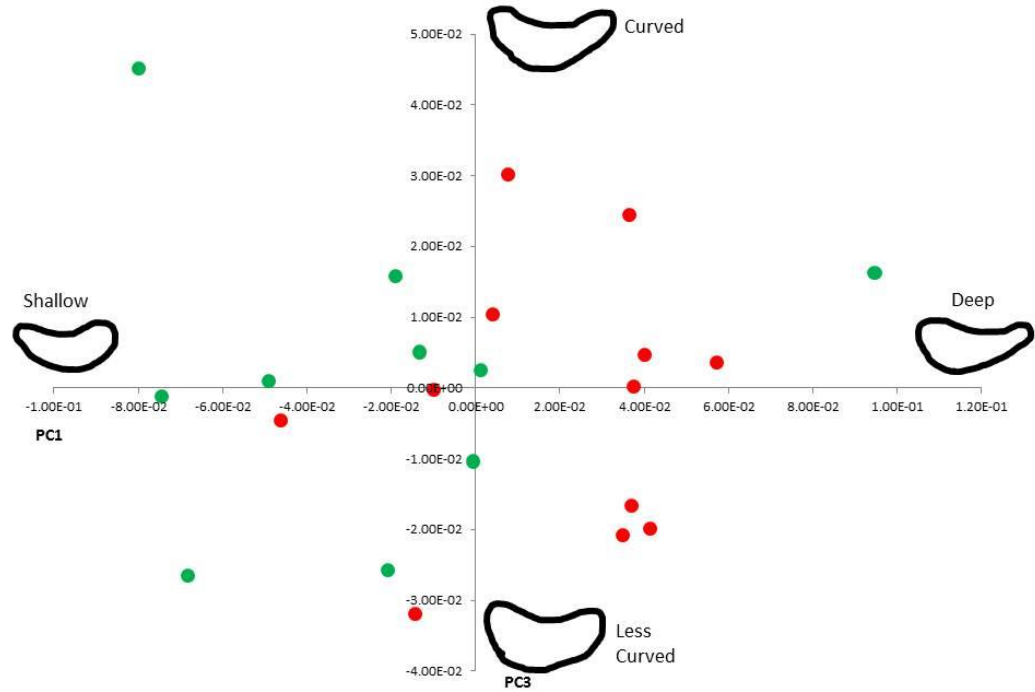
Figure 27. Scatter graphs of scores on principal components 1 and 3 for IO3 elements from larval neuromast ablation (red) and control (green) specimens. Also reconstructed shapes representing the variance are shown at the axes end-points. The mean shape of ablation elements fall on the positive side of the PC1 axis for deep (in the dorsoventral direction) IO3 elements. No specific grouping is observed along PC3.
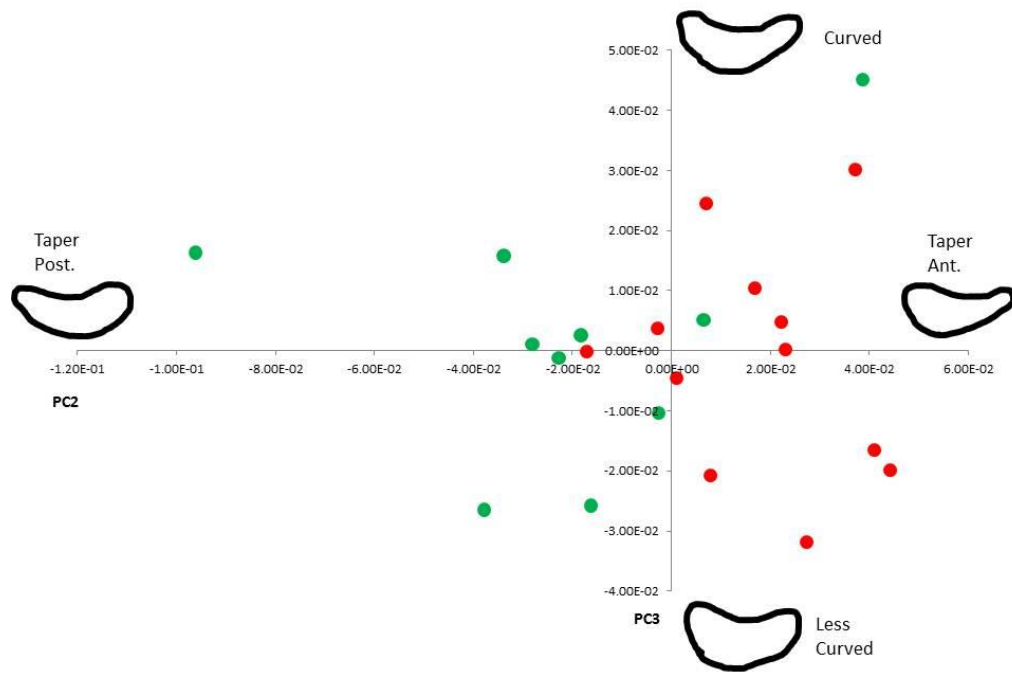
Figure 28. Scatter graphs of scores on principal components 2 and 3 for IO3 elements from larval neuromast ablation (red) and control (green) specimens. Also reconstructed shapes representing the variance are shown at the axes end-points. The ablation elements group towards the positive end of the PC2 axis for anterior taper direction as flat, wing-like extensions extend posteriorly. No specific grouping is observed along the PC3 axis.

Figure 29. Variations in infraorbital four shape accounted for by the 1st, 2nd, and 3rd principal components following larval neuromast ablation. The contour variance of each principal component is shown: broken line, thin solid line and thick solid line show average -2SD, mean and +2SD respectively. SD, standard deviation.

Figure 30. Scatter graphs of scores on principal components 1 and 2 for IO4 elements from larval neuromast ablation (red) and control (green) specimens. Also reconstructed shapes representing the variance are shown at the axes end-points. No specific grouping is observed, however the range of ablation specimens is much larger along both axes compared to control specimens.
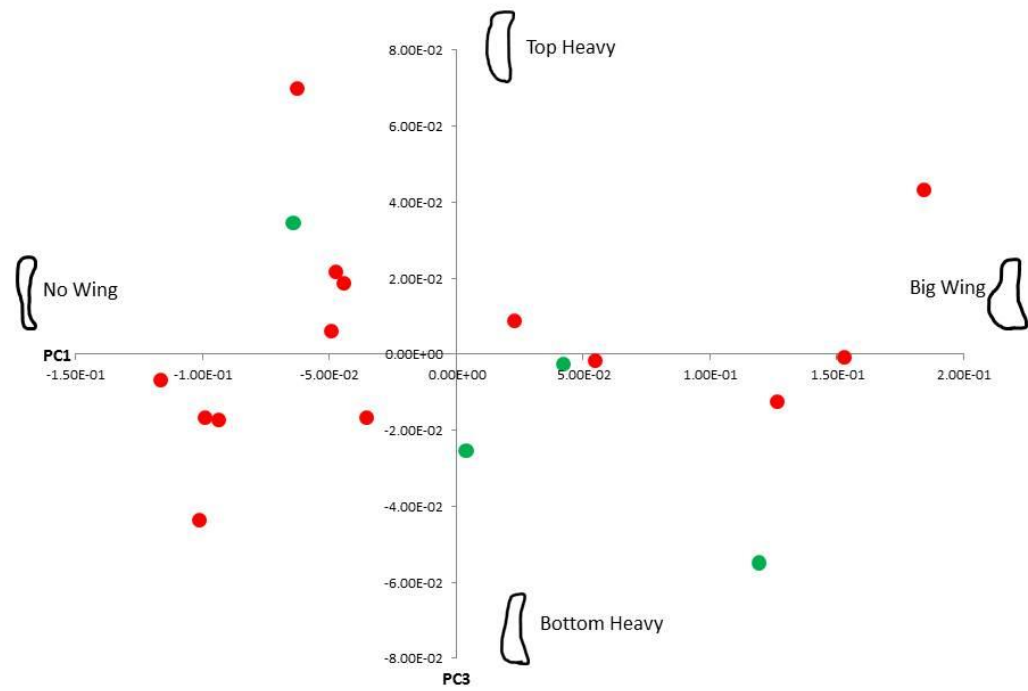
Figure 31. Scatter graphs of scores on principal components 1 and 3 for IO4 elements from larval neuromast ablation (red) and control (green) specimens. Also reconstructed shapes representing the variance are shown at the axes end-points. No specific grouping is observed.
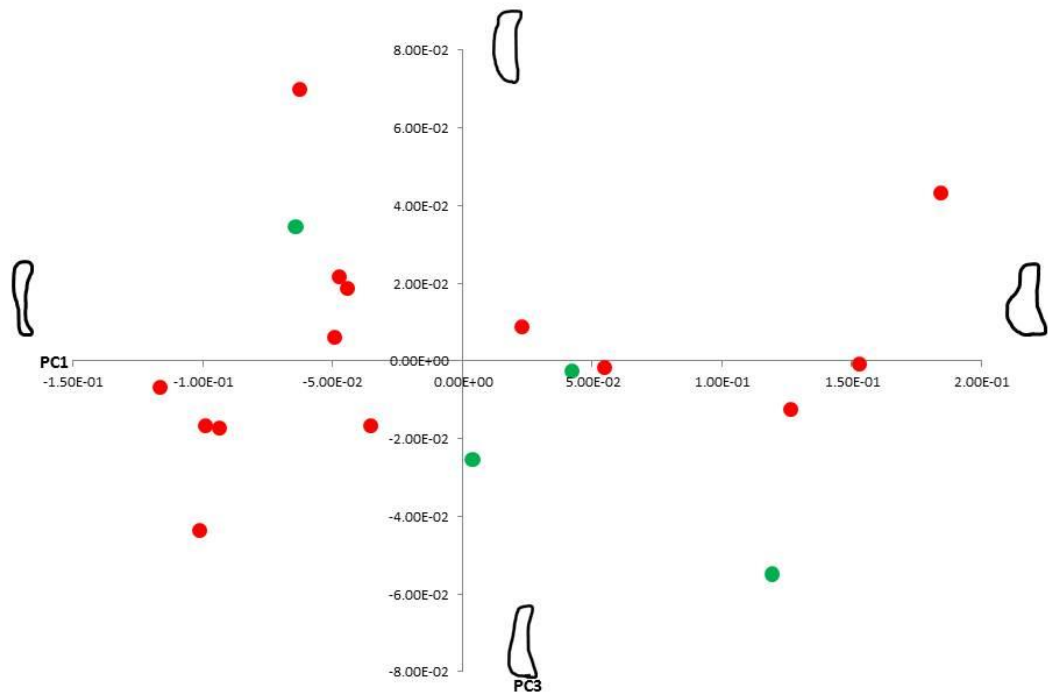
Figure 32. Scatter graphs of scores on principal components 2 and 3 for IO4 elements from larval neuromast ablation (red) and control (green) specimens. Also reconstructed shapes representing the variance are shown at the axes end-points. No specific grouping is observed.

Figure 33. Variations in infraorbital five shape accounted for by the 1st, 2nd, and 3rd principal components following larval neuromast ablation. The contour variance of each principal component is shown: broken line, thin solid line and thick solid line show average -2SD, mean and +2SD respectively. SD, standard deviation.
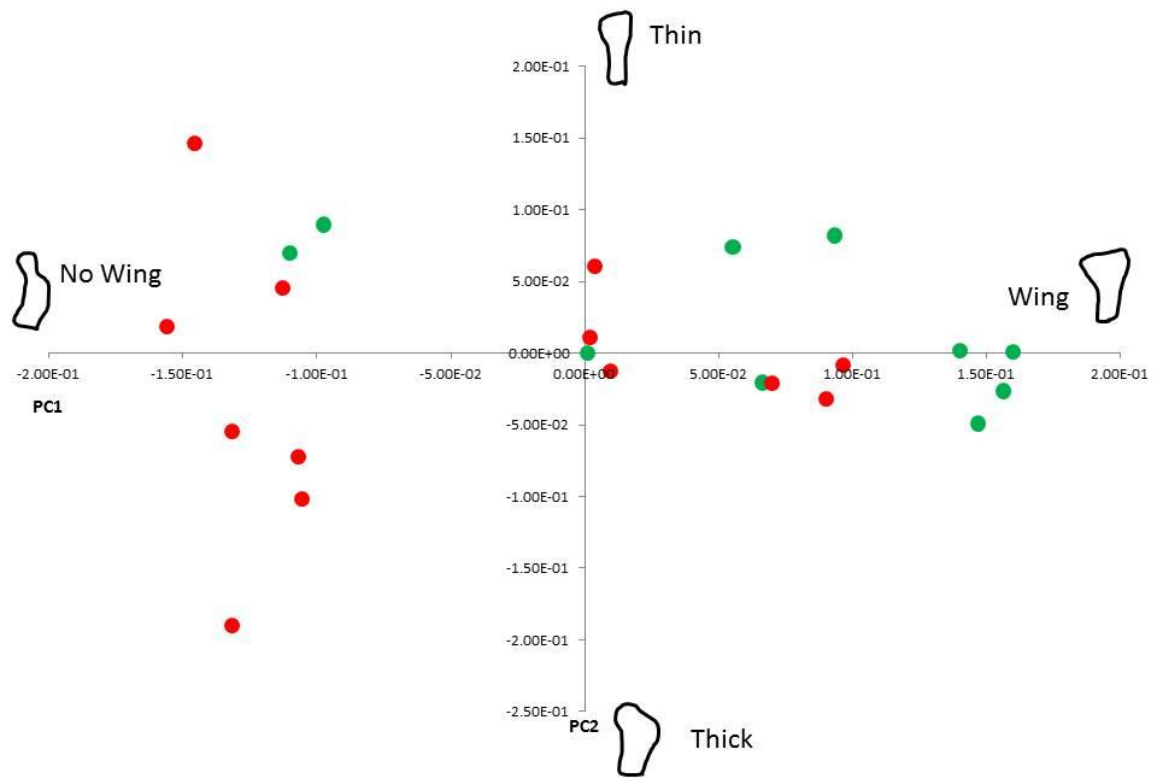
Figure 34. Scatter graphs of scores on principal components 1 and 2 for IO5 elements from larval neuromast ablation (red) and control (green) specimens. Also reconstructed shapes representing the variance are shown at the axes end-points. No specific grouping is observed.
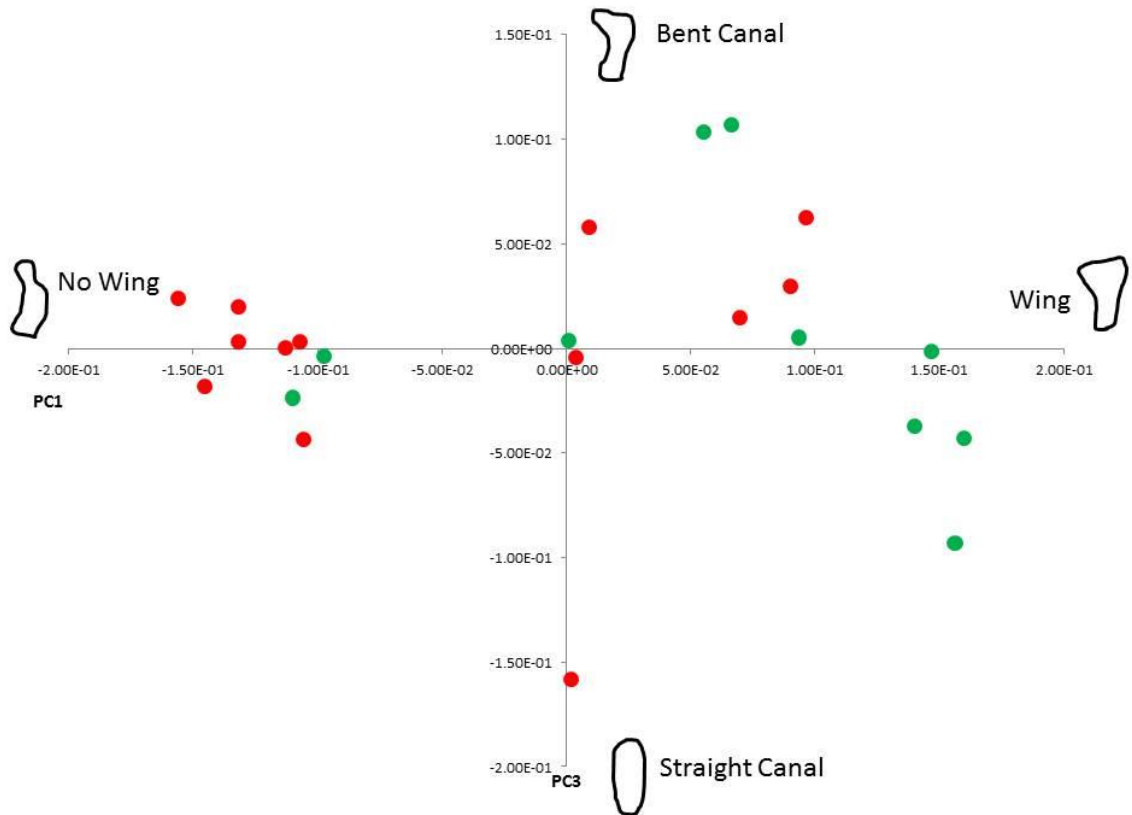
Figure 35. Scatter graphs of scores on principal components 1 and 3 for IO5 elements from larval neuromast ablation (red) and control (green) specimens. Also reconstructed shapes representing the variance are shown at the axes end-points. No specific grouping is observed.
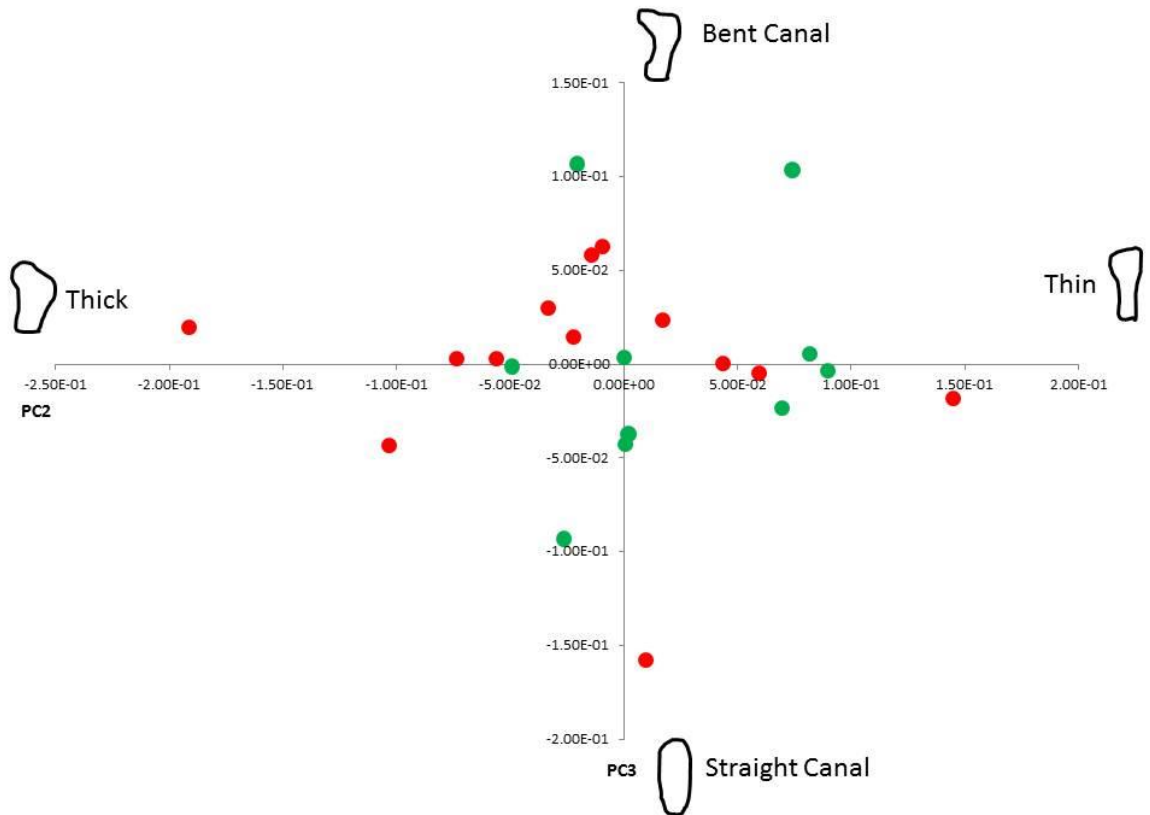
Figure 36. Scatter graphs of scores on principal components 2 and 3 for IO5 elements from larval neuromast ablation (red) and control (green) specimens. Also reconstructed shapes representing the variance are shown at the axes end-points. No specific grouping is observed.

3.3.2.4 Shape analysis of adult IO bones after juvenile neuromast ablations

To statistically analyze any shape differences between IO bones of adult (4-5 month old) juvenile neuromast ablation and control specimens a shape analysis was performed in the software program SHAPE. Shape analyses were performed separately for IO3 and IO5, comparing juvenile neuromast ablation to controls (untreated specimen).

The comparison of adult IO3 bones after juvenile IO3 neuromast ablation to control IO3 bones showed that the cumulative contribution of the first three principal components accounts for over 90% of the total variance (Table 9). The morphological meaning associated to each principal component was delineated (Figure 37). The first principal component accounts for 45% of the variance and corresponds to direction of taper of the element (the direction of outgrowth of flat aspect). The second principal component accounts for 39% of the variance and corresponds to the dorsoventral depth of the element. Finally, accounting for 7% of the variance, the third principal component describes the bend or curvature along the dorsal edge of the element. After plotting scatter graphs of the first three principal component scores some groupings of ablation and control specimens were seen with relation to morphology (Figures 38-40). The strongest grouping was observed when PC1 was plotted against PC2 as most of the ablation elements grouped close together in a cluster for deep, anteriorly-tapered IO3 elements (Figure 38). The ablation elements separated along the PC3 (bend) axis (Figure 39 and 40).

Table 9. Eigenvalues and proportions of principal components of the juvenile IO3 neuromast ablation elliptic Fourier descriptors.

|	PC1	PC2	PC3	PC4	PC5
Eigenvalue*	2.50	2.17	0.41	0.10	0.05
Proportion (%)	44.52	38.64	7.40	3.44	1.78
Cumulative (%)	44.52	81.16	90.57	94.01	95.79

*Read eigenvalue as $\chi \times 10^{-3}$

PC1
(Taper Direction)

PC2
(Thickness)

PC3
(Bend Curvature)
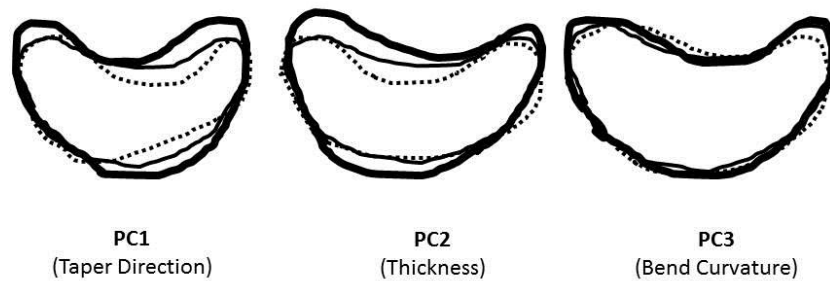
Figure 37. Variations in infraorbital three shape accounted for by the 1st, 2nd, and 3rd principal components following juvenile IO3 neuromast ablation. The contour variance of each principal component is shown: broken line, thin solid line and thick solid line show average -2SD, mean and +2SD respectively. SD, standard deviation.
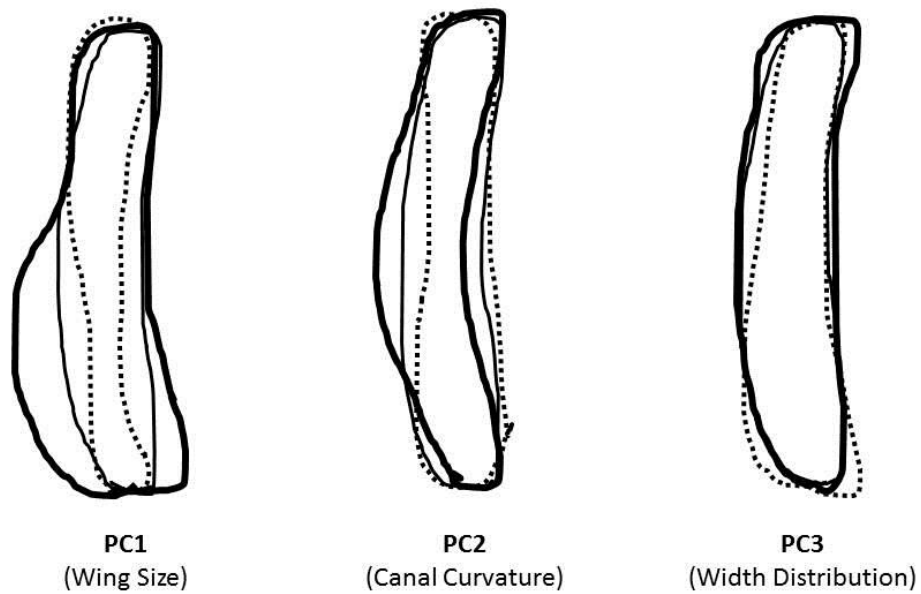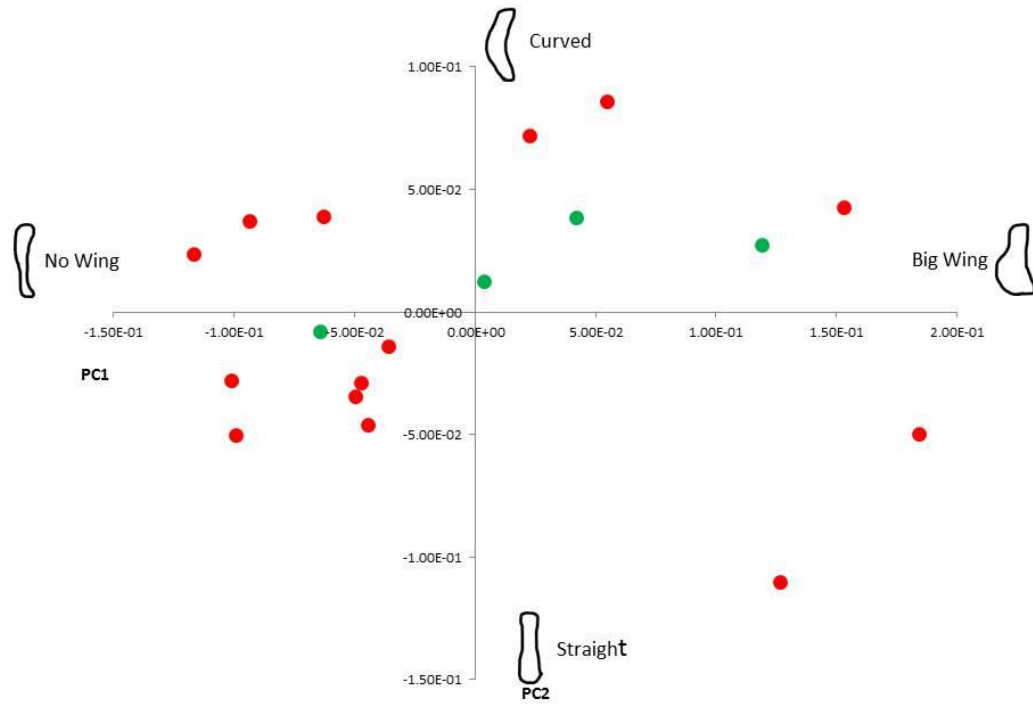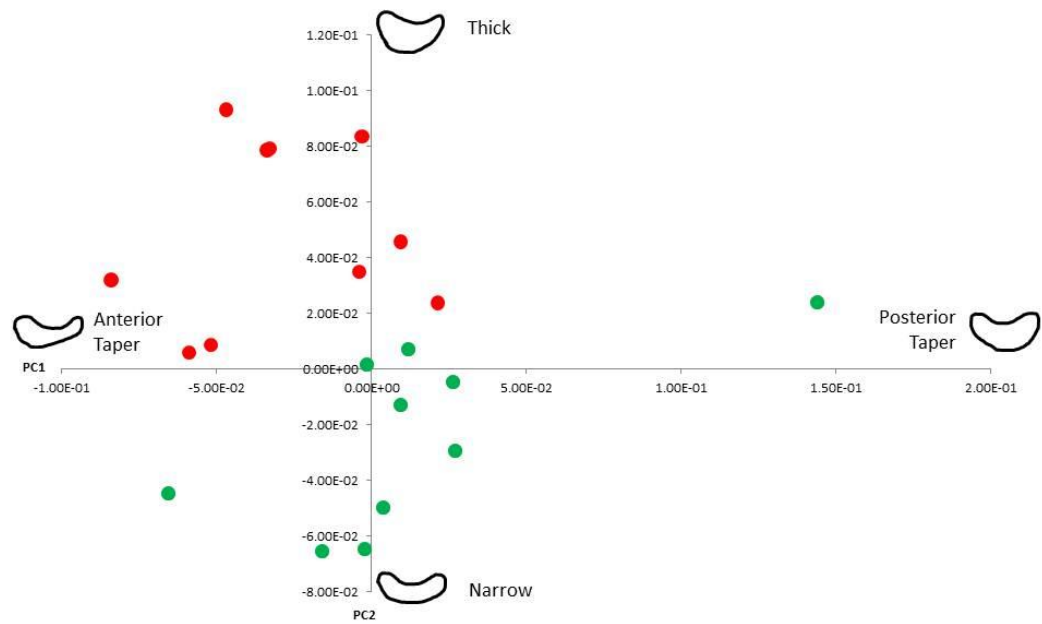
Figure 38. Scatter graphs of scores on principal components 1 and 2 for IO3 elements from juvenile IO3 neuromast ablation (red) and control (green) specimens. Also reconstructed shapes representing the variance are shown at the axes end-points. Grouping of ablation and control specimens is seen along the first and second principal component axes: ablation elements tend to be anteriorly tapered and have a deeper dorsoventral length.
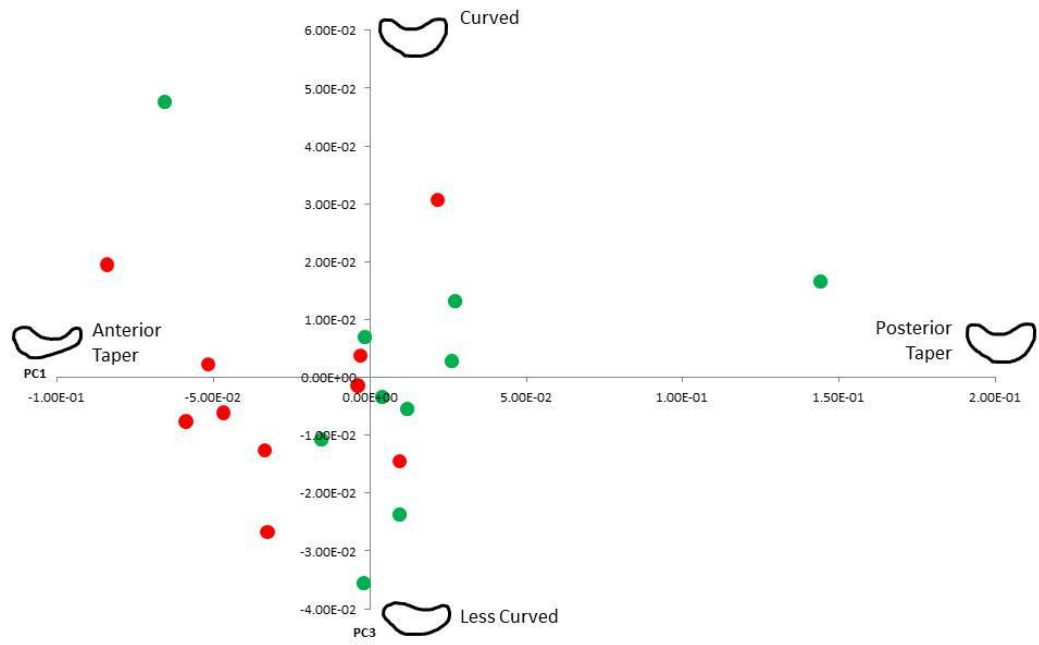
Figure 39. Scatter graphs of scores on principal components 1 and 3 for IO3 elements from juvenile IO3 neuromast ablation (red) and control (green) specimens. Also reconstructed shapes representing the variance are shown at the axes end-points. Grouping is observed along the first principal component axis, but specimens separate along the principal component three axis corresponding to curvature of the dorsal edge of the element.
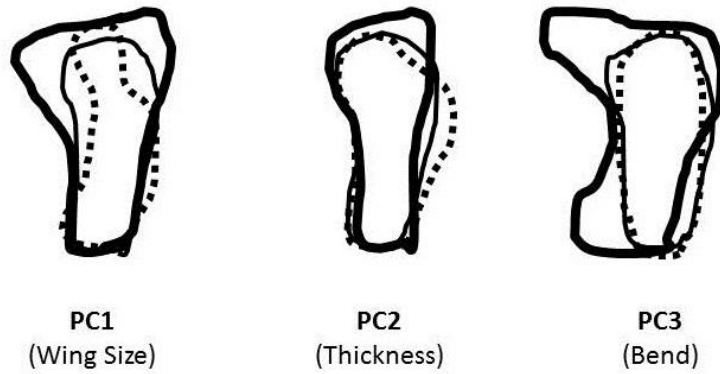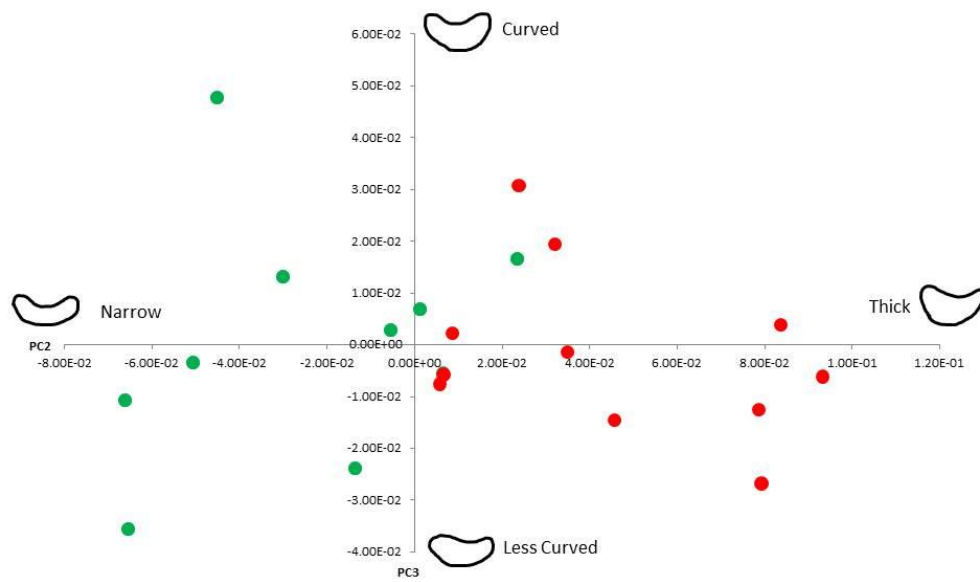
Figure 40. Scatter graphs of scores on principal components 2 and 3 for IO3 elements from juvenile IO3 neuromast ablation (red) and control (green) specimens. Also reconstructed shapes representing the variance are shown at the axes end-points. Grouping of ablation and control specimens is seen along the second principal component axis, but specimens separate along the principal component three axis corresponding to curvature of the dorsal edge of the element.

When adult IO5 juvenile neuromast ablation specimens' IO5 bones were compared to control IO5 bones, the cumulative contribution of the first three principal components is for 87% of the total variance (Table 10). The morphological meaning associated to each principal component was delineated (Figure 41). The first principal component corresponds to the presence of a canal bend compared to the wing size in the element and describes 41% of the variance in shape. The second principal component describes the roundness in the dorsal edge of the element and describes 29% of the shape variance observed. Finally, the third principal component describes the size of the flat, wing-like extension of the element and describes 17% of the shape variation. After plotting scatter graphs of the first three principal component scores, no groupings of specimens were observed, however a larger range in shape is seen in ablation specimens along PC2 (Figures 42-44).

In summary, the shape analyses comparing adult IO bones after juvenile neuromast ablation to controls show that the first three principal components describe approximately 90% of the variance in shape, of which the first component describes almost 50% of that variance. It is interesting that the shape characteristic that corresponds to the first principal component for IO3 ablations (direction of taper) is unique to IO3 bones. In addition, ablation and control specimens show grouping for this characteristic. Also, the first principal component for IO5 ablations describes the favouring of the canal bend instead of outgrowth of the flat wing; however no grouping was seen in this character.

Table 10. Eigenvalues and proportions of principal components of the juvenile IO5 neuromast ablation elliptic Fourier descriptors.

	PC1	PC2	PC3	PC4	PC5
Eigenvalue*	11.74	8.37	4.92	1.07	0.79
Proportion (%)	40.83	29.01	17.13	3.71	2.76
Cumulative (%)	40.83	69.84	86.96	90.68	93.44

*Read eigenvalue as χ x 10^{-3}

PC1
(Bend:Wing)

PC2
(Dorsal Edge Shape)

PC3
(Wing Size)
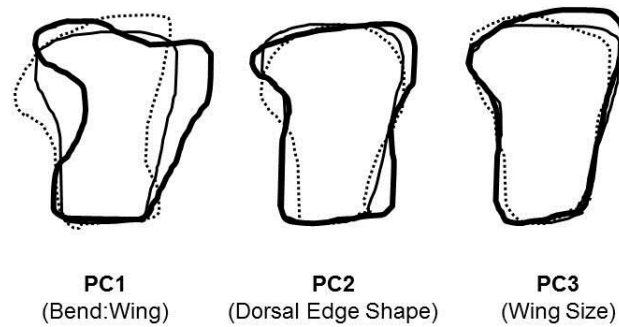
Figure 41. Variations in infraorbital five shape accounted for by the 1st, 2nd, and 3rd principal components following juvenile IO5 neuromast ablation. The contour variance of each principal component is shown: broken line, thin solid line and thick solid line show average -2SD, mean and +2SD respectively. SD, standard deviation.
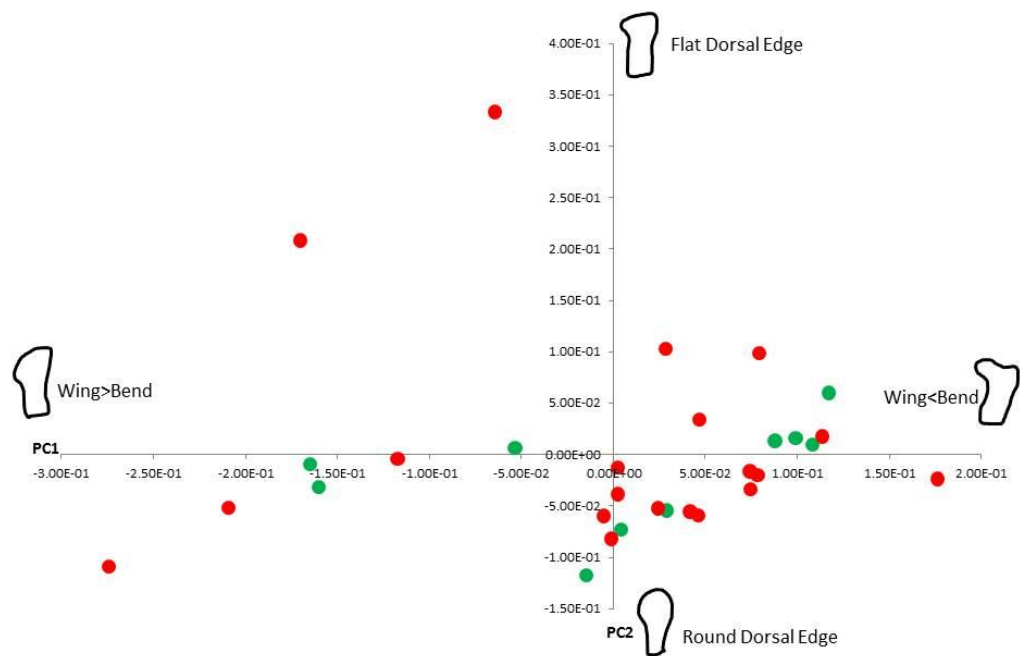
Figure 42. Scatter graphs of scores on principal components 1 and 2 for IO5 elements from juvenile IO5 neuromast ablation (red) and control (green) specimens. Also reconstructed shapes representing the variance are shown at the axes end-points. No specific grouping of elements was observed.
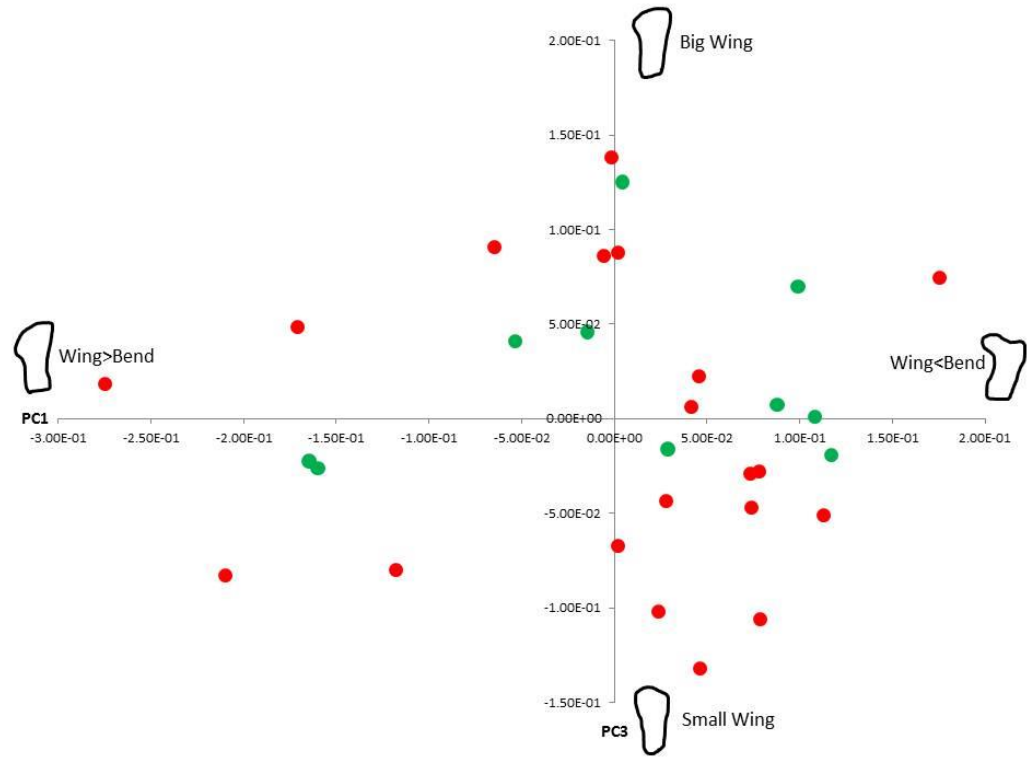
Figure 43. Scatter graphs of scores on principal components 1 and 3 for IO5 elements from juvenile IO5 neuromast ablation (red) and control (green) specimens. Also reconstructed shapes representing the variance are shown at the axes end-points. No specific grouping of elements was observed.
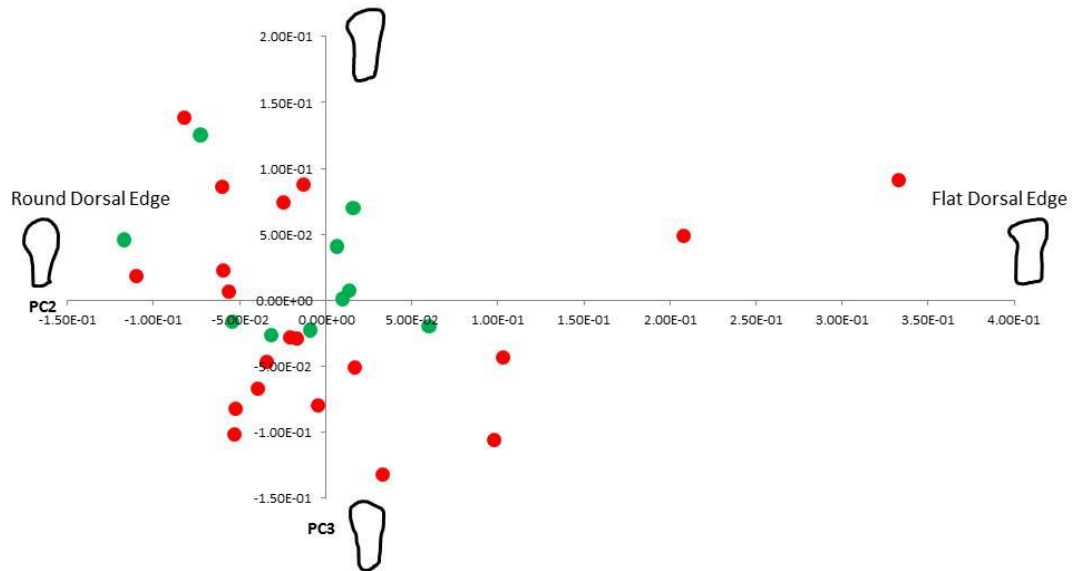
Figure 44. Scatter graphs of scores on principal components 2 and 3 for IO5 elements from juvenile IO5 neuromast ablation (red) and control (green) specimens. Also reconstructed shapes representing the variance are shown at the axes end-points. No specific grouping of elements was observed, however the range of IO5 element shape is along PC2 is much larger for ablation elements.

4.0 Discussion

4.1 The Sequence of Infraorbital Bones is Robust in Zebrafish

As observed by Cubbage and Mabee (1996) the infraorbital bones always developed in a predictable sequence. I think that that this sequence is most likely patterned by multiple mechanisms that work together to ensure that infraorbitals are induced, even in the event of developmental perturbation. Two mechanisms in particular that can alter the sequence induction of development are mechanical stimulation of osteogenesis and delayed induction.

In the case of infraorbital bones, the first phase of osteogenesis involves the induction of neural crest cells (ncc) into a skeletogenic cell lineage. Induction of ncc derived flat bones (such as the IO bones) typically occurs via epithelial-mesenchymal interactions; however the specific details of this mechanism for infraorbital bones has not been investigated. Following induction, condensation formation commences which involves the aggregation of cells into a condensation; this step is required for the next phase of osteogenesis, namely differentiation, to take place. Previous studies have shown that mechanical stimulation is involved in the transition from condensation to differentiation. For example, Rath et al., (2008) showed that mechanical stimulation (i.e. compression) of rat calvariae cells in culture results in osteogenic effects. Following compression, the cultured pre-osteoblasts increased proliferation and secretion of extracellular matrix and an increase in the induction of *BMP-2, Runx2, and Smad5* was observed. Adriaens and Verraes (1998) discussed the relationship between the sequence of cranial bone ossification and mechanical stimulation in the developing African catfish skull and found that the sequence of bone development in the skull was correlated to mechanical stimulation. An example of mechanical stimulation of osteogenesis specific to

zebrafish craniofacial development is the following observation recently discussed by Danos and Staab (2010). In the zebrafish jaw, the kinethmoid begins ossifying from its cartilage precursor at the ligamentous insertion point only when force is imposed. The concept of mechanical stimulation of osteogenesis could be applied to describe the sequence of infraorbital bone development. Infraorbital one forms first in the series and is positioned adjacent to the maxilla and was observed during dissection to be connected to the maxilla by connective tissue (i.e. ligaments). Since IO1 is situated directly adjacent to the maxilla, it experiences vigorous movement due to jaw movement during eating. In another study, Hernández (2000) investigated the ontogeny of feeding mechanisms in zebrafish. At the period prior to the onset of IO1 mineralization (6.0-10.0 mm SL) jaw open and closure velocities are approaching their peak and the amount of time required to reach maximum jaw gape peaks between 6.0-10.0 mm SL (Hernández 2000). After considering the positioning of all of the IO bones, I hypothesize that IO1 probably experiences the most mechanical stimulation out of all the bones in the series. I deduce that the mechanical stimulation of IO1 due to its association to the maxilla influences IO1 to mineralize first in the IO series as the region of IO1 is subjected to mechanical forces due to the movement of the jaw, and mechanical forces have been shown to induce mineralization.

Infraorbitals three and five are next in the sequence to mineralize. Although IO5 does not have any muscle insertions, it is situated directly beside the anterolateral knob of the sphenotic that has muscle insertions from the levator arcus palatine muscle (Cubbage and Mabee, 1996). This muscle is involved in the lifting of the hyoid complex during suction feeding which is present in larval fish and increases speed as zebrafish approach adulthood (Hernández 2002, Hernández et al., 2005). Since this muscle insertion site is

immediately posterior to the IO5 region, a subsequent increase in contraction speed could cause mechanical stimulation for osteogenesis in this element. Finally, IO3 is located dorsal to the preopercule that is part of the overlapping opercular series (Cubbage and Mabee, 1996). The movement of the opercular series during respiration translates into mechanical stimulation of the IO3 region and could stimulate osteogenesis. Altogether, the mineralization of the first three bones in the IO series ossification sequence could be stimulated by mechanical forces as previously described in the African catfish and zebrafish skull development (Adriaens and Verraes, 1998).

Infraorbital two and four mineralize last in the sequence (IO4 prior to IO2) and both share the characteristic of having adjacent IO bones on either side. Adjacent bones in the IO series are never observed to ossify at the same time or consecutively. This pattern is most likely a mechanism to ensure the proper development of the series as it allows for a recovery mechanism if one of the IO bones is damaged. This idea of delayed induction has previously been discussed regarding a different series of intramembranous bones in the vertebrate eye, the scleral ossicles of chickens (Duench and Franz-Odendaal, 2012). The scleral ossicles were observed to compensate for adjacent perturbed ossicles at specific developmental time-points. It was hypothesized that the sequential induction of groups of scleral ossicles during a period of time provided opportunities for the mesenchyme to compensate for the loss of an ossicle (Duench and Franz-Odendaal, 2012). In the case of the IO series, the sequential development of IO bone ossification over an extended period of time may also provide opportunities for the mesenchyme to respond to the loss of an IO bone.

In summary, the sequence of IO bone development is not random and likely involves the coordination of mechanical stimulation and temporal patterns of inductive

103

signaling. This sequence also serves a protective purpose, allowing for recovery following damage thus contributing to the developmental robustness of this series of bones.

4.2 The Formation of Lateral Line Canal Walls Occurs in Segments

The lateral line canal walls of fish have been hypothesized to mineralize in segments, that first form around neuromasts and later adjacent segments fuse forming a complete canal wall (Webb and Noden 1993). However, while this pattern of canal wall outgrowth may be due to induction by canal neuromasts, it could also be due to a mechanism of bone outgrowth unrelated to neuromast induction. Kimmel et al., (2010) describes the pattern of spur and veil outgrowth in the zebrafish operculum located posterior to the IO series. This outgrowth pattern was described to occur when shape changes occur in a bony element. Spur and veil mineralization includes the appearance of adjacent spurs of mineralized matrix along the axis of outgrowth that increase in number and length. A veil of bone matrix eventually is deposited between adjacent spurs connecting them. The pattern of canal wall outgrowth observed in the IO bones was observed to include adjacent segments of bone outgrowth along the canal length, which increased in number and size and eventually connected with one another to form a uniform wall. The mode of ossification of canal walls maybe similar to the spur and veil outgrowth observed in the zebrafish operculum. It can also be noted that the flat, wing-like extension of the IO bones does not exhibit this pattern of outgrowth, as this aspect of the element seems to expand outwards from the border of the element. Investigation into the mode of morphogenesis of both the canal and flat aspect of the IO bones should be carried out in order to better understand the development of the series. Insight into the

canal wall ossification patterns may provide additional insight into the potential role neuromasts play in inducing canal wall ossification by determining if osteoblasts aggregate into clusters initially at the location of canal neuromasts. If segments form initially in neuromast regions of the canal then this pattern of mineralization supports neuromast induction of bone. Alternatively, if segments (and osteoblasts) are not initially located in the neuromast region then the pattern does not provide any support for the concept of neuromast induction of bone.

4.3 The Lateral Line Canal Wall Closest to the Eye Initiates Canal Roof Enclosure

During the outgrowth of IO1, IO3 and IO5 canal walls in zebrafish, the canal wall closest to the eye extends farther than the wall further from the eye. In these bones it was clear that the wall closest to the eye closes over the canal roof. This pattern of wall outgrowth could be mediated by signaling by the eye, as the eye has been previously shown to influence the outgrowth of circumorbital bones in teleosts (Yamamoto et al., 2003; Dufton et al., 2012; Dufton 2013). For example, following lens removal in the Mexican tetra, *Astyanax mexicanus,* outgrowth of circumorbital bones was observed to occur into the orbital cavity. Dufton (2013) also conducted this experiment in the zebrafish; here, circumorbital bones were similar. Reasoning for this observation included the involvement of mechanical forces, paracrine factors that inhibited bone expansion into a functional eye (Dufton et al., 2012). Forces preventing bone expansion into the function eye could theoretically also influence the leading canal wall (closest to the eye) to fold over the canal, away from the eye, resulting in the closure of canal wall roof. Additionally, the wall closest to the eye may lead canal roof enclosure to provide optimal water flow through the canal. Modelling of the eye and circumorbitals should be done to

better understand the mechanical forces at play and also the fluid mechanics involved in this system.

4.4 Canal Roof Mineralization is Incomplete

Although the literature has repeatedly suggested that the infraorbital neuromasts in zebrafish are enclosed by a mineralized bony canal roof in zebrafish (i.e. in Gregory, 1933; Cubbage and Mabee, 1996; and Webb and Shirey, 2003), I never observed the complete mineralization of the canal roof even in 3-year-old fish. The canal wall structure observed in infraorbital bones consists of mineralized canal walls that have approached one another, but a small distance remains between the walls in the roof region. It is possible, that previous authors did not look closely enough at this area or that their criteria for enclosure did not require canal roof fusion. Occasionally, a small portion of the canal wall length does fuse (e.g in Figure 7L), however it does not follow that the entire roof will fuse over time. Indeed, my results do not suggest this (Figure 12A and B). Webb and Shirey (2003) are the only authors to have specifically investigated infraorbital canal roof formation in zebrafish. This analysis used SEM analyses of adult IO1-5 bones. This SEM analysis did not assess the degree of canal roof mineralization but rather the appearance of an enclosed canal structure, the identification of the tissue enclosing the canal was not carried out (i.e. epithelial tissue, osteoid, mineralized bones). In this study the epithelial canal roof was described to form before the bony canal roof, and the observation of canal enclosure did not discriminate between these two roof components. In this thesis, and after double staining IO bones with both Alizarin Red S and Alcian Blue, I clearly show that canal roofs stain with Alcian Blue. Alcian blue indicates the presence of glycosaminosglycans or muccopolysaccharides (Young et al., 2006),

indicating osteoid o (i.e. unmineralized bone). Another possibility for incomplete canal roof mineralization is that the IO lateral line canal roof in laboratory zebrafish may never mineralize completely. This observation is in agreement with a general lack of flat bone fusion in the calvariae of the zebrafish skull (Quarto and Longaker 2005).

Also, the zebrafish in the lab are many generations removed from wild populations and laboratory fish are not exposed to predators and are fed frequently so prey capture is not an issue. It has been shown in an experiment comparing wild and hatchery born trout that hatchery born fish show forms of domestication as predator avoidance strategies are diminished in hatchery raised fish compared to wild fish (Álvarez and Nicieza, 2003). This loss of predator avoidance could also be related to a less developed mechanosensory system (including incomplete canal wall mineralization). An investigation of the lateral line canal mineralization in wild zebrafish should be carried out to determine if incomplete canal roof mineralization is an artifact of the laboratory environment or if it is indeed a unique feature of zebrafish.

4.5 Skeletogenic IO5 Condensations Recover from Ablation

Following the skeletogenic condensation ablation recovery of the ablated element re-appears by five days post-ablation. I previously discussed that the absence of one element in the infraorbital series during development would result in compensation by adjacent elements as hypothesized by Duench and Franz-Odendaal (2012) in scleral ossicle development in chick. If one i) accepts that IO5 buds off from IO4 as my data suggests (Chapter 3.2.1, Figure 14) and ii) considers this recovery of IO5 as an enlargement of IO4 (which is also the next IO to undergo osteogenesis in the IO series), then the recovery mechanism I observed is indeed similar to that observed in chick scleral

ossicles as the removal of one IO bone resulted in the expansion of an adjacent IO bone into the area of the ablated IO bone. Further investigation is required to determine if the origin of the recovered IO5 element is the adjacent IO4 element. For example, future studies should investigate earlier stages of IO5 recovery that were not covered in this project (between 24 hours and 4 days post-ablation). If there is a shared recovery mechanism between chick scleral ossicles and zebrafish infraorbitals there are future implications for a shared vertebrate response to developmental perturbations in series of cranial flat bones such as these.

Additional support for this hypothesis includes the observation of the recovered adult IO5 element which appears truncated (smaller and lacking the flat projection) in three of the four ablation specimens. In the case that the recovered IO5 reformed by compensation from IO4 there would be a delay in IO5 ossification (IO4 normally is induced and ossifies later than IO5). A delay would have affected the outgrowth of the dorsal aspect of the element if separate, temporally specific, signaling were involved in the development of the flat, wing-like extension. Multiple signaling events have been previously demonstrated in the shaping of the frontonasal skeleton and beak in chick, through temporal- and spatial-specific changes of the proliferative zones (e.g. Wu et al., 2004). The outgrowth of the chick frontonasal mass is directed by the growth factor FGF from the ectodermal zone (Richman et al., 1997), whereas, the width of the beak has been shown to be regulated by the morphogen *BMP-4* (Wu et al., 2004). Together, these two signals are involved in the shaping of the beak. Thus, in bone development, the location and timing of inductive signaling is critical to the outcome of the shape of a skeletal element. The truncated IO5 that recovers following ablation could be due to the loss of an induction signal for outgrowth of the flat-wing extension as it could have missed the

time-point for induction of IO5 flat wing outgrowth which forms following the formation of the canal aspect. An analysis of growth factor and morphogen signaling in the IO region during IO series development is required to fully understand the process of IO shape acquisition.

Alternatively, in the case that the reformed IO5 element did not bud off from an expansion of IO4 an additional bone recovery mechanism must exist. In another osteoblast ablation experiment in larval medaka by Willems et al., (2012), osteoblasts were targeted and ablated using a cytotoxic agent and following ablation, a decrease in osteoblasts (which were observed to undergo apoptosis) and ossification was observed specifically in the cleithrum and operculum. Following ablation, new osteoblasts gradually appeared indicating the potential for the skeletogenic cell lineage to possess regenerative properties; however, more insight is required on the exact origin of these new osteoblasts (i.e. differentiation of osteoprogenitor cells vs. proliferation of osteoblasts). It is possible that following condensation ablation, a similar regenerative mechanism was involved in the recovery of osteoblast and subsequent regrowth of the ablated IO5 element.

Altogether, the result of bone recovery following ablation presents an interesting scenario involving natural developmental rescue mechanisms that exist in organisms. Considering that the ablation took place during the time-span of normal IO development, developmental mechanisms like delayed induction are most likely to be involved. More research should be done to enhance understanding this recovery mechanism.

4.6 Ablated neuromasts recover from ablation

Ablation of neuromasts has been previously performed through the application of aminoglycoside antibiotics (i.e. neomycin) (Harris et al., 2003; Namdaran et al., 2012) and copper sulphate (Hernandez et al., 2007) in zebrafish, the use of adhesive tape in the Mexican tetra (*Astyanax mexicanus*), or through laser ablation in the salamander (Balak et al., 1990) and axolotls (Jones and Corwin, 2012). Following ablation, the recovery or regeneration of neuromasts has been reported (salamander: Balak et al., 1990; axolotls: Jones and Corwin 1996; zebrafish: Harris et al., 2003; zebrafish: Namdaran et al., 2012). The mechanism of neuromast recovery following ablation has been investigated in three organisms and several studies agree that new hair cells arise via proliferation from the neuromast support cells (salamander: Balak et al., 1990; axolotls: Jones and Corwin 1996; zebrafish: Harris et al., 2003; zebrafish: Namdaran et al., 2012). The recovery of neuromasts following ablation in my study is also therefore likely to have occurred through proliferation from support cells.

Hernández and colleagues investigated the mechanism of neuromast regeneration in the larval zebrafish following exposure to copper sulphate (Hernández et al., 2007). In this study, the severity of the neuromast ablation had an effect on both the duration of neuromast recovery as well as the mechanism of recovery. When zebrafish were exposed to mild levels of copper sulphate they only experienced damage to mature hair cells, while the support cells were unaffected (Hernández et al., 2007). This incomplete neuromast ablation resulted in regeneration in less than 24 hours, and these new hair cells arise from non-dividing precursors (Hernández et al., 2007). However, when exposed to a higher dose of copper sulphate the whole neuromast (support cells included) was ablated and recovery did not occur after more than 24 hours (Hernández et al., 2007). When

recovery did occur it involved proliferation of pre-mitotic precursors support cells (Hernández et al., 2007). The location of the mitotically active cells support cells of the primordium was at the base of the neuromast underlying the neuromast hair cells in the region of the support cells (Hernández et al., 2007). In my study, following neuromast ablation with the laser there was no neuromast recovery until after 24 hours, indicating that, similar to the copper sulphate experiment, the laser ablation likely affected the entire neuromast structure (hair cells and support cells). Following, I would hypothesize that the recovered neuromast reformed from the proliferation of a pre-mitotic precursor support cells as well.

Neuromast regeneration has been shown to be directly related with *Sox2* expression, which is under the control of glial cells (Grant et al., 2005; López-Schier and Hudspeth, 2005). The loss of the lateral line nerve with its glia results in premature and ectopic neuromast production (Hernández et al., 2007). During the neuromast ablation in my experiment it is unlikely that the lateral line nerve innervating the neuromast was damaged as the formation of ectopic neuromasts was not observed and histology following ablation does not support nerve damage.

4.7 Recovery of Neuromasts Occurs Faster in Juvenile Ablations Compared to Larval

In the neuromasts ablation experiments, neuromast recovery was observed to occur faster in juvenile specimens compared to larval specimens. One reason for this observation might be that larval fish have limited energy resources as they are still undergoing development and are dependent on their yolk for nutrients. Due to the limited energy reserve, larval zebrafish may not have enough available energy to invest in rapid neuromast recovery, whereas the juvenile fish have larger energy stores since they are not reliant on their yolk and have regularly access to food. An alternative hypothesis for this difference in neuromast recovery speed could be that the neuromast structure (including support cells) is smaller in the larval fish compared to the juvenile specimens. Over the lifespan of zebrafish, hair cells are added to zebrafish neuromasts as cell turnover is taking place (Metcalfe et al., 1985; Williams 2000). In the smaller neuromast of larval fish one would expect fewer neuromast pre-mitotic precursor cells are available to proliferate during neuromast recovery, ultimately resulting in a slower recovery compared to juvenile ablation specimens. It is also a possibility that both of these factors are responsible for the difference in neuromast recovery times observed in larval and juvenile neuromast ablation specimens. It would be interesting to compare the composition of the neuromast in larval and juvenile specimens to determine if there is a difference in the number of support cells using a transgenic strain of zebrafish where support cells fluoresce (i.e *sqET4* and *sqET20)*. Investigating the recovery of neuromasts following ablation in fish at an intermediate stage (between larval and juvenile stages) could also provide insight into the affect energy stores has on neuromast recovery, if any.

4.8 Neuromast Ablation Affects Canal Wall Mineralization but not IO Shape

The results of this investigation show that following neuromast ablation, the outgrowth of mineralized canal walls is significantly less in larval ablations as well as juvenile IO3 ablations compared to control IO bones. These results strengthen my hypothesis that neuromasts are involved in canal wall mineralization. It was surprising that the neuromast ablation at the larval stage 3-4 weeks prior to the hypothesized period of neuromast induction of canal walls, affected canal wall mineralization. Two potential mechanisms could explain the decrease in canal wall mineralization observed. First, both the larval and the juvenile ablations would have resulted in decreased canal wall mineralization if the neuromast ablation caused delay of the canal wall induction (due to the time required for the ablated neuromast to recover). A delay in induction could translate into a delay in mineralization, which would result in less mineralization in specimens of the same age. However, it is also possible that following ablation, the regenerated neuromast did not possess the same inductive potential as the original neuromast and induction was not as strong or that the inductive signal could not travel as far in the tissue. The observed decreased canal wall mineralization in juvenile IO3 ablation specimens, but not in IO5 ablation specimens supports this second proposed mechanism. IO3 has a long canal while IO5 has a short canal, a decrease in the range or strength of the inductive signal in recovered neuromasts would affect IO3 more, since its canal walls are much longer than IO5. I hypothesize the decreased canal wall mineralization observed was due to the neuromast ablation which could have delayed induction of canal wall mineralization or changed the inductive potential of the neuromast.

Finally, in the neuromast ablation experiment there was no strong effect on the adult shape of the affect IO bones. This was not a surprising observation considering that the hypotheses of neuromast inducing ossification of infraorbital bones only describes an effect on the bony canal walls. However, this does suggest that the flat bone portion is independent of the canal wall portion in these bones. The results from the developmental growth series support two phases of IO bone development, a canal phase and a flat-wing phase, either of which can occur first.

5.0. Summary

In summary, this thesis described the development and growth of the zebrafish infraorbital bones, tested the relationship between bones in the series and tested the relationship between these bones and the lateral line canal neuromasts. The description of the growth of the infraorbital bones showed that this series always develops in a consistent sequence. I hypothesize that this is due to temporal mechanical and signal induction. Investigating the relationship shared between infraorbital bones through a skeletogenic condensation ablation resulted in the observation of infraorbital bone recovery. I originally hypothesized that growth of one IO affects the development of the other IO bones in the series. The results of the condensation ablation support my hypothesis as following the ablation of the IO5 condensation IO4 was observed to have a role in the recovery of IO5. The long-debated relationship between lateral line canal neuromasts and bony canal walls surrounding them was tested through neuromast ablation and resulted in neuromast recovery and decreased canal wall mineralization. This result supports my original hypothesis that canal neuromasts have a role in the formation of canal wall mineralization. From this result, I hypothesize that similar to previous neuromast ablation studies, neuromast recovery occurs through proliferation of support cells and that there was a delay or change in the inductive potential of the recovered neuromast. More research is required to elucidate the extent of neuromast involvement in canal wall mineralization.

6.0 Conclusion and Significance

The IO series of bones is a developmentally complex system. The IO bones are a developmentally linked set of bones that have remained together in skull ontogeny throughout evolution. Clearly there must be developmental mechanisms in place to have maintained this bone series throughout 450 million years of evolution (Hildebrand and Milton, 2001; Schoch, 2006). The results of this study highlight the developmental complexity and robustness of these bones. The development and growth of the IO bones is complex as each IO bone is unique in its morphology and development. The recovery of ablated structures demonstrates rescue mechanisms that allowed for the infraorbital series to develop normally following perturbation and demonstrates that the development of individual IO bones affects other bones in the series. The mechanisms of developmental robustness should be investigated further as the infraorbital bones can be used to increase understanding of intramembranous bone patterning. The canal neuromasts were shown to play some role in canal wall mineralization indicating that the IO series is also an ideal system to further elucidate the interaction between hard tissues and soft tissue (i.e. placode derived neuromasts and overlying epithelium).

7.0 Bibliography

Adriaens, D. and Verraes, W. (1998). Ontogeny of the osteocranium in the African catfish, Clarias gariepinus Burchell (1822)(Siluriformes: Clariidae): ossification sequence as a response to functional demands. J. Morphol. 235, 183–237.

Alvarez, D. and Nicieza, A. G. (2003). Predator avoidance behaviour in wild and hatchery-reared brown trout: the role of experience and domestication. J. Fish Biol. 63, 1565–1577.

Baker, C. V. H. and Bronner-Fraser, M. (2001). Vertebrate Cranial Placodes I. Embryonic Induction. Developmental Biology 232, 1–61.

Balak, K. J., Corwin, J. T. and Jones, J. E. (1990). Regenerated hair cells can originate from supporting cell progeny: evidence from phototoxicity and laser ablation experiments in the lateral line system. J. Neurosci. 10, 2502–2512.

Carter, D. R., Beaupré, G. S., Giori, N. J. and Helms, J. A. (1998). Mechanobiology of skeletal regeneration. Clin. Orthop. Relat. Res. S41–55.

Couly, G., Grapin-Botton, A., Coltey, P., Ruhin, B. and Le Douarin, N. M. (1998). Determination of the identity of the derivatives of the cephalic neural crest: incompatibility between Hox gene expression and lower jaw development. Development 3445–3459.

Cubbage, C. and Mabee, P. (1996). Development of the cranium and paired fins in the zebrafish *Danio rerio* (Ostariophysi, Cyprinidae). J. Morphol. 121–160.

Danos, N. and Staab, K. L. (2010). Can mechanical forces be responsible for novel bone development and evolution in fishes? J. Appl. Ichthyol. 26, 156–161.

Devillers, C. (1947). Recherches dur le crane dermique des teleosteens. Annales de palaeontology, 33, 1–94.

Duench, K. and Franz-Odendaal, T. A. (2012). BMP and Hedgehog signaling during the development of scleral ossicles. Dev. Biol. 365, 251–258.

Dufton, M., Hall, B. K. and Franz-Odendaal, T. A. (2012). Early Lens Ablation Causes Dramatic Long-Term Effects on the Shape of Bones in the Craniofacial Skeleton of Astyanax mexicanus. PLoS ONE 7, e50308.

Dufton M. 2013. Early Lens Ablation Causes Dramatic Long-Term Effects on the Bones of the Craniofacial Skeleton of the Mexican Tetra, *Astyanax Mexicanus* [disstertation]. Halifax: Dalhousie University. 43-73.

Edsall, S. C. and Franz-Odendaal, T. A. (2010). A Quick Whole-Mount Staining Protocol for Bone Deposition and Resorption. Zebrafish 7, 275–280.

Farrell, A. P., Chech, J. J. J., Richards, J. G. and Stevens, E. D. eds. Encyclopedia of Fish Physiology.Volume 1. London: Elsevier.419-471.

Franz TA and Kidson SH. 1997. Mapping of interdigital apoptosis in the chick and duck hindlimb. South African Journal of Science 93: 85-88.

Franz-Odendaal, T. A. (2011). Induction and patterning of intramembranous bone. Frontiers in bioscience: a journal and virtual library 16, 2734–2746.

Ghysen, A. and Dambly-Chaudière, C. (2004). Development of the zebrafish lateral line. Curr. Opin. Neurobiol. 14, 67–73.

Grant K, Raible D, Piotrowski T. 2005. Regulation of latent sensory hair cell precursors by glia in the zebrafish lateral line. Neuron 45:69–80

Gregory, W. K. (1933). Fish skulls: a study of the evolution of natural mechanisms. American Philosophical Society.

Hall, B. (1981). The induction of neural crest-derived cartilage and bone by embryonic epithelia: an analysis of the mode of action of an epithelial mesenchymal interaction. J Embryol Exp Morphol. 305-320.

Hall, B. and Van Exan, R. (1982). Induction of bone by epithelial cell products. J. Embryol. Exp. Morph. 69, 37-46 .

Hall, B. K. (1986). The role of movement and tissue interactions in the development and growth of bone and secondary cartilage in the clavicle of the embryonic chick. J Embryol Exp Morphol 93, 133–152.

Hall, B. K. (2005). Bones and cartilage: developmental and evolutionary skeletal biology. London: Elsevier Academic Press. 3-39, 127-295.

Hall, B. K. and Horstadius, S. (1988). The Neural Crest. New York: Oxford University Press.

Harris, J. A., Cheng, A. G., Cunningham, L. L., MacDonald, G., Raible, D. W. and Rubel, E. W. (2003). Neomycin-Induced Hair Cell Death and Rapid Regeneration in the Lateral Line of Zebrafish (Danio rerio). J. Ass. Res.Otolaryngol. 4, 219–234.

Henderson, J. H. and Carter, D. R. (2002). Mechanical induction in limb morphogenesis: the role of growth-generated strains and pressures. Bone 31, 645–653.

Hernandez, L. P., Barresi, M. J. and Devoto, S. H. (2002). Functional morphology and developmental biology of zebrafish: reciprocal illumination from an unlikely couple. American zoologist 42, 222–231.

Hernandez, L. P., Patterson, S. E. and Devoto, S. H. (2005). The development of muscle fiber type identity in zebrafish cranial muscles. Anat. Embryol. 209, 323–334.

Hernández, L. P. (2000). Intraspecific scaling of feeding mechanics in an ontogenetic series of zebrafish, Danio rerio. J. Exp. Biol. 203, 3033–3043.

Hernández, P. P., Olivari, F. A., Sarrazin, A. F., Sandoval, P. C. and Allende, M. L. (2007). Regeneration in zebrafish lateral line neuromasts: Expression of the neural progenitor cell marker sox2 and proliferation-dependent and-independent mechanisms of hair cell renewal. Dev. Neurobiol. 67, 637–654.

Hildebrand, M. and Goslow, G. E. (2001). Analysis of vertebrate structure.5th Ed. New York: Wiley. 3-50, 113-170.

Iwata, H. and Y. Ukai (2002) SHAPE: A computer program package for quantitative evaluation of biological shapes based on elliptic Fourier descriptors. J. Hered. 93: 384-385

Iwata, H., S. Niikura, S. Matsuura, Y. takano and Y. Ukai (2004) Interaction between genetic effects and soil type in diallel analysis of root shape and size of Japanese radish (*Raphanus sativus L.*). Breeding Science 54: 313-318.

Jacobson, A. (1966). Inductive processes in embryonic development. Science (New York, NY) 152, 25.

Jacobson, A. G. and Sater, A. K. (1988). Features of embryonic induction. Development 104, 341–359.

Jiang, X., Iseki, S., Maxson, R. E., Sucov, H. M. and Morriss-Kay, G. M. (2002). Tissue Origins and Interactions in the Mammalian Skull Vault. Dev Biol 241, 106–116.

JM Richman, M Herbert, E Matovinovic, J Walin: Effect of fibroblast growth factors on outgrowth of facial mesenchyme. Dev Biol, 189, 135-147 (1997)

Jones, J. E. and Corwin, J. T. (1996). Regeneration of sensory cells after laser ablation in the lateral line system: hair cell lineage and macrophage behavior revealed by time-lapse video microscopy. J. Neurosci. 16, 649–662.

Kague, E., Gallagher, M., Burke, S., Parsons, M., Franz-Odendaal, T. and Fisher, S. (2012). Skeletogenic Fate of Zebrafish Cranial and Trunk Neural Crest. PLoS ONE 7, e47394.

Kapoor, A. (1970). Development of dermal bones related to sensory canals of the head in the fishes Ophicephalus punctatus Bloch (Ophicephalidae) and Wallago attu Bl. & Schn.Zool. J. Linn. Soc., 49, 69-97.

Kimmel, C. B., DeLaurier, A., Ullmann, B., Dowd, J. and McFadden, M. (2010). Modes of Developmental Outgrowth and Shaping of a Craniofacial Bone in Zebrafish. PLoS ONE 5, e9475.

Kozlowski, D. J., Whitfield, T. T., Hukriede, N. A., Lam, W. K. and Weinberg, E. S. (2005). The zebrafish dog-eared mutation disrupts *eya1*, a gene required for cell survival and differentiation in the inner ear and lateral line. Dev Biol 277, 27–41.

Lekander, B. (1949). The sensory line system and the canal bones in the head of some Ostariophysi. Acta Zoologica.

Lieschke, G. J. and Currie, P. D. (2007). Animal models of human disease: zebrafish swim into view. Nat Rev Genet 8, 353–367.

Lopez-Schier H, Hudspeth AJ. 2005. Supernumerary neuro- masts in the posterior lateral line of zebrafish lacking peripheral glia. Proc Natl Acad Sci USA 102:1496–1501

Metcalfe WK, Kimmel CB, Schabtach E. 1985. Anatomy of the posterior lateral line system in young larvae of the zebrafish. J Comp Neurol 233:377–389

Meyer, A., Biermann, C. H. and Ortí, G. (1993). The phylogenetic position of the zebrafish (Danio rerio), a model system in developmental biology: an invitation to the comparative method. Proc. Biol. Sci. 252, 231–236.

Moodie, R. L. (1922). The influence of the lateral line system on the peripheral osseous elements of fishes. and amphibia. J. Comp. Neurol. 34, 319–335.

Namdaran, P., Reinhart, K. E., Owens, K. N., Raible, D. W. and Rubel, E. W. (2012). Identification of Modulators of Hair Cell Regeneration in the Zebrafish Lateral Line. J.Neurosci. 32, 3516–3528.

Nelson, G. (1969). Infraorbital bones and their bearing on the phylogeny and geography of osteoglossomorph fishes. American Museum Novitates 2394, 1–37.

Nelson, J. S. (1976). Fishes of the world. New York: Wiley.

Nusslein-Volhard, C. and Dahm, R. (2002). Zebrafish: a practical approach. New York: Oxford University Press.

Ostrander, G. K. (2000). *The laboratory fish*. San Diego: Academic Press.Quarto N,

Longaker MT (2005) The zebrafish (Danio rerio): a model system for cranial suture patterning. Cells Tissues Organs 181: 109–118.

Parichy, D. M., Elizondo, M. R., Mills, M. G., Gordon, T. N. and Engeszer, R. E. (2009). Normal table of postembryonic zebrafish development: Staging by externally visible anatomy of the living fish. Dev. Dyn. 238, 2975–3015.

Raible, D. and Kruse, G. (2000). Organization of the lateral line system in embryonic zebrafish. J. Comp. Neurol. 189–198.

Rath, B., Nam, J., Knobloch, T. J., Lannutti, J. J. and Agarwal, S. (2008). Compressive forces induce osteogenic gene expression in calvarial osteoblasts. J. Biomech. 41, 1095–1103.

Sapède, D., Gompel, N., Dambly-Chaudière, C. and Ghysen, A. (2002). Cell migration in the postembryonic development of the fish lateral line. Development 129, 605–615.

Schilling, T. F. and Webb, J. (2007). Considering the zebrafish in a comparative context. J. Exp. Zool. 308B, 515–522.

Schoch, R. R. (2006). Skull ontogeny: developmental patterns of fishes conserved across major tetrapod clades. Evol. Dev. 8, 524–536.

Stone, L.S., 1922. Experiments on the development of the lateral line sense organs in *Amblystomea punctatum*. J. Exp. Zool 35, 421-496

Takahashi, Y., Bontoux, M. and Le Douarin, N. M. (1991). Epithelio--mesenchymal interactions are critical for Quox 7 expression and membrane bone differentiation in the neural crest derived mandibular mesenchyme. EMBO J. 10, 2387–2393.

Tyler, M. S. and McCobb, D. P. (1980). The genesis of membrane bone in the embryonic chick maxilla: epithelial-mesenchymal tissue recombination studies. J Embryol Exp Morphol 56, 269–281.

Webb, J. and Noden, D. (1993). Ectodermal Placodes Contributions to the Development of the Vertebrate Head. American zoologist.434-447.

Webb, J. F. and Shirey, J. E. (2003). Postembryonic development of the cranial lateral line canals and neuromasts in zebrafish. Dev. Dyn. 228, 370–385.

Westoll, T. S. (1937). On the cheek bones in teleostome fishes. J. of Anat. 71, 362–382.

Whitfield, T. T., Granato, M., van Eeden, F. J., Schach, U., Brand, M., Furutani-Seiki, M., Haffter, P., Hammerschmidt, M., Heisenberg, C. P., Jiang, Y. J., et al. (1996). Mutations affecting development of the zebrafish inner ear and lateral line. Development 123, 241–254.

Willems, B., Büttner, A., Huysseune, A., Renn, J., Witten, P. E. and Winkler, C. (2012). Conditional ablation of osteoblasts in medaka. Dev. Biol. 364, 128–137.

Williams, J. A. and Holder, N. (2000). Cell turnover in neuromasts of zebrafish larvae. Hearing Research 143, 171–181.

Witten, P. E. (1997). Enzyme histochemical characteristics of osteoblasts and mononucleated osteoclasts in a teleost fish with acellular bone (*Oreochromis niloticus*, Cichlidae). Cell and tissue research 287, 591–599.

Wu, P. (2004). Molecular Shaping of the Beak. Science 305, 1465–1466.

Yamamoto, Y., Espinasa, L., Stock, D. W. and Jeffery, W. R. (2003). Development and evolution of craniofacial patterning is mediated by eye-dependent and -independent processes in the cavefish *Astyanax*. Evol. Dev. 5, 435–446.

Young, B., Lowe, J.S., Stevens, A., Heath, J.V. 2006.Wheater's functional histology: a text and colour atlas. 5th Ed. London: Churchill Livingston. 186-206.

Appendix 1

Table 1. Summary of zebrafish specimens fixed for bone stain growth series.

Developmental Time-Point	Specimen Number	Clutch ID	DOB	DOD
8.0 mm SL	1	IOGSE 1	18/04/12	31/05/12
	2	IOGSE 1	18/04/12	31/05/12
	3	IOGSE 1	18/04/12	31/05/12
8.5 mm SL	1	IOGSE 1	18/04/12	29/05/12
	2	IOGSE 1	18/04/12	29/05/12
9.0 mm SL	1	CCTRANS 7	18/01/12	01/05/12
	2	IOGSE 1	18/04/12	29/05/12
	3	IOGSE 7	01/06/12	11/07/12
9.5 mm SL	1	CCAB 11	30/03/12	29/05/12
	2	CCTRANS1	08/09/11	13/10/11
	3	CCTRANS1	08/09/11	13/10/11
10.0 mm SL	1	IOGSE 1	18/04/12	31/05/12
	2	IOGSE 1	18/04/12	31/05/12
	3	IOGSE 1	18/04/12	29/05/12
	4	IOGSE 1	18/04/12	31/05/12
	5	CCTRANS1	08/09/11	12/10/11
10.5 mm SL	1	IOGSE 1	18/04/12	11/06/12
	2	IOGSE 1	18/04/12	31/05/12
	3	CCTRANS 7	18/01/12	01/05/12
	4	IOGSE 1	18/04/12	31/05/12
11.0 mm SL	1	IOGSE 5	02/05/12	11/06/12
	2	IOGSE 1	18/04/12	31/05/12
	3	CCTRANS 10	18/01/12	29/05/12
	4	CCTRANS 7	18/01/12	01/05/12
	5	CCTRANS 1	08/09/11	13/11/12
11.5 mm SL	1	IOGSE 1	18/04/12	11/06/12
	2	IOGSE 1	18/04/12	11/06/12
	3	IOGSE 1	18/04/12	11/06/12
	4	CCTRANS 7	18/01/12	01/05/12
	5	CCTRANS 7	18/01/12	01/05/12
	6	IOGSE 8	01/06/12	11/07/12
12.0 mm SL	1	CCTRANS 8	26/01/12	01/05/12
	2	CCTRANS 7	18/01/12	01/05/12
	3	CCTRANS 7	18/01/12	01/05/12
	4	IOGSE 1	18/04/12	31/05/12
	5	IOGSE 8	01/06/12	11/07/12
12.5 mm SL	1	IOGSE 1	18/04/12	11/06/12
	2	IOGSE 1	18/04/12	11/06/12
	3	IOGSE 1	18/04/12	11/06/12
	4	CCTRANS 1	08/09/11	12/11/11
	5	IOGSE 5	02/05/12	19/06/12

13.0 mm SL	1	CCTRANS 1	08/09/11	15/11/11
	2	CCTRANS 7	18/01/12	01/05/12
	3	IOGSE 4	02/05/12	19/06/12
	4	IOGSE 4	02/05/12	19/06/12
13.5 mm SL	1	CCTRANS 7	18/01/12	01/05/12
	2	CCTRANS	18/01/12	01/05/12
	3	CCAB 11	30/03/12	25/06/12
	4	IOGSE 4	02/05/12	25/06/12
14.0 mm SL	1	CCTRANS 7	18/01/12	01/05/12
	2	CCAB 11	30/03/12	29/05/12
	3	CCAB 11	30/03/12	29/05/12
	4	CCAB 11	30/03/12	29/05/12
	5	CCTRANS 8	18/01/12	01/05/12
14.5 mm SL	1	CCTRANS 7	18/01/12	01/05/12
	2	IOGSE 5	02/05/12	19/06/12
	3	IOGSE 5	02/05/12	25/06/12
	4	IOGSE 5	02/05/12	25/06/12
	5	IOGSE 8	01/06/12	11/07/12
	6	IOGSE 8	01/06/12	11/07/12
15.0 mm SL	1	CCTRANS 6	19/10/11	01/05/12
	2	CCTRANS 8	26/01/12	01/05/12
	3	CCTRANS 1	08/09/11	15/11/12
15.5 mm SL	1	CCTRANS 10	16/03/12	29/05/12
	2	IOGSE 5	02/05/12	19/06/12
16.0 mm SL	1	CCTRANS 8	19/10/11	01/05/12
	2	CCTRANS 7	18/01/12	01/05/12
16.5 mm SL	1	CCTRANS 10	16/03/12	29/05/12
	2	CCTRANS 1	08/09/11	04/01/12
17.0 mm SL	1	CCTRANS 1	08/09/11	04/01/12
	2	CCAB1	08/09/11	09/11/12
	3	CCTRANS 8	26/01/12	01/05/12
	4	CCAB 8	13/01/12	29/05/12
	5	CCAB 8	13/01/12	29/05/12
18.0 mm SL	1	CCAB1	08/09/11	09/11/12
	2	CCTRANS 1	08/09/11	10/02/12
	3	CCTRANS 6	19/10/11	01/05/12
	4	CCTRANS 6	19/10/11	01/05/12
	5	CCAB 8	13/01/12	29/05/12
20.0 mm SL	1	CCTRANS 6	19/10/11	01/05/12
22.0 mm SL	1	CCTRANS 6	19/10/11	01/05/12
25.0 mm SL	1	CCAB3	09/11/11	29/03/12
	2	CCAB3	09/11/11	29/03/12
	3	CCAB3	09/11/11	29/03/12

Table 2. Specimens fixed for Alkaline Phosphatase (AP) Stained Growth Series

Developmental Time-Point	Specimen Number	Clutch ID	DOB	DOD
6.0 mm SL	1	IOGSE 7	01/06/12	26/06/12
	2	IOGSE 7	01/06/12	26/06/12
	3	IOGSE 7	01/06/12	26/06/12
	4	IOGSE 7	01/06/12	26/06/12
	5	IOGSE 7	01/06/12	26/06/12
7.0 mm SL	1	IOGSE 7	01/06/12	26/06/12
	2	IOGSE 7	01/06/12	26/06/12
	3	IOGSE 7	01/06/12	26/06/12
	4	IOGSE 7	01/06/12	26/06/12
	5	IOGSE 6	25/05/12	26/06/12
	6	IOGSE 6	25/05/12	26/06/12
	7	IOGSE 6	25/05/12	26/06/12
8.0 mm SL	1	IOGSE 6	25/05/12	26/06/12
	2	IOGSE 6	25/05/12	26/06/12
	3	IOGSE 6	25/05/12	26/06/12
	4	IOGSE 4	02/05/12	26/06/12
	5	IOGSE 4	02/05/12	26/06/12
	6	IOGSE 4	02/05/12	26/06/12
9.0 mm SL	1	IOGSE 6	25/05/12	26/06/12
	2	IOGSE 6	25/05/12	26/06/12
	3	IOGSE 6	25/05/12	26/06/12
	4	IOGSE 4	02/05/12	26/06/12
	5	IOGSE 4	02/05/12	26/06/12
	6	IOGSE 4	02/05/12	26/06/12
	7	IOGSE 4	02/05/12	26/06/12
10.0 mm SL	1	IOGSE 4	02/05/12	26/06/12
	2	IOGSE 4	02/05/12	26/06/12
	3	IOGSE 4	02/05/12	26/06/12
	4	IOGSE 4	02/05/12	26/06/12
	5	IOGSE 4	02/05/12	26/06/12
	6	IOGSE 4	02/05/12	26/06/12
11.0 mm SL	1	IOGSE 4	02/05/12	26/06/12
	2	IOGSE 4	02/05/12	26/06/12
	3	IOGSE 4	02/05/12	26/06/12
	4	IOGSE 4	02/05/12	26/06/12
	5	IOGSE 4	02/05/12	26/06/12
	6	IOGSE 4	02/05/12	26/06/12
	7	IOGSE 4	02/05/12	26/06/12

12.0 mm SL	1	IOGSE 4	02/05/12	26/06/12
	2	IOGSE 4	02/05/12	26/06/12
	3	IOGSE 4	02/05/12	26/06/12
	4	IOGSE 4	02/05/12	26/06/12
	5	IOGSE 4	02/05/12	26/06/12
13.0 mm SL	1	IOGSE 4	02/05/12	26/06/12
	2	IOGSE 4	02/05/12	26/06/12
	3	IOGSE 8	01/06/12	11/07/12
	4	IOGSE 8	01/06/12	11/07/12
	5	IOGSE 8	01/06/12	11/07/12
14.0 mm SL	1	IOGSE 8	01/06/12	11/07/12
	2	IOGSE 8	01/06/12	11/07/12
	3	IOGSE 4	02/05/12	31/07/12
	4	IOGSE 4	02/05/12	31/7/12
15.0 mm SL	1	IOGSE 8	01/06/12	11/07/12
	2	IOGSE 8	01/06/12	11/07/12
	3	IOGSE 4	02/05/12	31/07/12
	4	IOGSE 4	02/05/12	31/07/12
	5	IOGSE 4	02/05/12	31/07/12
16.0 mm SL	1	IOGSE 8	01/06/12	11/07/12
	2	IOGSE 8	01/06/12	11/07/12
	3	IOGSE 4	02/05/12	31/07/12
	4	IOGSE 4	02/05/12	31/07/12
	5	IOGSE 4	02/05/12	31/07/12
17.0 mm SL	1	IOGSE 4	02/05/12	31/07/12
	2	IOGSE 4	02/05/12	31/07/12
	3	IOGSE 4	02/05/12	31/07/12
	4	IOGSE 4	02/05/12	31/07/12
	5	IOGSE 4	02/05/12	31/07/12
18.0 mm SL	1	IOGSE 4	02/05/12	31/07/12
	2	IOGSE 4	02/05/12	31/07/12
	3	IOGSE 4	02/05/12	31/07/12
	4	IOGSE 4	02/05/12	31/07/12
	5	IOGSE 4	02/05/12	31/07/12
19.0 mm SL	1	IOGSE 4	02/05/12	31/07/12
	2	IOGSE 4	02/05/12	31/07/12
	3	IOGSE 4	02/05/12	31/07/12
	4	IOGSE 4	02/05/12	31/07/12
	5	IOGSE 4	02/05/12	31/07/12
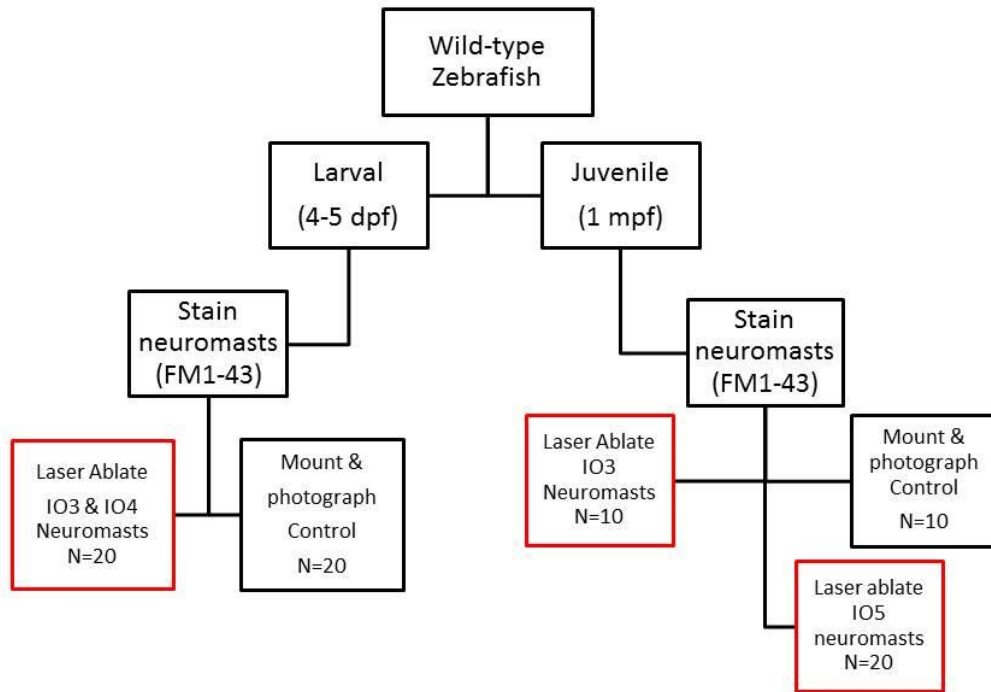
Figure 1. Flow-chart describing neuromast ablation experimental design for both larval and juvenile neuromast ablation. Laser ablation specimens are indicated by red boxes.

Table 3. Sizes of adult neuromast ablation specimens measured prior to fixation.

	Experiment Ablation Group			
	Controls	Larval	IO3 Juvenile	IO5 Juvenile
Size (cm SL)	2.50	2.40	2.10	2.20
	2.60	2.40	2.20	2.20
	2.50	2.20	2.00	2.30
	2.40	2.20	2.40	2.30
	2.20	2.00	2.20	2.20
	2.50	2.50	2.20	2.50
	2.20	2.20	2.20	2.20
	2.10	2.20	2.30	2.20
	2.00	2.00	2.40	2.10
	2.00	2.50	2.50	2.20
	2.00	2.50		2.30
	2.10	2.20		2.20
	2.10	2.20		2.10
	2.40	2.10		2.20
				2.50
				2.40
				2.30
				2.20
Mean Size	2.26	2.26	2.25	2.26

Table 4. Canal wall measurement ratios for adult neuromast ablation specimens. Ratio was calculated by comparing the length of raised canal wall to the total length of the presumptive canal.

	Control			Larval			Juvenile IO3	Juvenile IO5
	IO3	IO4	IO5	IO3	IO4	IO5		
Ratio of length of raised canal wall vs. total presumptive canal length	1.95	1.19	1.76	1.80	1.37	1.49	1.46	1.44
	2.00	1.47	1.57	1.48	1.27	1.33	1.65	1.31
	1.98	1.10	1.72	1.38	0.88	0.89	1.63	1.52
	1.94	1.94	1.71	1.27	1.20	0.77	1.66	1.55
	1.71	2.00	1.13	1.40	0.97	0.96	1.64	1.63
	1.77	1.70	1.85	1.25	1.15	1.09	1.28	1.59
	1.76	2.00	1.72	1.14	1.45	1.20	1.68	1.70
	1.91	2.00	1.67	1.82	1.20	1.16	1.69	1.63
	1.96	1.75	1.78	1.41	1.34	1.28	1.55	1.61
	1.50	1.74	1.54	1.22	1.21	1.36	1.49	1.51
				1.33	1.44	1.31		1.56
				1.60	1.73	1.29		1.64
				1.64	1.73	1.59		1.29
				1.36	1.68			1.45
				1.63				1.67
								1.63
								1.72
								1.62
								1.52
								1.36
Mean	1.85	1.69	1.64	1.45	1.33	1.21	1.57	1.55
SD	0.15	0.32	0.19	0.20	0.25	0.22	0.12	0.12
SE	0.05	0.11	0.06	0.05	0.07	0.06	0.04	0.03

Appendix 2
0.1M PBS Stock Solution Recipe

- 80g NaCl (Sigma SX0420-3)
- 2g KCl (Sigma P217-10)
- 11.2g Na2HPO4 (Sigma SX0720-1)
- 2g KH2PO4 (Sigma P5655)
- in 1000mL
- pH to 7.4

Aptes Coated Slides

- dip slides in 100% EtOH two times
- dip slides in tap H2O
- dry in incubator at 38°C
- allow slides to cool
- dip slides in 2% Aminopropyl triethoxy-silane (APTES) (Sigma A3648) in acetone (Fisher A18-4)
- dip in 100% acetone (Fisher Scientific A18-4) twice
- dry in incubator at 38°C overnight
- store at room temperature

Haupt's Coated Slides

- dip slides in 100% ethanol twice
- dry slides overnight at 38°C
- using a KimWipe coat slides with Haupt's Gelatin Solution (all solutions used were pre-made, see recipe below)
- allow slides to dry overnight at 38°C
- store at room temperature
    Haupt's Gelatin Solution
    - Warm distilled water to 30°C
    - Dissolve 2g of phenol crystals into warmed water
    - Add 1g of powdered gelatin and 15mL of glycerine
    - Stir well and filter when cool
    - Solution can be diluted if needed

Acid-Free Double Stain for Bone and Cartilage (for Adult specimens)
(Modified from Edsall and Franz-Odendaal, 2010)

1) Remove the specimen from the fixative and insert to a 50% ethanol solution for 10 minutes with agitation
2) Descale and degut the specimen and replace ethanol with Alcian blue staining solution. Allow for staining to occur over night with agitation
3) Remove the Alcian blue stain from the test tube and briefly rinse the specimen with distilled water. Invert test tube twice maximum
4) Remove the water from the test tube and replace with the bleaching solution. Allow to for bleaching to occur overnight
5) Remove the bleaching solution from the test tube and briefly rinse the specimen with distilled water. Invert test tube twice maximum
6) Remove the water from the test tube and replace with saturated borax. Specimen can sit in saturated borax for the duration of the day or overnight
7) Remove the saturated borax from the test tube and add alizarin red staining solution. Allow for staining over night with agitation
8) Remove the staining solution form the test tube and rinse the specimen in 1% KOH.
9) Remove the 1% KOH from the test tube and replace with Trypsin-Borax tissue digestion solution. Allow for digestion to occur overnight
10) Remove digestion solution and initiate glycerol solution series to 100% glycerol (made in 1% KOH). Store

Alcian Blue Staining Solution:
For 100mL of solution:
- 5mL 0.4% Alcian blue (Sigma, A3157) in 70% ethanol
- 70mL of 95% ethanol
- 25mL 20mM $MgCl_2$ (Fisher, 930963)
- Final concentrations: 0.02% Alcian blue, 20mM MgCl2 and 70% ethanol

Alizarin Red Staining Solution:
- 0.001g/mL of alizarin red (Sigma-Aldrich A5533) of 1%KOH

Bleaching Solution:
- 5 ml of 3% hydrogen peroxide (Compliments brand) and 100 ml of 1% potassium hydroxide (Sigma, 221473)

Trypsin-Borax Digestion Solution:
- 1% Trypsin (Fisher, T360-500) and 2% sodium tetraborate decahydrate (Sigma, B9876) in distilled water

**Appendix 3**

Morphometric analyses were conducted by applying 20 landmarks on the lateral

views of right side of the skull. Procrustes superimposition was used to align

corresponding landmarks in order to analyze these changes in shape. Goodall's F-tests

indicate that the ablation of neuromasts at larval and juvenile (both IO3 and IO5

ablations) is significantly different from the control (p<0.01, n=13, n=10, n=20

respectively). These results agree with the findings from the resampling test F test,

Procrustes (p<0.05, F-score: 1.67, p<0.05, F-score: 2.37, p<0.05, F-score: 2.93, and

p<0.05).
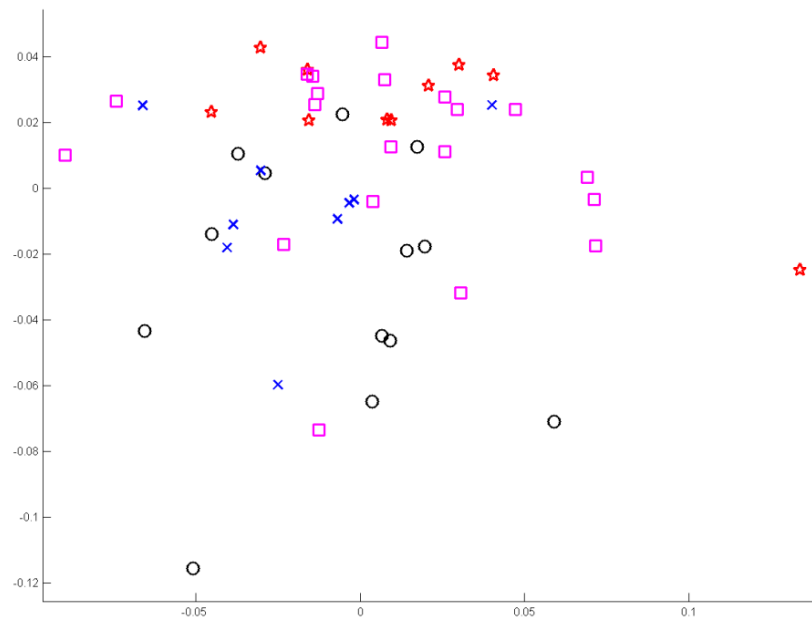
Figure 2. Principal component analysis of adult neuromast ablation specimens based on landmark morphometrics. (cross)Control, (circle) larval ablation, (star) IO3 juvenile and (square) IO5 juvenile ablation specimens.
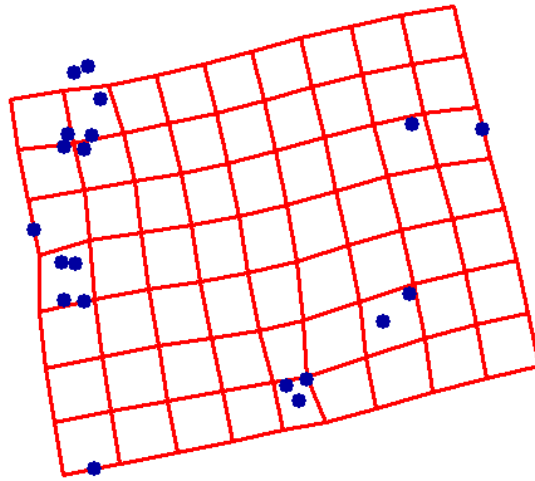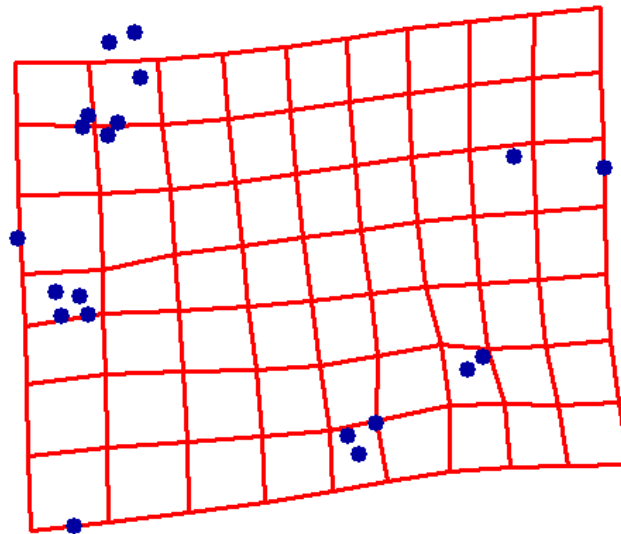
Figure 3. Thin plates spline morphometrics of lateral view of adult, larval neuromast ablation specimens compared to controls.
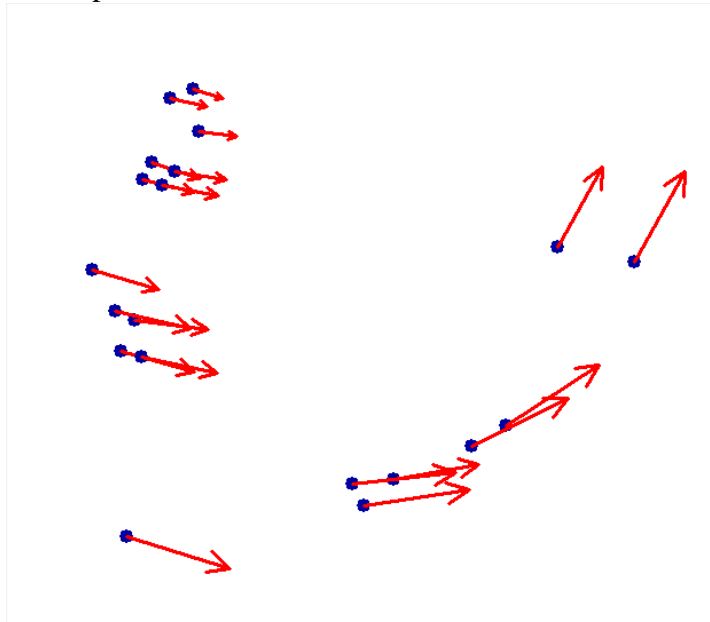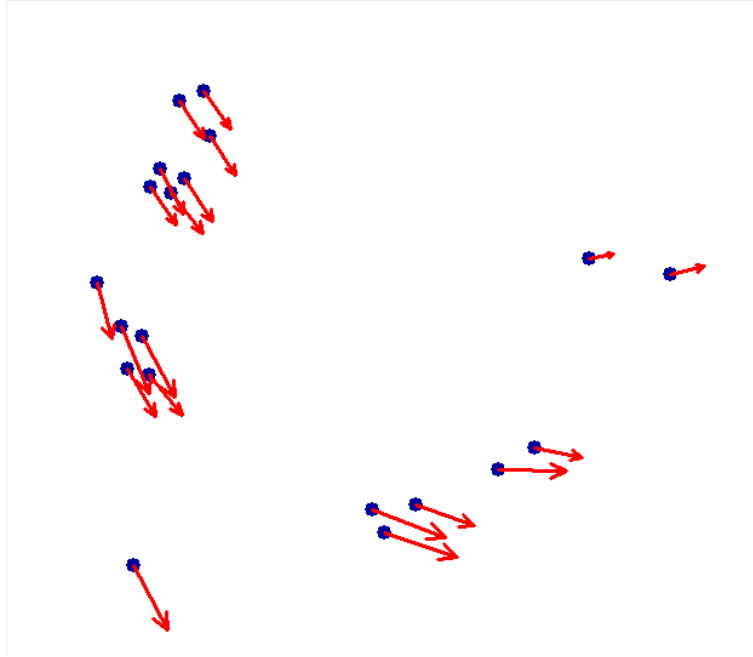

Figure 4. Vector morphometrics of lateral view of (red arrow) adult, larval neuromast ablation specimens compared to (blue dot) control specimens.
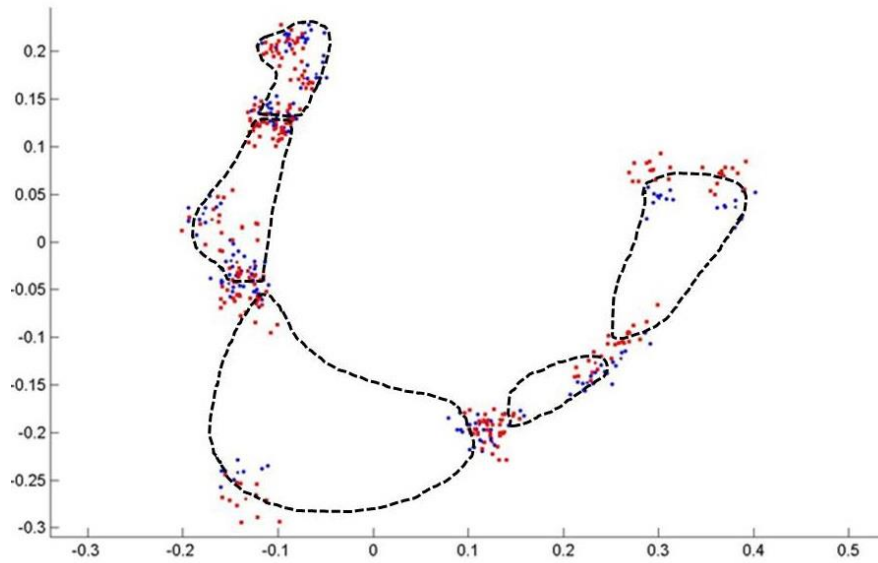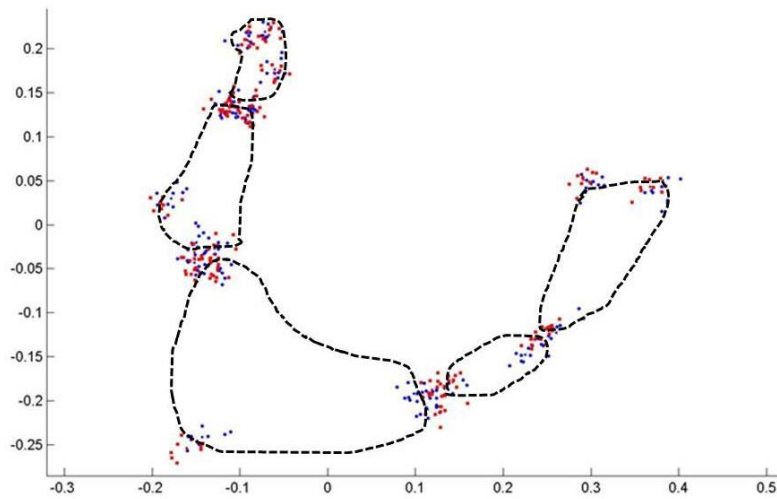
Figure 5. Procrustes superimposition morphometrics of lateral view of adult, (red) larval neuromast ablation specimens compared to control adult specimens (blue). Approximate location of IO bones are outlined with black dashed line.
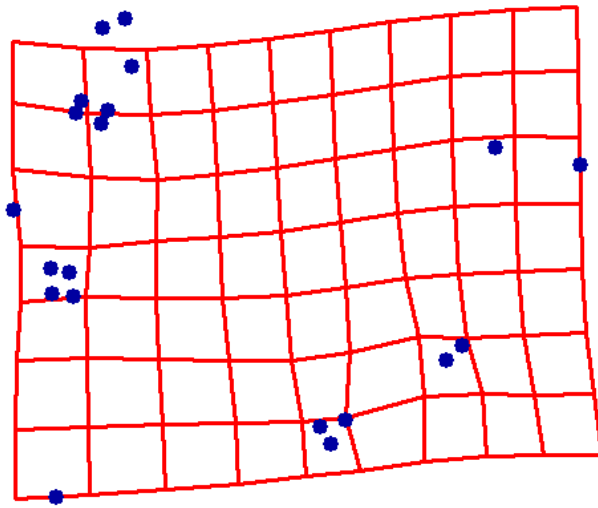

Figure 6. Thin plates spline morphometrics of lateral view of adult, juvenile IO3 neuromast ablation specimens compared to controls.
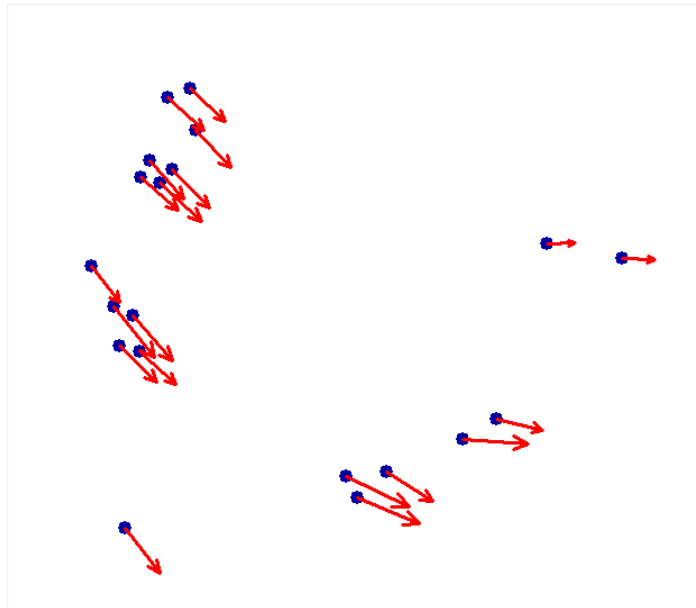
Figure 7. Vector morphometrics of lateral view of (red arrow) adult, juvenile IO3 neuromast ablation specimens compared to (blue dot) control specimens.
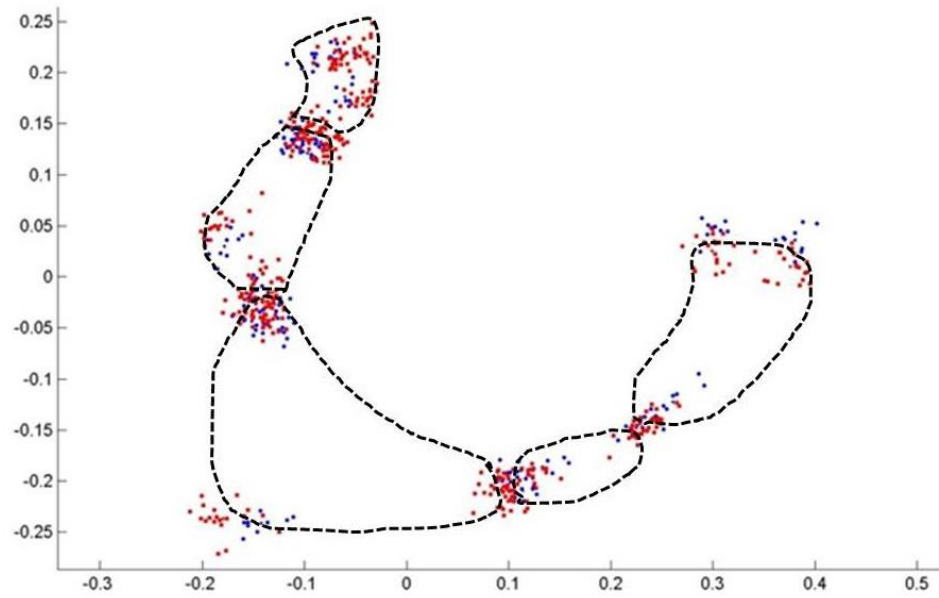

Figure 8. Procrustes superimposition morphometrics of lateral view of adult, (red) juvenile IO3 neuromast ablation specimens compared to control adult specimens (blue). Approximate location of IO bones are outlined with black dashed line.

134

Figure 9. Thin plates spline morphometrics of lateral view of adult, juvenile IO5 neuromast ablation specimens compared to control.

Figure 10. Vector morphometrics of lateral view of (red arrow) adult, juvenile IO5 neuromast ablation specimens compared to (blue dot) control specimens.

Figure 11. Procrustes superimposition morphometrics of lateral view of adult, (red) juvenile IO5 neuromast ablation specimens compared to control adult specimens (blue). Approximate location of IO bones are outlined with black dashed line.